A novel high-z submm galaxy efficient line survey in ALMA Bands 3 through 8-an ANGELS pilot

Citation for the original published paper (version of record):
Bakx, T., Amvrosiadis, A., Bendo, G. et al (2024). A novel high-z submm galaxy efficient line survey in ALMA Bands 3 through 8-an ANGELS pilot. Monthly Notices of the Royal Astronomical Society, 535(2): 1533-1574. http://dx.doi.org/10.1093/mnras/stae2409

(article starts on next page)

Monthly Notices of the ROYAL ASTRONOMICAL SOCIETY

MNRAS **535,** 1533–1574 (2024)
Advance Access publication 2024 October 23

https://doi.org/10.1093/mnras/stae2409

A novel high-z submm galaxy efficient line survey in ALMA Bands 3 through 8 – an ANGELS pilot

T. J. L. C. Bakx,[1,2,3]★ A. Amvrosiadis,[4] G. J. Bendo,[5] H. S. B. Algera,[3,6] S. Serjeant,[7] L. Bonavera,[8,9] E. Borsato,[10] X. Chen,[3] P. Cox,[11] J. González-Nuevo,[8,9] M. Hagimoto,[3] K. C. Harrington,[12] R. J. Ivison,[13,14,15,16] P. Kamieneski,[17] L. Marchetti,[18,19] D. A. Riechers,[20] T. Tsukui,[16,21] P. P. van der Werf,[22] C. Yang,[1] J. A. Zavala,[3] P. Andreani,[23] S. Berta,[24] A. R. Cooray,[25] G. De Zotti,[10] S. Eales,[26] R. Ikeda,[27,28] K. K. Knudsen,[1] I. Mitsuhashi,[3] M. Negrello,[26] R. Neri,[24] A. Omont,[11] D. Scott,[29] Y. Tamura,[3] P. Temi[30] and S. A. Urquhart[7]

Affiliations are listed at the end of the paper

Accepted 2024 October 21. Received 2024 October 21; in original form 2024 June 28

ABSTRACT

We use the Atacama Large sub/Millimetre Array (ALMA) to efficiently observe spectral lines across Bands 3, 4, 5, 6, 7, and 8 at high-resolution (0.5–0.1 arcsec) for 16 bright southern *Herschel* sources at $1.5 < z < 4.2$. With only six and a half hours of observations, we reveal 66 spectral lines in 17 galaxies. These observations detect emission from CO (3−2) to CO(18−17), as well as atomic ([C I](1−0), (2−1), [O I] 145 μm and [N II] 205 μm) lines. Additional molecular lines are seen in emission (H_2O and H_2O^+) and absorption (OH^+ and CH^+). The morphologies based on dust continuum ranges from extended sources to strong lensed galaxies with magnifications between 2 and 30. CO line transitions indicate a diverse set of excitation conditions with a fraction of the sources (∼ 35 per cent) showcasing dense, warm gas. The resolved gas to star formation surface densities vary strongly per source, and suggest that the observed diversity of dusty star-forming galaxies could be a combination of lensed, compact dusty starbursts and extended, potentially merging galaxies. The predicted gas depletion time-scales are consistent with 100 Myr to 1 Gyr, but require efficient fuelling from the extended gas reservoirs onto the more central starbursts, in line with the Doppler-shifted absorption lines that indicate inflowing gas for two out of six sources. This pilot paper explores a successful new method of observing spectral lines in large samples of galaxies, supports future studies of larger samples, and finds that the efficiency of this new observational method will be further improved with the planned ALMA Wideband Sensitivity Upgrade.

Key words: galaxies: evolution – galaxies: high-redshift – submillimetre: galaxies.

1 INTRODUCTION

The discovery of a population of dusty galaxies – called either submm galaxies (SMGs; Smail, Ivison & Blain 1997; Hughes et al. 1998; Blain et al. 2002) or dusty star-forming galaxies (DSFGs; Casey, Narayanan & Cooray 2014) – showed that more than half of the star formation in the early Universe was shrouded in dust. With total infrared luminosities exceeding several times $10^{12}\,L_\odot$, the star formation rates (SFRs) in these SMGs and DSFGs (hereafter, we use DSFGs for simplicity) approach the stability limit of $1000\,M_\odot\,yr^{-1}$ and may even exceed this limit (Andrews & Thompson 2011; Fudamoto et al. 2017; Rowan-Robinson et al. 2018). These intense SFRs – enough to build a large galaxy in only 0.1 Gyr – suggest that these may be the ancestors of present-day early-type galaxies (Eales et al. 1999; Lilly et al. 1999). Evidence of this evolutionary pathway of DSFGs to quenched elliptical galaxies is mounting, given their high stellar masses (Hainline et al. 2011; Aravena et al. 2016; Long et al. 2023; Smail et al. 2023), high specific SFRs (Straatman et al. 2014; Spilker et al. 2016; Glazebrook et al. 2017; Schreiber et al. 2018; Merlin et al. 2019) and location in overdense regions (Blain et al. 2004; Weiß et al. 2009; Hickox et al. 2012). However, the DSFG population appears diverse (e.g. Hagimoto et al. 2023), and because the types of galaxies studied in this paper are very rare (a few/deg^2 for $> 10^{12.5}\,L_\odot$), hydrodynamical models struggle to include a large enough volume to simulate these galaxies accurately to test the evolutionary pathways of these DSFGs (e.g. Narayanan et al. 2015). Observations of large numbers of DSFGs are thus the only direct way of understanding this population.

The *Herschel Space Observatory* increased the number of known DSFGs from hundreds to over half a million sources through several large-area surveys. In these surveys, the SPIRE instrument (Spectral and Photometric Imaging Receiver; Griffin et al. 2010) observed these large areas at the peak of the redshifted DSFG dust spectra without the hindering effects of the atmosphere. The total mapping area of *Herschel* surveys is over 1000 sq deg^2, with 660 deg^2 *Herschel* Astrophysical Terahertz Large Area Survey (H-ATLAS; Eales et al. 2010) and the 380 deg^2 *Herschel* Multi-tiered Extragalactic Survey

★ E-mail: tom.bakx@chalmers.se

(Oliver et al. 2012) and the *Herschel* Stripe 82 Survey (Viero et al. 2014) accounting for the bulk of the area increase (Shirley et al. 2021). The vast increase in survey area (at the time, ground-based surveys only covered ~1 deg^2 in total) also meant that *Herschel* discovered many more of the most extreme DSFGs. This has been complemented by observations in the mm regime, such as the South Pole Telescope survey, which revealed around a hundred sources that are also at high redshift from over 2500 deg^2 (Reuter et al. 2020).

To examine the nature of these extreme high-redshift sources, it is crucial to perform detailed studies characterizing the conditions of the interstellar medium (ISM) conditions seen through resolved spectral line observations (e.g. Hodge et al. 2019). Recent high-resolution follow-up studies of H-ATLAS sources, to use one survey as an example, have revealed 14 sources with $4 < z < 6.5$ with SFRs up to 8000 $\mathrm{M_\odot\,yr^{-1}}$, well over the maximal starburst limit (Fudamoto et al. 2017; Zavala et al. 2018; Montaña et al. 2021), and the discovery of a source at $z = 4.002$ which when followed up with Atacama Large sub/Millimetre Array (ALMA) turned out to be the core of a protocluster (Oteo et al. 2018), with its large scale environment forming stars at a rate of several tens of thousands of solar masses per year.

Given the large beam size of single-dish telescopes, high-redshift submm astronomy was often jokingly referred to as blobology prior to the advent of interferometer facilities such as ALMA, CARMA (Combined Array for Research in Millimeter-wave Astronomy), NOEMA (Northern Extended Millimeter Array; previously PdBI), and the SMA (Submillimeter Array). These interferometers were able to reveal large numbers of spectral lines of individual sources with NOEMA (e.g. Yang et al. 2023), as well as stunning lensing arcs and *Einstein* rings (e.g. Dye et al. 2015, 2018; Spilker et al. 2016), while targeting spectral lines at high resolution with ALMA (e.g. Rizzo et al. 2020). Particularly since the advent of large samples of DSFGs with robust redshifts (Reuter et al. 2020; Urquhart et al. 2022; Cox et al. 2023), spectroscopic follow-up studies are the key next step in a full characterization of this extreme population. Unfortunately, while interferometers are powerful instruments, the modest bandwidths currently available at ALMA mean that spectral line observations require dedicated tunings for every source, resulting in either runaway observation times or statistically insignificant samples. Consequently, a comprehensive high-resolution spectroscopic study of complete bright *Herschel* samples, or for that matter any survey from large-area mapping studies, is beyond the scope of current instrumentation. The Wideband Sensitivity Upgrade (WSU; Carpenter et al. 2023) will provide some relief, but as we will show, even its most optimistic goals can benefit from the methods detailed in this exploratory paper.

To break the current paradigm – i.e. long observations or small samples – this paper attempts short snapshot-style observations with ALMA (similar to Dye et al. 2018; Amvrosiadis et al. 2018) while targeting as many spectral lines as possible: A Novel high-z submm Galaxy Efficient Line Survey (ANGELS; Appendix Fig. F1). We describe this technique in Section 2, together with the definition of the sample of galaxies, and the ALMA data reduction steps. We describe the results of the observations, both for continuum and line measurements, in Section 3. We find lensing morphology for around half of the sample, and we report the lensing and ancillary data properties in Section 4. We place the line properties into context of the literature in Section 5. The resolved studies of ANGELS sources are discussed in Section 6. We collate an overview of the nature of the ANGELS sources, as became apparent by these observations, in Section 7. We evaluate this efficient line survey in Section 8, where we also detail the inevitable caveats and look into the future of surveys including the benefits of the WSU (Carpenter et al. 2023). Conclusions are summarized in Section 9. Throughout this paper, we assume a flat Lambda-cold dark matter cosmology with the best-fitting parameters derived from the *Planck* results (Planck Collaboration VI 2020), which are $\Omega_\mathrm{m} = 0.315$, $\Omega_\Lambda = 0.685$, and $h = 0.674$.

2 OBSERVATIONS

We target a group of sources within 10 deg on the sky using rapid two-minute snapshots across Bands 3–8 to test the viability of a rapid line survey with ALMA across the available bands with the best atmospheric transmission. Prior high-redshift observations with ALMA were limited to observations that have to retune the local oscillator and subsequently repeat the calibration observations. This approach results in large overheads ($\sim 20 - 30$ min per target) and requires a large program before 100 lines are reached. Our method instead asks: what specific tuning would allow us to target as many spectral lines as possible? The purpose of this paper is to test the usefulness of a snapshot-style line survey with bandwidths optimized to cover as many lines as possible. In Section 2.1, we describe the selected sources, and detail the ANGELS method in Section 2.2, before describing the data reduction steps in Section 2.3.

2.1 Target selection

The group of sources is selected from the 285 deg^2 South Galactic Pole (SGP) field from the H-ATLAS survey (Eales et al. 2010). The field is centred on RA, Dec. = 23:24:46, −33:00:00, and is shown in Fig. 1 (Valiante et al. 2016; Ward et al. 2022). In total, this field contains 88 bright high-redshift *Herschel* sources ($5 > z_\mathrm{phot} > 2$ and $350 > S_{500} > 80$ mJy; Bakx et al. 2018, 2020b), of which 65 sources have one or more ALMA-resolved sources with spectroscopic redshifts (which increased to 68 sources by including the spectroscopic redshifts identified by this program). These sources represent a larger sample of roughly the 300 brightest high-redshift objects (Nayyeri et al. 2016; Negrello et al. 2017; Bakx et al. 2018, 2020b) selected from a thousand square degrees of *Herschel* surveys, and typically have slightly lower observed luminosities than the majority-lensed South Pole Telescope- (SPT; $\overline{\mu L_\mathrm{IR}} = 4.4 \times 10^{13}\,\mathrm{L_\odot}$, Reuter et al. 2020) and *Planck*-selected galaxies ($\overline{\mu L_\mathrm{IR}} = 1.2 \times 10^{14}\,\mathrm{L_\odot}$, Berman et al. 2022) from ~ 2500 deg^2 and an all-sky survey, respectively. Meanwhile, these *Herschel* sources have higher apparent luminosities than the more abundant, typically unlensed SMGs from ground-based submm observations (e.g. Garratt et al. 2023), that are selected from surveys of up to ~ 10 deg^2. The Bright Extragalactic ALMA Redshift Survey (BEARS) provided the bulk of the spectroscopic redshifts across 62 *Herschel* sources (Urquhart et al. 2022), for a total of 71 ALMA-resolved galaxies with average lensed infrared luminosities of $\overline{\mu L_\mathrm{IR}} = 4.0 \times 10^{13}\,\mathrm{L_\odot}$. This survey efficiently used Bands 3 and 4 to derive robust spectroscopic redshifts using multiple carbon-monoxide (CO) and atomic carbon ([C I]) lines (Bakx & Dannerbauer 2022); and in addition, the data enabled subsequent marginally resolved studies of the dust continuum (Bendo et al. 2023) and molecular gas (Hagimoto et al. 2023).

The observations in this pilot program aimed to target a group of sources close on the sky (< 10 deg) with spectroscopic redshifts. We identified this group of sources using the ALMA Observing Tool, which split the 88 sources across six groups on the sky that can each be observed within a single calibration, i.e. all sources that are closer together than 10 deg on the sky. The group that was selected (RA, Dec. = 00:00:00, −33:29:00) contains most fields with spectroscopic redshifts; 13 out of 16 fields had at least one source

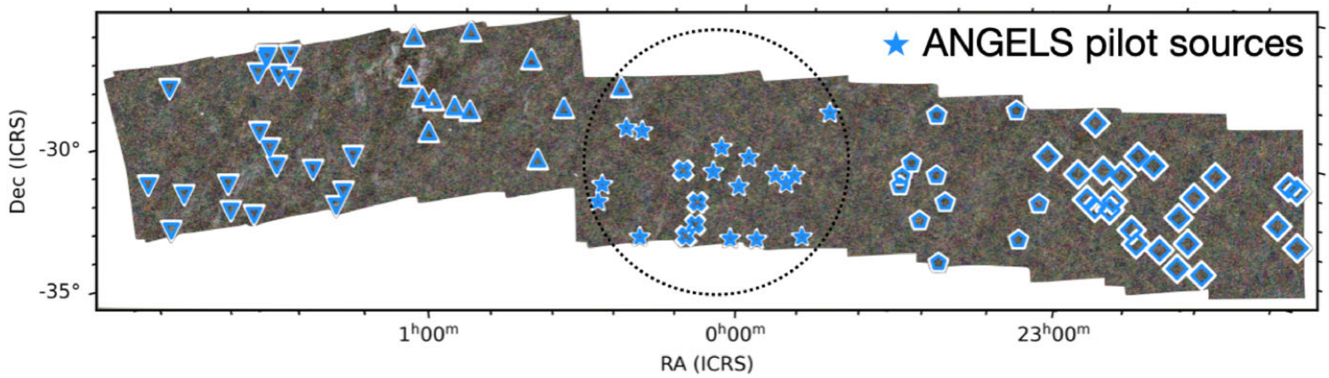

Figure 1. The 88 *Herschel* Bright Sources (Bakx et al. 2018, 2020b) in the 285 deg^2 SGP field (85 observed in the BEARS survey; Urquhart et al. 2022). Observations within 10 deg on the sky can be done in rapid succession, without the need for additional calibration. Here, we show the five different regions across the SGP field indicated with different symbols, with the central field used for Pilot observations (star symbols), while the four remaining fields (upward and downward triangles, hexagons, and diamonds) are left for subsequent follow-up. Note that four sources were excluded at the time of observation (crosses). The circle with a radius of ∼ 7 deg indicates the typical size for sources that the ALMA Observing Tool predicts can be observed with only a single calibration step for ALMA configuration schedules C43-6 and smaller.

Table 1. Sources targeted by ANGELS pilot.

Source	z	RA	Dec.	ΔV [km s^{-1}]
HerBS-21AB	3.323	23:44:18.112	−30:39:36.58	550 ± 110
HerBS-22A	3.050	00:26:25.000	−34:17:38.22	680 ± 150
HerBS-22B‡	–	00:26:25.560	−34:17:23.30	–
HerBS-25	2.912	23:58:27.505	−32:32:45.05	210 ± 40
HerBS-36	3.095	23:56:23.079	−35:41:19.64	550 ± 80
HerBS-41A	4.098	00:01:24.796	−35:42:11.15	680 ± 100
HerBS-41B‡	–	00:01:23.240	−35:42:10.80	–
HerBS-41C‡	–	00:01:25.820	−35:42:18.00	–
HerBS-42A	3.307	00:00:07.458	−33:41:03.07	640 ± 70
HerBS-42B	3.314	00:00:07.428	−33:40:55.82	490 ± 90
HerBS-42C‡	–	00:00:07.050	−33:41:03.40	–
HerBS-81A	3.160	00:20:54.739	−31:27:50.96	670 ± 200
HerBS-81B	2.588	00:20:54.201	−31:27:57.49	650 ± 190
HerBS-86	2.564	23:53:24.569	−33:11:11.93	460 ± 100
HerBS-87†	2.059	00:25:33.683	−33:38:26.21	370 ± 110
HerBS-93	2.402	23:47:50.443	−35:29:30.13	640 ± 160
HerBS-104A‡	–	00:18:39.470	−35:41:48.00	–
HerBS-104B†	1.536	00:18:38.851	−35:41:33.09	430 ± 130
HerBS-106A	2.369	00:18:02.467	−31:35:05.17	500 ± 170
HerBS-106B‡	–	00:18:01.104	−31:35:08.00	–
HerBS-155A	3.077	00:03:30.644	−32:11:35.00	500 ± 150
HerBS-155B‡	–	00:03:30.060	−32:11:39.30	–
HerBS-159A	2.236	23:51:21.750	−33:29:00.53	280 ± 80
HerBS-159B	2.236	23:51:22.363	−33:29:08.14	330 ± 90
HerBS-170†	4.182	00:04:55.445	−33:08:12.85	680 ± 180
HerBS-184	2.507	23:49:55.661	−33:08:34.48	320 ± 40

Notes. Column 1: source name. In the case of source multiplicity, we denote the brightest component with the letter A, and subsequent letters mark the source sensitivity. Column 2: spectroscopic redshift from submm observations. Column 3: right ascension in [hms] units. Column 4: declination in [dms] units. Column 5: Velocity–width in [km s^{-1}] units from unresolved ALMA observations (Urquhart et al. 2022). †The redshifts of these sources are confirmed using the ANGELS observations, and are based on the lines included in this paper, see Section 8.1. ‡ These sources do not have spectroscopic redshifts and are not completely covered by the primary beam across Bands 3–8. If the field only has one galaxy with a spectroscopic redshift, we drop the subindex (i.e. A, B etc.) throughout the paper for legibility reasons. These sources are shown in Appendix B.

with a spectroscopic redshift, ranging between $z = 1.536$ and 4.182 with a median value of $\bar{z} = 2.843$, see Table 1. The average infrared luminosities of these 16 fields are on average $\overline{\mu L_{\rm IR}} = 4.2 \times 10^{13}\,{\rm L_\odot}$ based on the luminosities documented in (Bakx et al. 2018, 2020b),[1] and thus these fields are representative of the larger BEARS and HerBS samples. In total, 26 resolved galaxies exist within these 16 fields. An additional four fields were not targeted in these initial ANGELS observations, although they were within the range of this field (shown as crosses in Fig. 1). Only one line was detected in the spectra of the three remaining sources (HerBS-87, HerBS-104, and HerBS-170), and it was not possible to determine robust redshifts for these targets. The additional observations from ANGELS allowed us to cut through this redshift degeneracy and measure redshifts for these three sources (see Section 8.1).

2.2 The ANGELS method

The number density of sources allowed the use of short snapshots (≈ 2 min) with only a single ∼ 20 − 30 min calibration step to reduce the overheads typically associated with line surveys (∼one calibration per targeted line). As a result, each observation required roughly one hour per band. This style of snapshot observation is not unique (e.g. Amvrosiadis et al. 2018 showed short snapshots can reveal the morphology of 15 lensed galaxies with only 2 min of on-source time), however this ANGELS pilot project explicitly focuses to include as many spectral lines as possible, while covering a much larger range of frequencies between Bands 3–8. Since we knew the redshifts of all of our targets (except for HerBS-87, -104, and -170, at the time of observing), we could use the cosmological frequency shift of the Universe as our spectrometer and evaluate the coverage of the spectral windows at the rest-frame frequencies of all of the *Herschel* galaxies (see Fig. 2). The sources are shown by their spectral windows shifted to their rest-frame frequency, and any lines within the spectral windows are marked as circles in the bottom panel. Typically, Bands 3 and 4 are able to target CO and [C I] (at 492.161 GHz) emission

[1]This value is slightly higher than the luminosities from a refit using the spectroscopic redshifts with the Eyelash template (e.g. Ivison et al. 2016) of $2.9 \times 10^{13}\,{\rm L_\odot}$, which still comparable to the average luminosity of the BEARS sample.

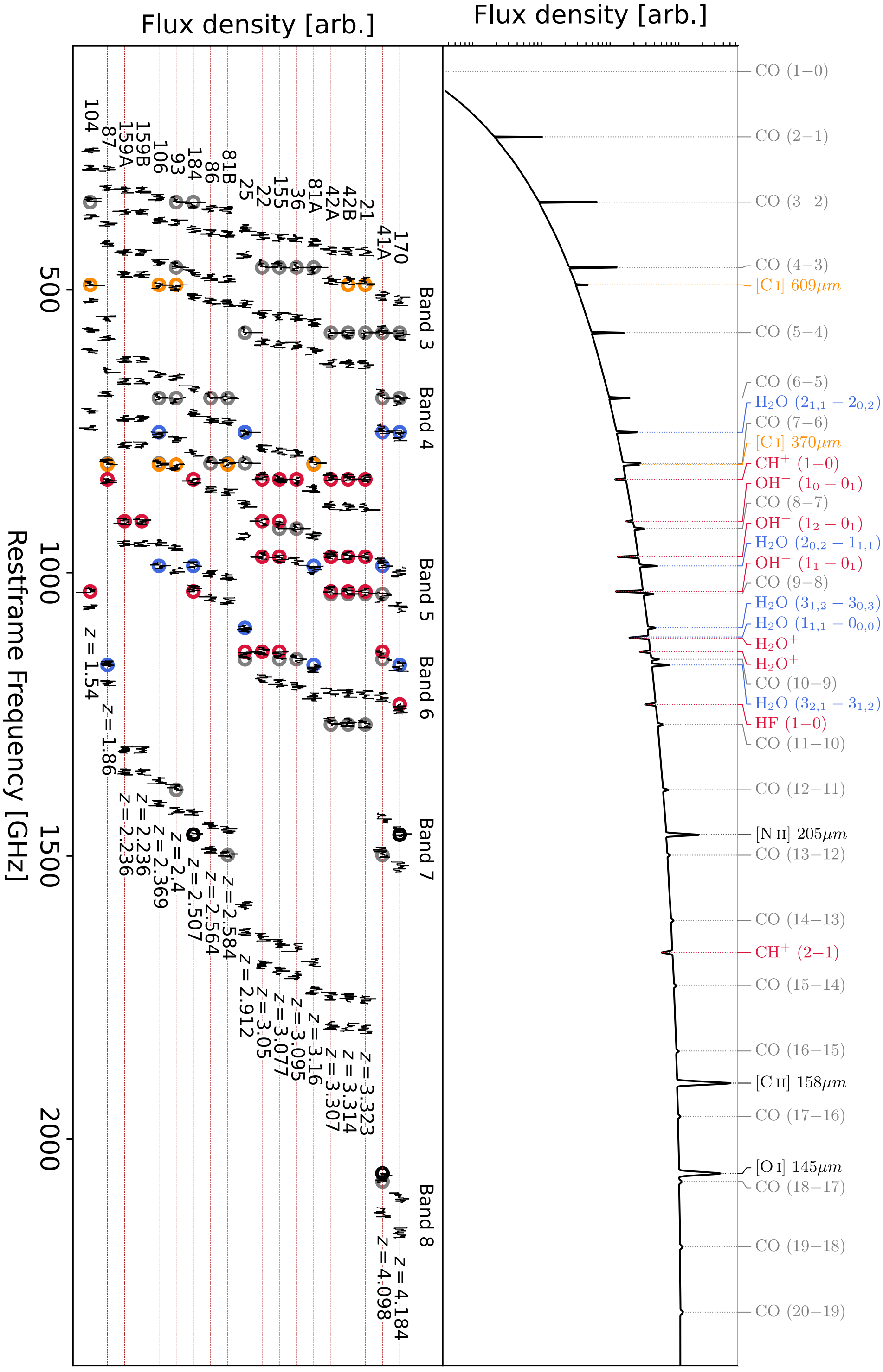

Figure 2. The top panel shows the rest-frame spectra of a typical dusty galaxy, assuming a two-body dust spectrum based on *Herschel* observations (Pearson et al. 2013) in conjunction with the spectral lines of a local Ultra-Luminous InfraRed Galaxy (ULIRG), in this case based on the line ratios of Arp220 by Rangwala et al. (2011). Most lines are seen in emission, with CO (grey), [C I] (orange), and water (blue, of course) lines at low frequencies, and atomic lines at high frequencies (shown in black). A forest of absorption lines is seen at the ∼ 1000 GHz frequency range, consisting of CH^+, OH^+, and (ionized) water lines, shown in red. The bottom panel shows the rest-frame frequencies of the optimized tunings in Bands 3, 4, 5, 6, 7, and 8 for each of the sources in ANGELS. The tunings (shown as the aperture-extracted spectra in black lines) were optimized to target as many lines as possible, and wherever they are expected to observe a line, we mark the frequency with a circle. The sources are sorted by redshift, with the lowest redshift source at the bottom, and the highest redshift source at the top.

Table 2. ANGELS optimized observation set-up.

Tuning	Bandwidth [GHz]	Observing depth Cont. [mJy beam^{-1}]	35 km s^{-1}	Resolution [arcmin × arcmin]	FoV (arcsec)	MRS (arcsec)	Pix. size (arcsec)	Cal. unc. (per cent)
Band 3[@]	98.3705... 102.0895 & 110.3705... 114.0895	0.051	1.25	0.51 × 0.30	82	4.2	0.05	5
Band 4[#]	132.4405... 136.1605 & 144.4405... 148.1605	0.049	1.04	0.38 × 0.34	62	4.1	0.05	5
Band 5[†]	190.8645... 194.5855 & 202.8645... 206.5855	0.051	0.92	0.31 × 0.26	44	2.9	0.04	5
Band 6[‡]	222.9465... 226.6665 & 237.4465... 241.1665	0.069	1.89	0.20 × 0.18	38	2.5	0.03	10
Band 7[*]	279.2225... 282.9425 & 291.2225... 294.9425	0.102	1.52	0.17 × 0.12	30	2.1	0.02	10
Band 8[**]	403.9195... 407.6395 & 415.9195... 419.6395	0.210	2.61	0.17 × 0.16	21	1.5	0.02	20

Notes. Column 1: ALMA Band used for the tuning. Column 2: frequency set-up, contiguous between the triple dots, and with the lower and upper sidebands separated by an ampersand. Column 3: sensitivity of the observations across the complete ≈ 7.5 GHz. Column 4: average sensitivity of the observations across a 35 km s^{-1} bin. Column 5: average beam size in units of arcsec by arcsec. Column 6: field of view in units of arcsec, this corresponds to the diameter where the primary beam reaches 0.35 of its peak value. Column 7: maximum recoverable scale in units of arcsec. Note that none of our sources extend beyond this scale. Column 8: pixel size in units of arcsec. Column 9: calibration uncertainty in flux density measurements. Following Bakx & Conway (2024), our observations are conducted using the Local Oscillator (Bryerton et al. 2013) and the following receivers: [@]The Band 3 performance is documented in Claude et al. (2008) and Kerr et al. (2014). [#] The Band 4 performance is documented in Asayama et al. (2014). [†]The Band 5 performance is documented in Belitsky et al. (2018). [‡]The Band 6 performance is documented in Ediss et al. (2004) and Kerr et al. (2004, 2014) [*]The Band 7 receiver performance is reported in Mahieu et al. (2012). [**] The Band 8 receiver performance is reported in Sekimoto et al. (2008).

lines. Bands 5, 6, and 7 are sensitive to molecular lines such as water, and absorption lines including CH^+ and OH^+. The highest frequency Band 8 is able to target atomic emission lines, such as [O I] (2060 GHz) and [N II] (1461 GHz).

This shared calibration step is only enabled for sources within 10 deg on the sky for configurations below ∼ 3 km (C43-6 or lower), while for longer baselines this condition is more stringent (< 1 deg). This places a rough limit on the maximum resolution between 0.3 and ∼0.07 arcsec for Bands 3–8, respectively. Given the spatial extent of DSFGs, any higher resolution could run into problems with maximum resolvable scales and the dilution of emission across the increasing number of beams.

The ALMA observations were carried out in Cycle 8 between 2021 November and 2022 July (Program ID: 2021.1.01628.S; PI: T. Bakx). Table 2 shows the exact tuning frequencies used in this ANGELS pilot, together with the observing depth across the entire image (i.e. the continuum depth), and across 35 km s^{-1} bins. A quasar was used for the complex gain calibration (J2359−3133), while another quasar was used for bandpass calibration (J2258−2758). We found this exact set-up of the spectral windows by parametrizing each of the spectral set-ups of the bands by their starting frequency. Appendix Fig. A1 compares each potential tuning with ALMA to the total number of lines that can be targeted. The bottom part of the graph shows the atmospheric transmission, normalized between 0 and 1, to indicate the effect of tuning at this specific frequency. The variability in the observable number of lines with frequency reveals an important fact: the simple act of optimizing the tuning towards the known spectroscopic redshifts can triple the number lines within any snapshot program.

2.3 Data reduction

All data were processed using the COMMON ASTRONOMY SOFTWARE APPLICATIONS (CASA) package (McMullin et al. 2007; CASA Team et al. 2022). The pipeline calibration of the visibility data were first restored using the standard scripts from the ALMA Science Archive and using CASA version 6.2.1. After this, the data were imaged using TCLEAN. The continuum images were created with CASA version 6.2.1, while the image cubes were created with CASA version 6.4.1.

We initially created image cubes binning the channels by a factor of 16 to identify detectable spectral lines from each target within each spectral window (corresponding to a channel width between 50 and 15 km s^{-1} between Bands 3 and 8, respectively). After this, we subtracted the continuum from the visibility data for each field and spectral window containing a detectable spectral line. We also had spectral windows that covered spectral lines that were expected to be present based on the redshifts of the individual targets from Urquhart et al. (2022) but that were not detected. In these situations, we identified all channels that lied within a 0.4 GHz region centred on the expected frequency of the spectral line for each target as potentially containing line emission and used all channels not covering the potential line emission to measure and subtract the continuum from the visibility data. These continuum-subtracted image cubes were then used for the final analysis. The channels in the visibility data without the continuum subtraction that were identified as not containing emission were used to create the final continuum images.

Natural weighting was used to create the continuum images, but when creating the image cubes, we set the weighting to BRIGGSBWTAPER, which is a variant of Briggs weighting that makes adjustments for variations in the beam size with frequency, and we set the robust factor to 2, which is equivalent to natural weighting and which is best for detecting faint emission in ALMA data. To further optimize the images for the detection of faint line or continuum emission, we used the Hogbom deconvolver. Additionally, a *uv* taper of 0.05 arcsec was applied to remove noise with very high spatial frequencies. The channel width in the image cubes was adjusted to attempt to maximize the peak signal-to-noise ratio (SNR) of the beam while preserving as much spectral structure of the line as possible. The final images have pixel scales that sample the full width at half-maxima of the beams by at least five times; the specific pixel scales and reconstructed beam sizes are listed in Table 2. This table also lists the fields of view in the ALMA images in each band, the maximum recoverable scales (MRS), and the calibration uncertainties, which are based on information from the ALMA Technical Handbook[2] (Cortes et al. 2023).

3 RESULTS

The ANGELS observations resulted in a high-angular resolution spectral perspective on 16 *Herschel* galaxies, across the frequency range from 200 to 2000 GHz in the rest frame. In this section,

[2]Available from https://almascience.eso.org/documents-and-tools/cycle10/alma-technical-handbook.

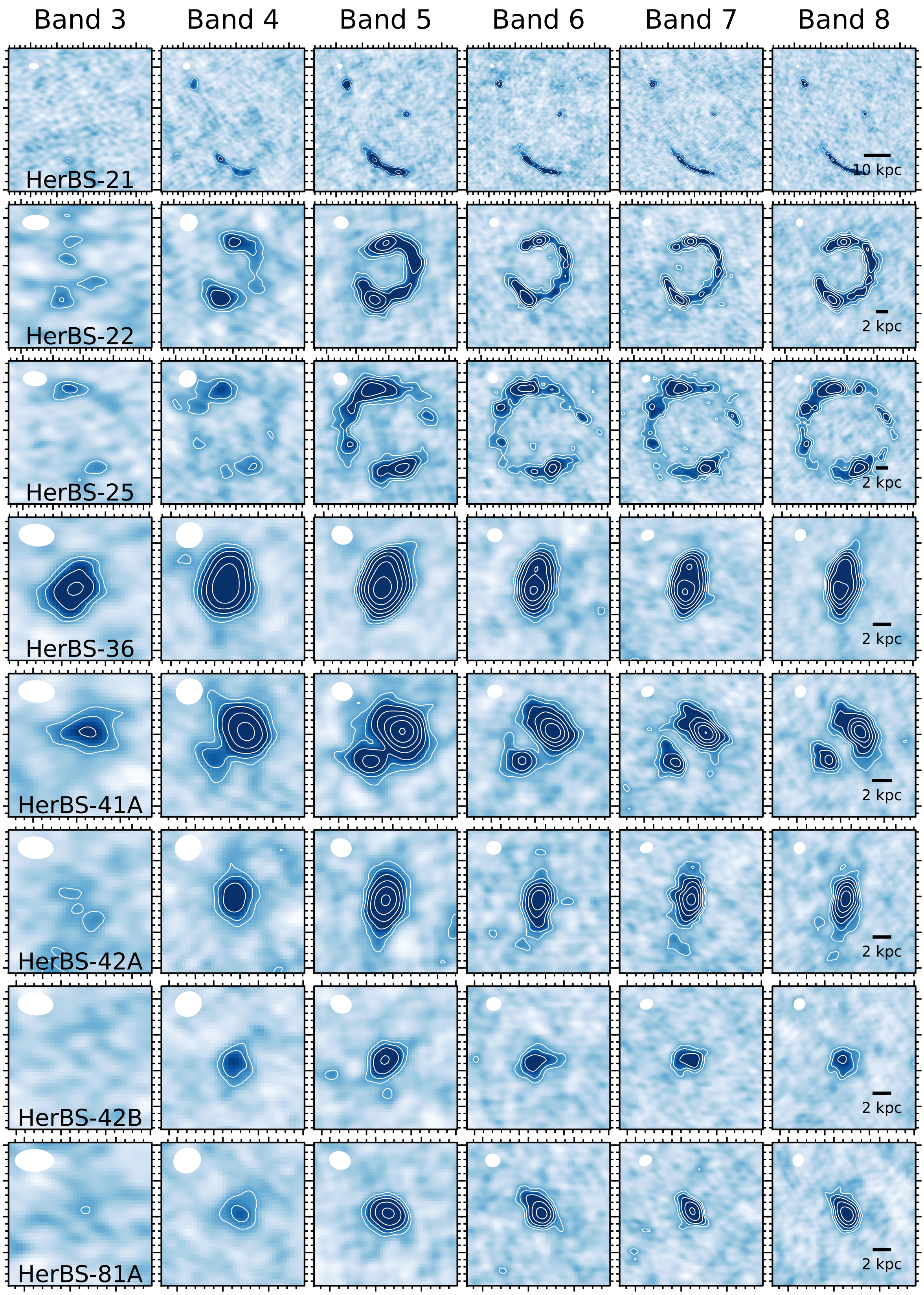

Figure 3. The dust continua of HerBS-21 through -81A are shown as white contours (3σ, 5σ, 8σ, and beyond, following the Fibonacci sequence, see Table 2 for the σ-values) between Bands 3–8 from left to right. The beam size is shown as a white ellipsoid in the top left, and the scale bar is shown in the bottom right of the Band 8 image, using the proper distance at the redshift of the *Herschel* source. The images are scaled to contain the source, using a 7 arcsec^2 post-stamp for HerBS-21 field, a 3 arcsec post-stamp for HerBS-22 and -25, and a 2 arcsec post-stamp for HerBS-36 through 81A. For fair comparison, we show the images before primary-beam corrections, as these effects could vary across the different bands.

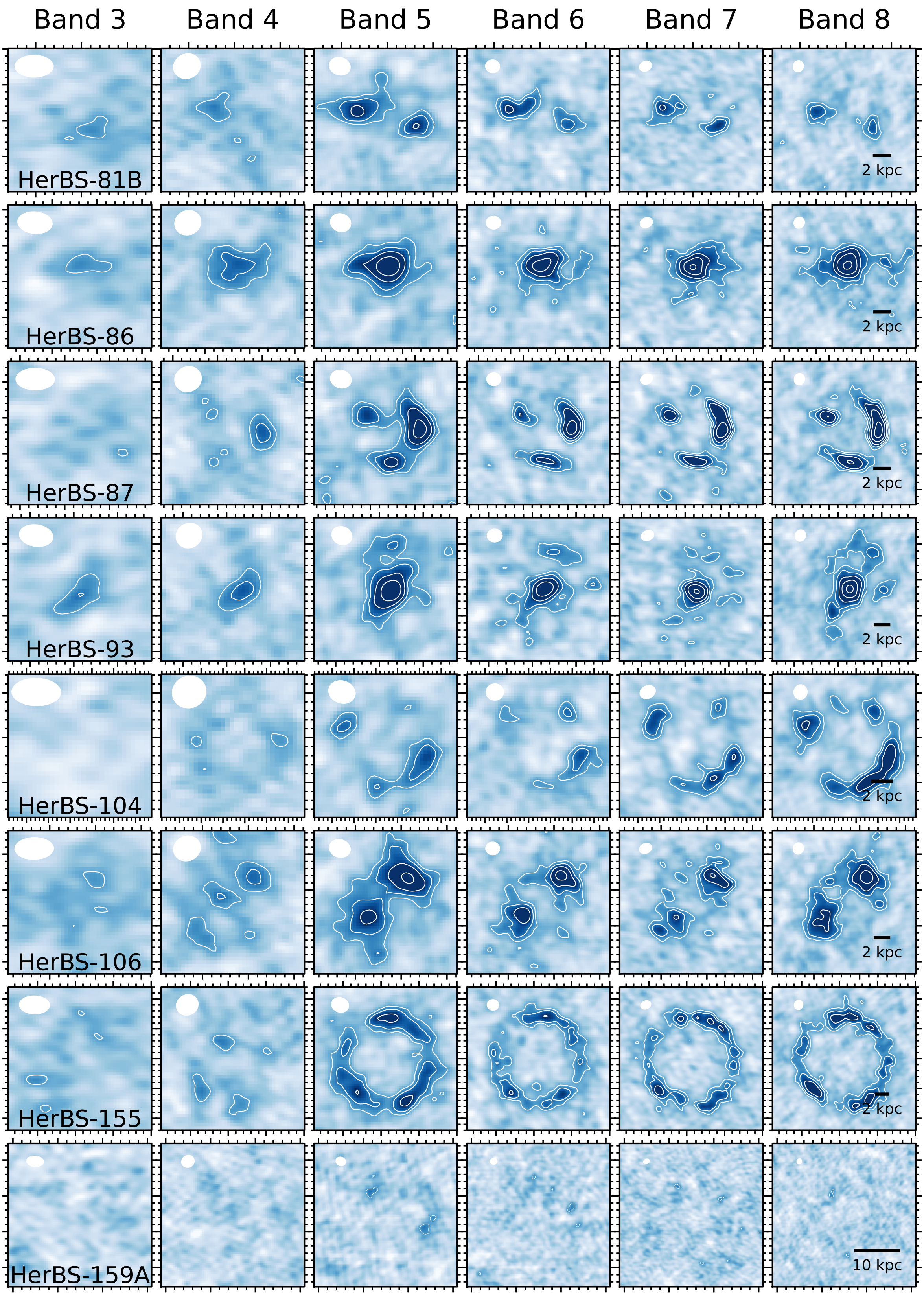

Figure 3. (continued) The dust continua of HerBS-81B through -159A are shown as white contours (3σ, 5σ, 8σ, and beyond, following the Fibonacci sequence, see Table 2 for the σ-values). The images are scaled to contain the source, using a 2 arcsec^2 post-stamp for all fields, except a 1.6 arcsec^2 post-stamp for HerBS-104, a 2.4 arcsec^2 post-stamp for HerBS-155, and a 4 arcsec^2 post-stamp for HerBS-159A. For fair comparison, we show the images before primary-beam corrections, as these effects could vary across the different bands.

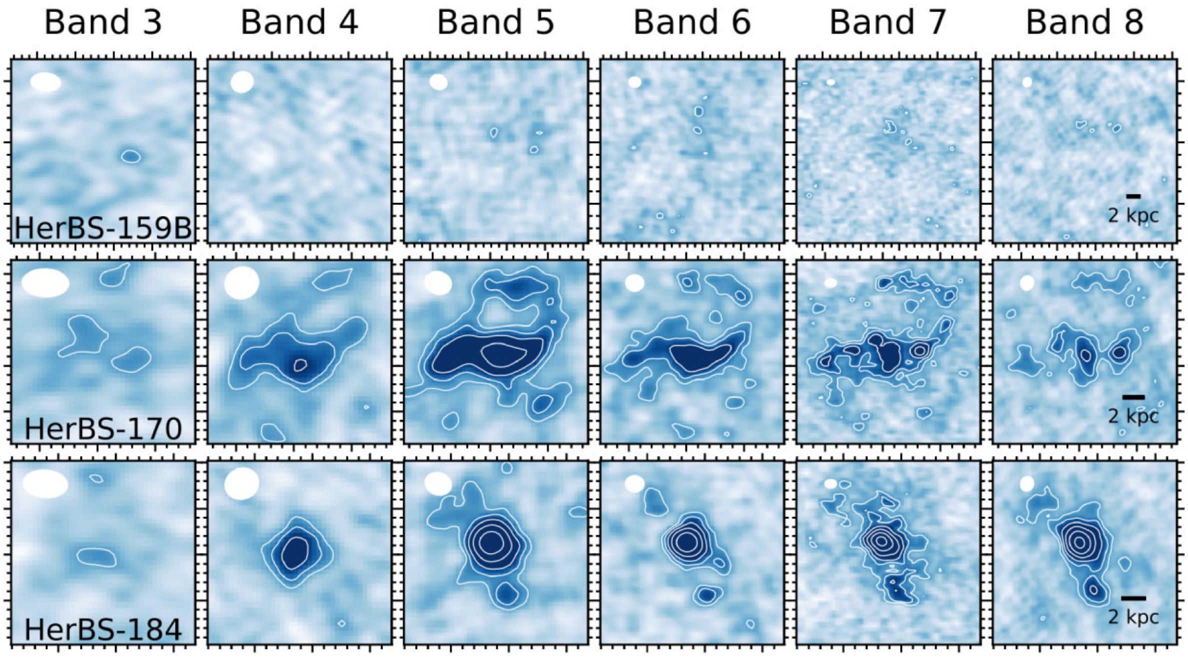

Figure 3. (continued) The dust continua of HerBS-159B through -184 are shown as white contours (3σ, 5σ, 8σ, and beyond, following the Fibonacci sequence, see Table 2 for the σ-values). The images are scaled to contain the source, using a 3 arcsec^2 post-stamp for HerBS-159B, and a 2 arcsec^2 post-stamp for HerBS-170 and -184. For fair comparison, we show the images before primary-beam corrections, as these effects could vary across the different bands.

we present the main results on the underlying dust continuum (Section 3.1) and the line measurements (Section 3.2).

3.1 Continuum snapshots

Fig. 3 displays the dust continuum images for all the sources that have complete coverage in Bands 3–8. We further present sources separated beyond the primary beams of the higher frequency bands in Appendix Fig. B1. The sources have starkly varying morphologies, with lensing structures such as (partial) *Einstein* rings seen for HerBS-21, -22, -25, -36, -41A, -87, -104, and -155. HerBS-21 has a much more complicated gravitational lensing morphology when compared to the other sources, which are single galaxy–galaxy lensed systems (see Section 7.1). Other sources are resolved into bright single components, such as HerBS-42A and -B, -81A, -86, -93, -170, and -184. HerBS-81B and -106 (and potentially -170) are resolved into multiple components on the scale of < 1.5 arcsec, and were seen as individual clumps in the BEARS observations (discussed further in Section 7.2). Since the MRS is between 4 and 1.5 arcsec for the ALMA observations (see Table 2), we expect this to play little effect in the final imaging quality.

Interestingly, HerBS-159A and -B are not seen in the imaging. For these sources, we create tapered images in Fig. 4 to see if any emission of these 500 µm-bright sources is seen at these longer wavelengths. Tapering reveals the dust emission in Bands 5 and beyond. For HerBS-159A, the emission appears to be split across several sources separated at ~ 1 arcsec, while HerBS-159B appears to be a single bright component. We discuss the significance of these types of sources in Section 7.3.

The morphology of the ANGELS sources varies across the different bands, and provides a strong argument towards a multiband interpretation of dusty galaxies, particularly if only lower frequencies are available. For example, even though the observations are at high enough resolution in Bands 3 and 4, the lensing nature of HerBS-41A remained unclear until the convincing arcs seen in Bands 7 and 8.

We provide the continuum spectral energy distribution fitting in a subsequent paper (Bendo et al., in preparation) that will investigate the nature of dust in these ANGELS sources. In this paper, we employ two methods for calculating the far-infrared luminosity, which are broadly in agreement between one another (Bendo et al. 2023). First, where it is necessary to discuss the resolved luminosity (e.g. in the resolved star formation law; Section 6.1), we use a single-temperature modified blackbody estimate of the far-infrared luminosity of these sources with 35 K and $\beta_{\rm dust} = 2$ (Bendo et al. 2023) fit to the Band 7 flux densities of the sources, which typically have the highest SNR. Secondly, in scenarios where the bulk luminosity is important (e.g. for the total intrinsic luminosity after lensing correction; Section 6.2), we use the *Herschel* photometry to re-derive the luminosity by fixing the redshift to the $z_{\rm spec}$ (Bakx et al. 2018, 2020b) assuming the spectrum of the famous Eyelash galaxy (see e.g. Ivison et al. 2016). For sources resolved into multiple components, we distribute this luminosity based on the relative flux densities of the individual components as measured in Band 7. Note that this implicitly assumes these sources have the same colour temperature and are at the same redshift. In Appendix D, we provide the infrared luminosities derived using three methods of fitting, including the Eyelash template, the *Herschel*-derived template from Pearson et al. (2013) and Bakx et al. (2018, 2020b), and a single-temperature blackbody. The latter also provides an estimate for the dust temperature and dust mass. As a sanity check, when we investigate the luminosity of the sources based on the total Band 7 flux both assuming a constant dust temperature and a best-fitting dust temperature, we find a comparable, albeit uncertain (a standard deviation of ~ 50 per cent) luminosity when compared to the second method, with a better fit of the constant dust temperature ($= 35$ K) when compared to the best-fitting dust temperature. A more thorough investigation of the ALMA and *Herschel* dust properties is planned for a subsequent paper (Bendo et al., in preparation).

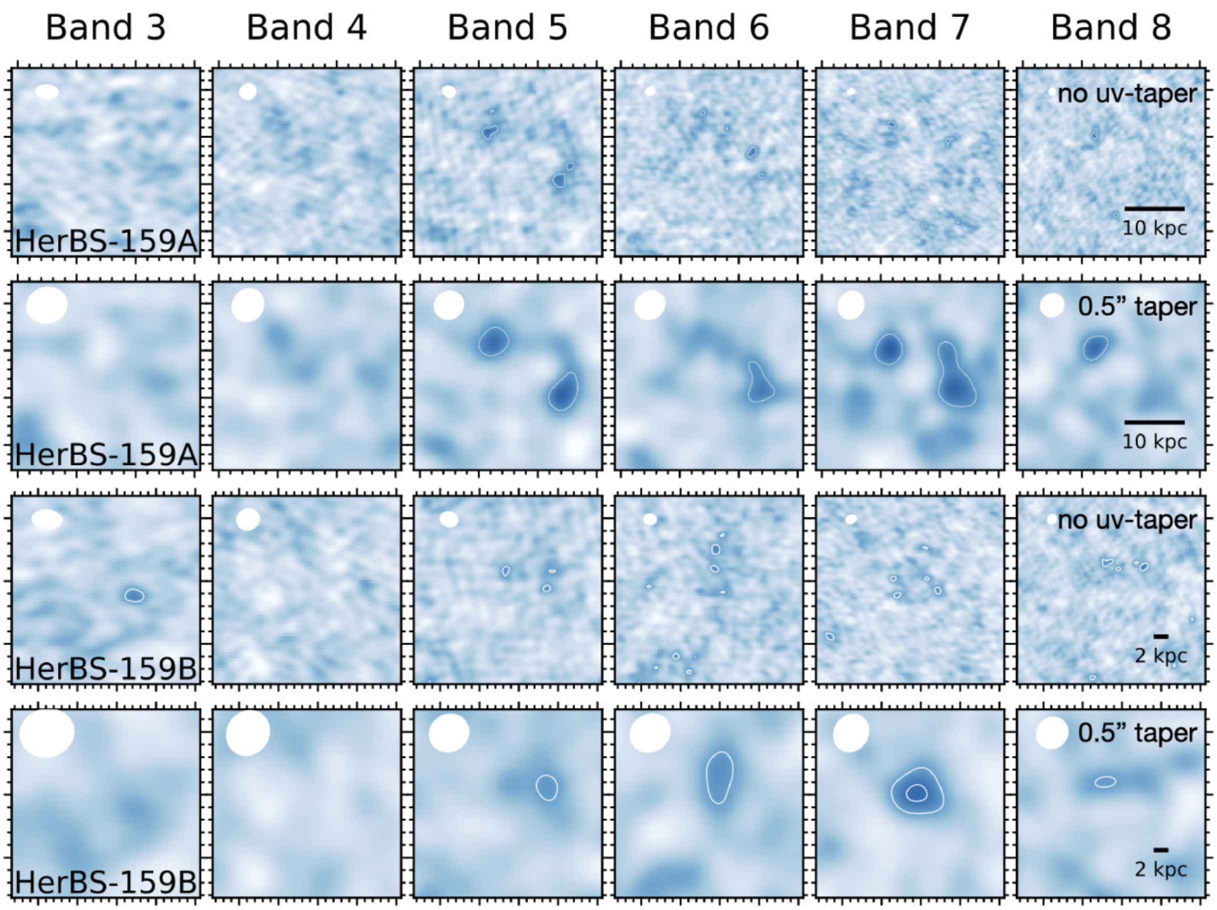

Figure 4. HerBS-159A and -B are undetected in the natural weighted maps. Instead, we create tapered images with an additional weighting term on the uv-data of 0.5 arcsec. These reveal the extended structure missed at higher resolutions. HerBS-159A appears to consist of multiple components separated by ∼ 1 arcsec, while HerBS-159B appears to be a single bright component. Similar to Fig. 3, the dust continua are shown as white contours (3σ and 5σ) between Bands 3–8 from left to right. The beam size is shown as a white ellipsoid in the top left, and the scale length is shown in the bottom right of the Band 8 image. For fair comparison, we show the images before primary-beam corrections, as these effects could vary across the different bands.

3.2 Line measurements

The main aim of this study is to perform efficient line surveys across a large sample of galaxies in an effort to out-perform the point-tune-and-shoot style observations that are the norm for extragalactic surveys with ALMA. We present the line results in Table C1 and show the spectral line profiles in Appendix Fig. C1.

These sources are mostly resolved systems with line emission extending across multiple beams. Calculating the total line fluxes is therefore a non-trivial exercise, and we use the following procedure on the image-plane data to collect the properties of the emission lines across our spectrum.

In an effort to extract the total line fluxes, we tried several flux measurement techniques, including 2σ moment-0 apertures (biased to including false positive 2σ features and missing the $0\sigma - 2\sigma$ regions on the edges of the contours; Stanley et al. 2023) and dust continuum apertures (presuming dust and star formation are coincident with line emission). Instead, we combine these methods into an algorithm that matches the highest fidelity (band 7) observation to the cube resolution, and extending the 2σ continuum contour by up to three beams of the cube. Effectively, we test the best aperture for each line to include as much flux as possible, favouring larger apertures to measure the total flux as accurately as possible at the potential cost of SNR.

For sources where the apertures cover a large number of beams, an additional aperture selection criterion is used, based on the 2σ contours of the moment-0 map before extending the aperture by up to three beams. This step guides the aperture to match the line emission, but also reduces the effect of p-hacking. Note that, in the case of absorption lines, typically no additional spatial smoothing is used, since the expected absorption is only seen at the location where continuum emission is seen.

The subsequent spectrum is then fitted with a single Gaussian profile to provide a line estimate. We list all line properties in Table C1, and provide the moment-0 and spectra of the detected lines in Appendix Fig. C1, where we further highlight the thresholds used to create the aperture (i.e. $\sigma_{\rm cont}$, $\sigma_{\rm mom-0}$, and $N_{\rm beam}$).

4 LENSING

Nine sources show lensing features in their dust continuum. As gravitational lensing is a purely geometric process, it is achromatic, and we can use the uv-based lensing reconstruction of Band 7 – which typically has the highest SNR detections for our sample – to deduce the properties of our galaxies across the entire frequency range.

4.1 Lensing reconstruction

In this section, we give a general description of the methodology and models that we used to obtain source-plane reconstructions. We perform this lens modelling (lens mass model optimization and

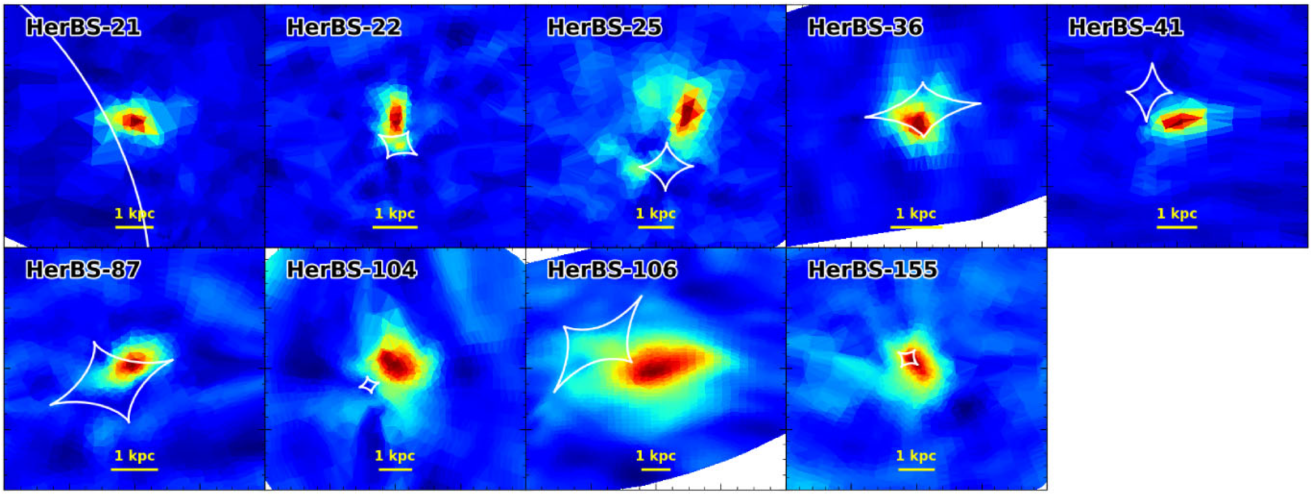

Figure 5. Source-plane reconstructions for the nine confirmed strong lenses in our sample. The grey curve in each panel of the figure shows the caustic curve, while the white scale bar at the bottom corresponds to a physical scale of 1 kpc.

background source reconstructions) using the open-source software PYAUTOLENS, which is described in Nightingale & Dye (2015), Nightingale, Dye & Massey (2018), and Nightingale et al. (2021) and builds on the methods from previous works in the literature (e.g. Warren & Dye 2003; Suyu et al. 2006). We perform lens modelling in the visibility (i.e. uv) plane (e.g. Enia et al. 2018; Maresca et al. 2022; Powell et al. 2021).

The analysis pipeline is broken down in two phases. In the first phase we fit a parametric model for the source (i.e. a Sérsic profile) while in the second phase we switch to pixelated reconstructions. In both phases, the mass model for the lensing galaxy is a singular isothermal ellipsoid (SIE).

The analysis pipeline was divided into two phases for both technical and observational reasons. Technically, the non-linear search involving a pixelated reconstruction, which is computationally intensive, benefits from a robust initial estimate of the lens's mass model to converge more efficiently. While a parametric model of the source may not fully capture the complexity of the background source, it provides a reliable initial mass model. This model, derived from the parametric phase, serves as a prior for the subsequent pixelated phase. Observationally, at higher resolutions, complex structures in some sources emerge that cannot be accurately modelled with a parametric approach. In such cases, relying on a parametric model could introduce biases in the lens parameters and, by extension, in the derived magnification factors, which are primarily what we aim to determine from the lensing analysis in this paper. In the subsections that follow we give more details about the various models that are used in our analysis.

4.1.1 Lens

The convergence of the SIE model is defined as,

$$\kappa(x, y) = \frac{1}{1+q}\left(\frac{\theta_{\rm E}}{\sqrt{x^2 + y^2/q^2}}\right)^{-1}, \tag{1}$$

where q is the axis ratio (minor to major axis) and $\theta_{\rm E}$ is the Einstein radius. Our model also has additional free parameters that control the position of the centre $(x_c,\ y_c)$ and its position angle, θ, which is measured counterclockwise from the positive x-axis. In practise, we parametrize the model's axis ratio, q, and position angle, θ, in terms of two components of ellipticity,

$$e_1 = \frac{1-q}{1+q}\sin(2\theta)\ , \quad e_2 = \frac{1-q}{1+q}\cos(2\theta)\ , \tag{2}$$

which help to prevent periodic boundaries and discontinuities in the parameter space, which are associated with the position angle and axis ratio, respectively. Finally, our model also has an additional component to model the potential presence of external shear and/or any mass distributions with more complexity than a single SIE (Etherington et al. 2023). This is typically described by two parameters, its magnitude, $\gamma_{\rm ext}$, and position angle, $\theta_{\rm ext}$, but here we express them in terms of $\gamma_{\rm ext,1}$ and $\gamma_{\rm ext,2}$, with relations:

$$\gamma_{\rm ext} = \sqrt{\gamma_{\rm ext,1}^2 + \gamma_{\rm ext,2}^2}\,, \quad \tan 2\theta_{\rm ext} = \frac{\gamma_{\rm ext,2}}{\gamma_{\rm ext,1}}\,. \tag{3}$$

4.1.2 Source

As mentioned before two different approaches are used to represent the background source. The first approach is to use a parametric profile, specifically a Sérsic (1963), which is the most common type of profile that is used to describe the light distribution of galaxies. This has a functional form that is given by,

$$I(r) = I_{\rm e}\exp\left\{-b_{\rm n}\left[\left(\frac{r}{r_{\rm e}}\right)^{1/n} - 1\right]\right\}, \tag{4}$$

where r_e is the effective radius, $I_{\rm e}$ the intensity at the effective radius, n the Sérsic index, and $b_{\rm n}$ a constant parameter that only depends on n (Trujillo et al. 2004).

The second approach is to use a pixelated grid to reconstruct the source's surface brightness distribution, independent of the parametric method described above. For this, we use an irregular Voronoi mesh grid (e.g. Nightingale & Dye 2015). This irregular grid has the advantage that adapts to the magnification pattern in the source plane, meaning that more source-plane pixels are dedicated to regions with higher magnifications (since the resolution will also be higher in these regions, roughly scaling as $\mu^{-1/2}$) compared to regions with lower magnification. In addition, it is preferred in cases where the morphology of the background source is complex and can not be described with simple parametric profiles (e.g. Sérsic). When reconstructing a source on a pixelated grid it is also

Table 3. Intrinsic properties of ANGELS sources.

Source	Magnification	Intrinsic source radii	
	$\mu \pm \sigma_\mu$	[mas]	[kpc]
HerBS-21	9.0 ± 1.8	121^{+13}_{-10}	$0.924^{+0.100}_{-0.080}$
HerBS-22	18.8 ± 3.7	38^{+1}_{-1}	$0.301^{+0.009}_{-0.009}$
HerBS-25	9.2 ± 1.8	279^{+46}_{-27}	$2.217^{+0.368}_{-0.222}$
HerBS-36	4.1 ± 0.8	86^{+3}_{-3}	$0.672^{+0.027}_{-0.023}$
HerBS-41	2.6 ± 0.5	90^{+2}_{-2}	$0.633^{+0.018}_{-0.018}$
HerBS-42A*	*1.0*	265 ± 9	2.02 ± 0.07
HerBS-42B*	*1.0*	287 ± 38	2.19 ± 0.29
HerBS-81A*	*1.0*	301 ± 70	2.33 ± 0.54
HerBS-81B*	*1.0*	322 ± 63	2.64 ± 0.52
HerBS-86*	*1.0*	422 ± 28	3.47 ± 0.23
HerBS-87	8.7 ± 1.7	49^{+3}_{-2}	$0.417^{+0.024}_{-0.021}$
HerBS-93*	*1.0*	284 ± 24	2.36 ± 0.20
HerBS-104	6.3 ± 1.2	83^{+5}_{-2}	$0.721^{+0.046}_{-0.024}$
HerBS-106	2.3 ± 0.4	239^{+16}_{-15}	$2.001^{+0.131}_{-0.129}$
HerBS-155	28.3 ± 5.6	71^{4}_{-3}	$0.553^{+0.030}_{-0.027}$
HerBS-159A*	*1.0*	1415 ± 530	11.9 ± 4.48
HerBS-159B*	*1.0*	433 ± 189	3.65 ± 1.60
HerBS-170*	*1.0*	952 ± 67	6.64 ± 0.47
HerBS-184*	*1.0*	246 ± 14	2.03 ± 0.12

Notes. Column 1: source name. Column 2: magnification and uncertainties. Numbers in italics assume no lensing magnification as is apparent in the ∼ 0.1 arcsec Band 7 observations. Column 3: the source-plane size estimates in units of milliarcseconds. Column 4: the source-plane size estimates in units of kpc. The source sizes were calculated for both Sérsic profiles of the lensed sources, which is left as a free parameter. The IMFIT routine is used for the non-lensed sources, which are indicated by a star (*).

necessary to introduce some form of regularization in order to avoid overfitting (e.g. Suyu et al. 2006). In this work, we use a constant regularization scheme, where the level of regularization is controlled by the regularization coefficient, $\lambda_{\rm reg}$.

As seen in Fig. 5, some sources display extended structures at faint flux levels, possibly indicating interactions. However, the majority of sources show simple morphologies, in particular at the brighter flux levels. We can therefore use our best-fitting parametric profiles to get an estimate of the sizes of the star-forming regions, which are presented in Table 3. For the same reason we also use the parametric fits to estimate magnifications, also presented in Table 3 as the ratio of the image-plane to source-plane flux.

4.2 Multiwavelength perspective

In total, six ANGELS fields have *Hubble* imaging from surveys reported in Borsato et al. (2023), shown in Fig. 6. These *Hubble* observations use *JH*-band snapshot-style observations between 7 and 11 min to reveal the foreground structure of these galaxies. The near-complete Einstein rings of HerBS-22, -87, and -155 are shown to lie directly behind foreground lensing galaxies. In fact, HerBS-155 was already identified as a gravitational lens through a foreground removal study (Borsato et al. 2023), where the lensing features were already apparent in the pre-subtracted images. They find a comparable lensing magnification ($\mu \approx 20 - 21$) to the ALMA-based lensing magnification of $\mu = 28.3 \pm 5.6$, although they are derived independently. The astrometry of the *Hubble Space Telescope* (*HST*) images is corrected using *Gaia* stars and the imaging is thus accurate to < 0.1 arcsec. Given the high astrometric accuracy of ALMA,[3] the relative astrometric accuracy between *HST* and ALMA imaging thus lies below 0.1 arcsec. The sources with extended emission (HerBS-159A and -B) show a complex foreground system. This suggests that extended emission, particularly in HerBS-159A, could be caused by gravitational lensing extending across multiple arcseconds. Unfortunately, the SNR of HerBS-159A does not allow for a robust lensing model to test this hypothesis.

On top of the *HST* fields, seven *Herschel* fields (nine ALMA sources including the multiplicity) have *Spitzer* imaging. Note that two of these sources (HerBS-170 and -184) also have *HST* imaging, shown in Fig. 7. The image point spread functions (PSFs) are wider, complicating the astrometric correction (∼ 1 arcmin), and as a result, provide a less clear picture of the lensing nature of several galaxies. HerBS-25 and -41A, together with the *HST*-identified *Einstein* rings, are shown to lie directly on top of a foreground galaxy. HerBS-36 is likely lensed with a very small *Einstein* radius (predicted down to ∼ 0.2 arcsec, Amvrosiadis et al. 2018). The continuum emission is a barely resolved clump with a double-peaked internal structure of ≈ 3 × 7 kpc, and the southern clump appears to arc (see Appendix Fig. F1). The lensing nature of the HerBS-42, -81, and -184 systems remain unclear. The emission of HerBS-42A and -B coincide with *Spitzer*-bright emission, although the emission does not appear to resemble an obvious lensing feature. The double emission peaks of HerBS-81B are close to a *Spitzer*-imaged source, although the geometry is not reminiscent of a lensing system. While the *HST* image of HerBS-184 does not suggest a bright foreground system, *Spitzer* shows a bright source adjacent to the ALMA emission. Meanwhile, the continuum emission of HerBS-184 is clumpy and extended, although the lack of a counterimage likely rules out lensing. HerBS-170 is not seen in *HST* imaging, although some faint *Spitzer* emission appears visible at the position of HerBS-170. The spatial association of nearby objects does not suggest any lensing association. The continuum emission is clumpy and extended, particularly in Band 5 (≈ 10 × 12 kpc; see Table 3). As there is no nearby lensing galaxy seen for HerBS-170, and no counterimage is seen, HerBS-170 is thus likely not lensed.

5 SPECTRAL LINE PROPERTIES

The ANGELS observations have revealed a multitude of lines, consisting of 54 emission and 12 absorption lines, summarized in Table 4. In this section, we discuss the CO spectral line energy distributions (SLEDs; Section 5.1), the in- and outflow distribution of our sample seen in absorption lines (Section 5.2), a brief investigation of the atomic lines (Section 5.3), and a stacked spectrum (Section 5.4). These investigations show the wealth of data from this modest project, and detailed examination of each subject is planned for subsequent studies.

5.1 CO spectral line energy distributions

The rotational transitions of CO have proved a particularly good tracer of the internal structure of DSFGs (e.g. Rizzo et al. 2024, and references therein). CO is the second-most abundant molecule in the Universe after molecular Hydrogen (H_2). However, unlike the a-polar H_2, it emits brightly from gas clouds fuelling star formation and is therefore a useful probe of the available star-forming gas (e.g.

[3]Estimated to lie below 0.05 arcsec for > 5σ observations in Band 7 using equation 10.7 in https://almascience.eso.org/documents-and-tools/cycle10/alma-technical-handbook.

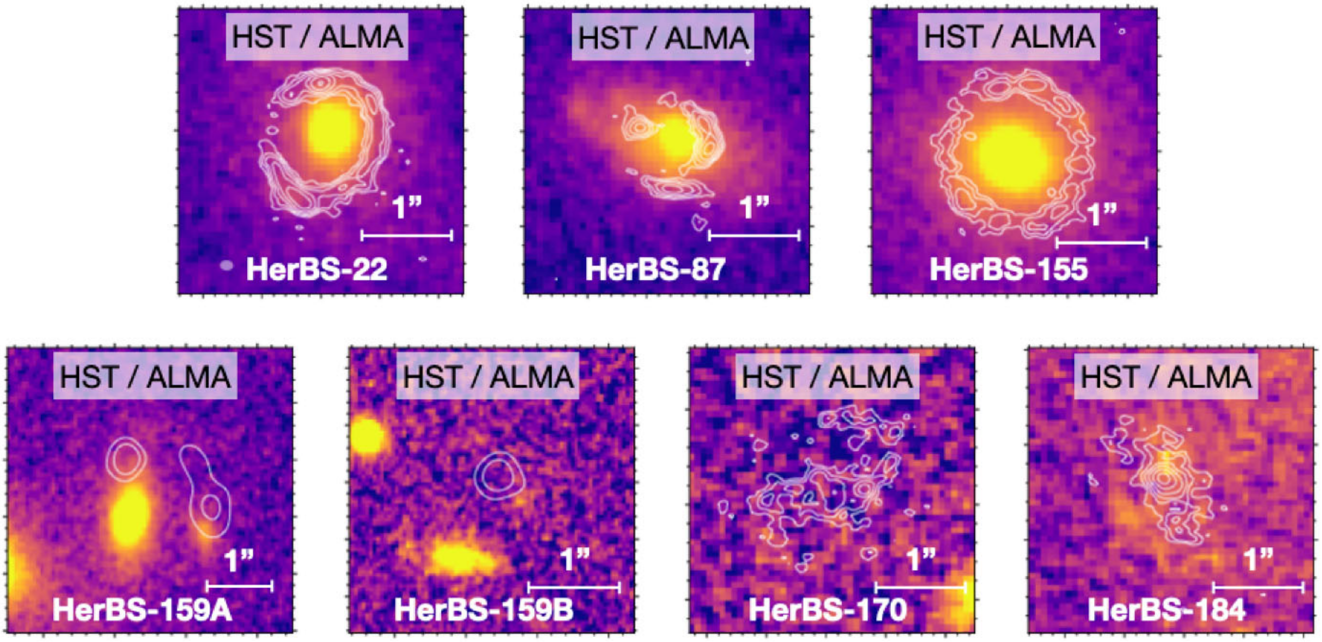

Figure 6. *Hubble JH*-band snapshot data are available for seven of our target galaxies, which provide a high-resolution imaging of several lensed sources, particularly on the top row. The contours of Band 7 continuum emission are drawn at levels of 3σ, 5σ, 8σ, and beyond, following the Fibonacci sequence (see Table 2 for the σ-values). HerBS-159A, a source with extended emission requiring tapering to image, is shown to lie in front of a foreground galaxy which is likely causing a gravitational lensing scenario. Gravitational lensing could be a likely explanation for the extended emission seen in this source.

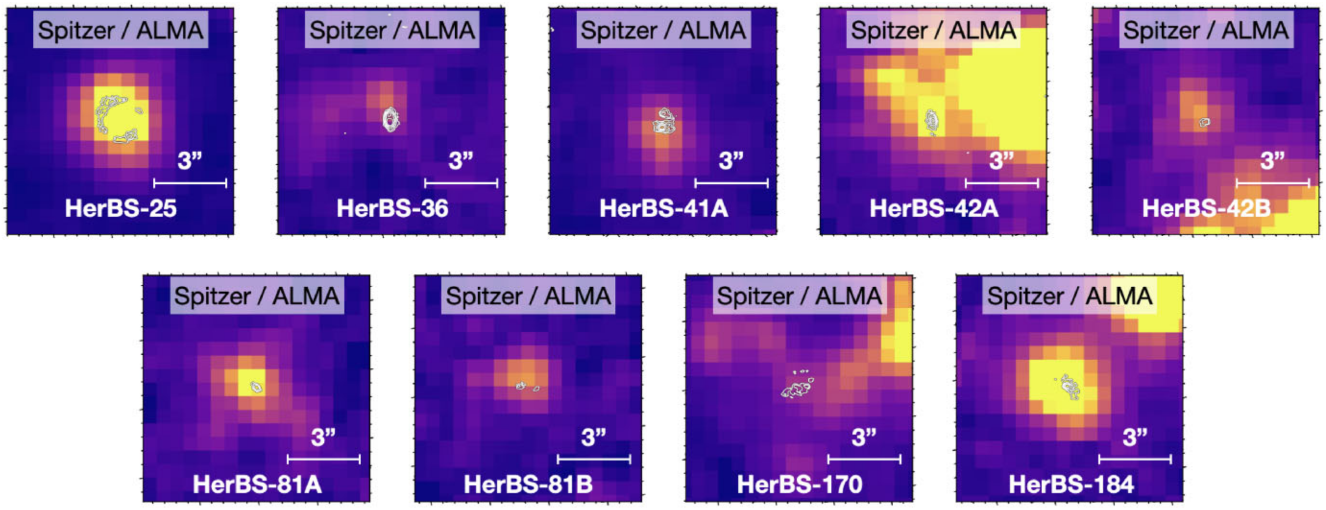

Figure 7. *Spitzer* 3.6 μm data arevailable for seven of our ANGELS fields (nine sources in total), which are shown with the *Spitzer* imaging in the background, and the ALMA Band 7 contours in the foreground (at 3σ, 5σ, 8σ, and beyond according to Fibonacci's sequence). The majority of sources lie close to, or on top of a bright *Spitzer* galaxy. The nature of sources with obvious lensing features (e.g. HerBS-25) is not in doubt, but it is unclear whether sources such as HerBS-170, or -184 are lensed from the current ANGELS and multiwavelength imaging.

Carilli & Walter 2013). Starting at its ground state at 115.270 GHz, CO transitions scale linearly in frequency with higher rotational transitions. These so-called higher J transitions are sensitive to denser, warmer gas, and a comparison between the brightness of different CO transitions can illuminate the properties of the ISM. Recent comparisons of unresolved low-to-mid J CO line ratios, often called SLEDs, find a large diversity among DSFGs (Harrington et al. 2021; Sulzenauer et al. 2021; Hagimoto et al. 2023), ranging from near-thermalized excitation to low-excitation conditions similar to the Milky Way (Fixsen et al. 1999).

The ANGELS observations provide detections and upper limits on both mid-J ($J = 3 - 7$) and high-J transitions ($J = 8 - 18$). This large spread in the CO J levels allows us to qualitatively investigate the presence of dense gas in some of these sources. We show the CO SLEDs in Fig. 8 for the sources with CO lines from ANGELS. We normalize the CO SLEDs against the CO(4−3) observations, and if they are not available, we use the average CO SLED template of Harrington et al. (2021) to translate from the lowest available J transition to CO(4−3), and subsequently normalize against that transition. The choice to normalize to CO(4−3) – which is the most

Table 4. Detected emission lines.

Line	Det.	Sources
	54 emission lines	
CO (3−2)	3	87; 93; 184
CO (4−3)	5	22; 36; 81A; 93; 155
CO (5−4)	5	21; 25; 41A; 42A; 42B
CO (6−5)	7	41A; 81B; 86; 87; 93; 106; 170
CO (7−6)	5	25; 81A; 81B; 86; 106
CO (8−7)	2	36; 155
CO (9−8)	4	21; 41A; 42A; 42B
CO (10−9)	3	25; 36; 41A
CO (11−10)	2	21; 42A
CO (13−12)	1	41A
CO (18−17)	1	41A
[C I] 370 μm	2	93; 106
[C I] 609 μm	3	93; 104; 106
[N II] 205 μm	2	170; 184
[O I] 145 μm	1	41A
H_2O ($2_{0,2} - 1_{1,1}$)	2	41A, 184
H_2O ($2_{1,1} - 2_{0,2}$)	1	25
H_2O ($3_{1,2} - 3_{0,3}$)	1	25
H_2O ($3_{2,1} - 3_{1,2}$)	2	81A; 170
H_2O^+ ($1_{1,1} - 0_{0,0}$)	2	22; 25
	12 absorption lines	
CH^+ (1−0)	3	21; 22; 36
CH^+ (2−1)	1	36
OH^+ ($1_0 - 0_1$)	1	22
OH^+ ($1_1 - 0_1$)	4	21; 41A; 42A; 104
OH^+ ($1_2 - 0_1$)	3	21; 22

frequently detected CO line for our sample – will best allow us to see variations between the CO SLEDs. Similarly, since the galaxies used to derive the CO SLED template from Harrington et al. (2021) are likely similar to the DSFGs in this *Herschel*-selected sample, the CO SLED should be an accurate representation of the typical behaviour of the ANGELS galaxies.

Although the BEARS and ANGELS CO line fluxes agree on the whole, several sources show discrepancies in CO line fluxes, even when observed in the same CO transition. Appendix Fig. E1 shows the velocity-integrated flux densties for the six galaxies with line measurements of the same CO transition in both BEARS and ANGELS, as well as the fluxes extracted from the resolved maps using the same method as BEARS. Careful re-examination of the BEARS (Urquhart et al. 2022; Hagimoto et al. 2023) and ANGELS data suggests these discrepancies could be caused by the different apertures and different approaches taken in the flux extraction. First, in this paper we match the apertures to extract flux despite the additional noise that arises from increased apertures, while previous studies use a curve-of-growth approach that stops velocity-integrated flux density measurements at a 5σ threshold, which appears to bias the observed fluxes low. The comparison between the 5σ and the ANGELS methods on the complete resolved data finds only a 4 ± 8 per cent systemic difference between the two methods (with modestly-larger fluxes in the ANGELS methodology), although there appears a large (45 per cent) variation for each line between the methods. This effect could thus influence the analysis of individual SLEDs. Secondly, we also note that there are consistently found discrepancies between unresolved and resolved studies (Jorsater & van Moorsel 1995; Czekala et al. 2021), such as the flux estimates from ALMA large program ALPINE (ALMA Large Program to Investigate C+ at Early Times) when compared to the resolved CRISTAL study ([CII] Resolved ISM in Star-forming Galaxies with ALMA; Posses et al. 2024), or the flux estimates reported in resolved observations of bright active galactic nuclei (AGNs, Novak et al. 2019). The origin of these issues arise from the deconvolution technique in TCLEAN that produces a combined image of background noise (in units of Jy/dirty beam) and signal (assuming a Gaussian PSF in units of Jy/clean beam). As a consequence, the fluxes from resolved maps might produce a different total flux estimate than those from unresolved observations. Regardless of this caveat, our subsequent interpretation does not depend solely on the BEARS data and we have confidence in our ANGELS-to-ANGELS CO SLED analysis presented below.

As seen for other samples (Yang et al. 2017; Cañameras et al. 2018; Stanley et al. 2023), the CO SLEDs of sources vary strongly, with several sources showing evidence of large reservoirs of warm, dense gas (i.e. HerBS-25, -41A, -42A, -87, and -170), with HerBS-87 tentatively showing steep SLED features similar to the broad absorption line quasar APM 08279 + 5255 (Weiß et al. 2007). Meanwhile, the other sources (i.e. HerBS-21 and -93) follow the trend reported in Harrington et al. (2021). Some of these sources were not observed in high-J CO transitions (HerBS-22 and -86), which impedes us to extend the interpretation towards all sources. Unfortunately, the non-comprehensive nature of this survey means that the current statistics are limited to only a handful of sources.

The ANGELS observations are not deep enough to detect all lines, but they do indicate the broad statistics of the ANGELS Pilot sample, such as the lensing fraction and the ratio of sources with high-J CO lines. The prevalence of dense, warm gas thus appears diverse across distant dusty galaxies, with $\sim 36 \pm 13$ per cent (using a binomial distribution; Gehrels 1986) of sources showing such evidence, which could indicate the presence of an AGN (e.g. van der Werf et al. 2010; Rosenberg et al. 2015). A visual inspection of fig. 5 of Harrington et al. (2021) seems to suggest they have a similar ratio of sources with extreme high-J CO SLEDs. Broadly, their χ^2-minimized turbulence models of the CO SLEDs report five sources with no emission at $J_{\rm up} = 10$, while four sources have bright CO(10−9) emission. 14 ANGELS sources fall between these two categories, indicating there is some dense gas, but that the sample is not dominated by dense gas. Since the SLEDs with emission from higher J CO emission are distributed between lensed and unlensed sources, there does not appear a large effect of differential lensing (Serjeant 2012, 2024), and we note that a thorough characterization of the gas in ANGELS sources requires more extensive modelling beyond the scope of this paper (e.g. Harrington et al. 2021).

5.2 Absorption lines

These dusty galaxies probably lie at the centre of overdensities from quantum fluctuations left over from the big bang (Chiang, Overzier & Gebhardt 2013; Chiang et al. 2017; Casey 2016). As the Universe expanded, filaments funnelled gas onto these central nodes (e.g. Springel 2005; Dekel et al. 2009), allowing for the formation of massive galaxies. This feeding subsequently triggers the onset of feedback mechanisms (Man & Belli 2018) via AGNs heating (Hlavacek-Larrondo, Li & Churazov 2022) and star-formation-driven winds (e.g. Furlanetto & Mirocha 2022). Such dynamics are sometimes seen through wide or asymmetric emission lines, but outflow signatures are difficult to detect against the often-brighter systemic emission in galaxies due to velocity smearing effects and the multiphase nature of outflows.

Absorption lines offer a more unbiased and high-fidelity (Spilker et al. 2018, 2020a) approach at detecting gas dynamics inside

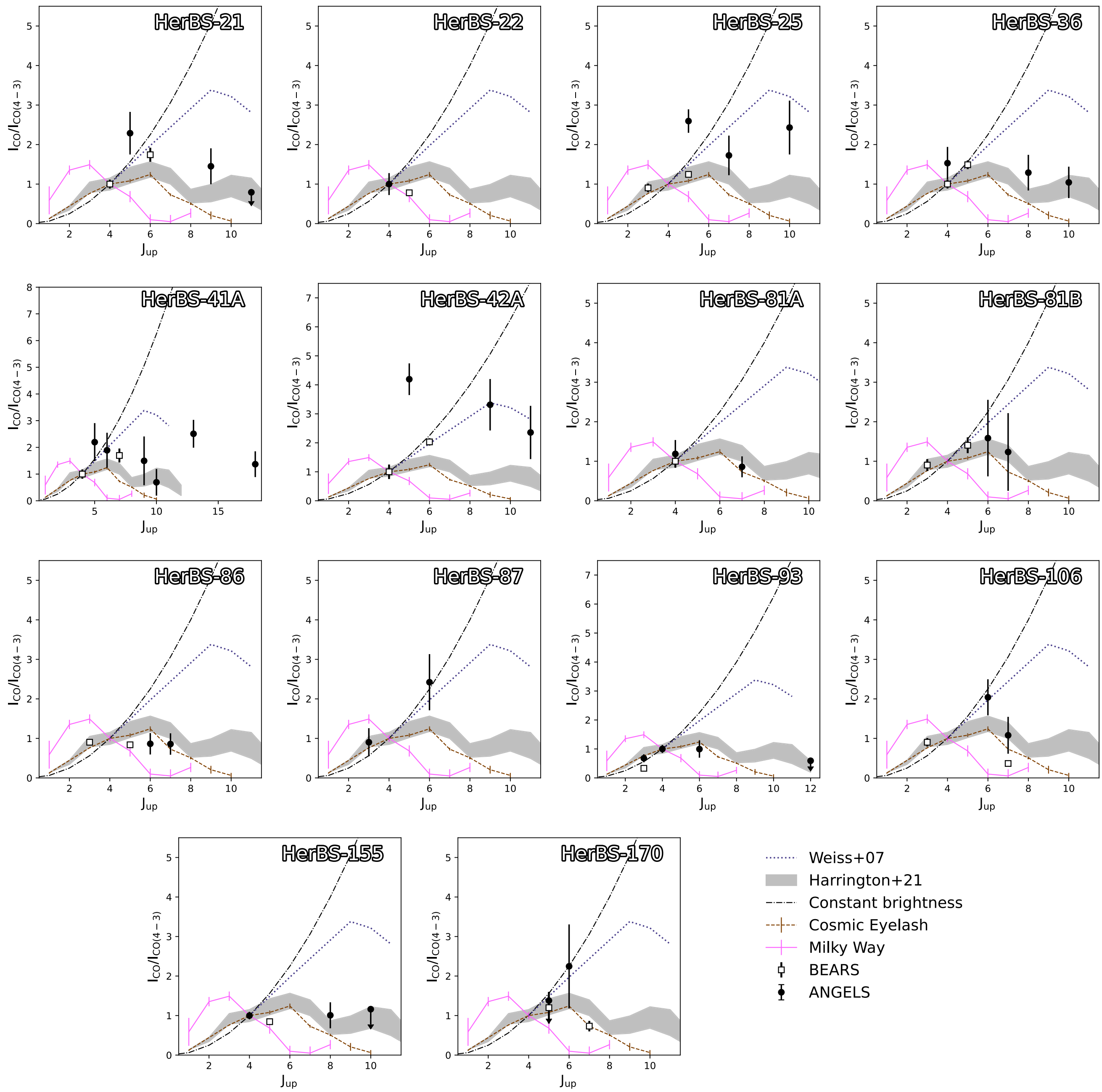

Figure 8. The CO SLEDs of all sources including the new CO line observations from the ANGELS survey and previous values from the BEARS survey (Urquhart et al. 2022; Hagimoto et al. 2023) show the velocity-integrated line intensities of the CO lines normalized against the CO(4−3) line. If the CO(4−3) line is not available, we use the lowest-J CO line and the stacked CO template from Harrington et al. (2021) to derive the expected CO(4−3) emission line. We compare CO SLEDs against the *thermalized* constant-brightness profile ($\propto J^2$; i.e. optically thick in all lines), a highly excited quasar (Weiß et al. 2007), the stacked profile by Harrington et al. (2021), the Cosmic Eyelash (Swinbank et al. 2010; Ivison et al. 2010), and the Milky Way (Fixsen, Bennett & Mather 1999).

galaxies, by searching for the shadow of an absorption line against the bright continuum of dusty sources. Since the absorption feature originates between the bright continuum-emitting regions and us (the observers), any velocity offset immediately reveals whether the gas is in- or outflowing. Consequently, absorption lines are an important tracer of the gas cycle of distant galaxies. To date, a handful of studies have characterized distant dusty galaxies using absorption lines such as the methylidyne cation (CH^+; Falgarone et al. 2017; Indriolo et al. 2018), ionized hydroxyl (OH^+; Berta et al. 2021; Butler et al. 2021, 2023; Riechers et al. 2021), and hydroxyl (OH 119μm; Spilker et al. 2018, 2020b, a).[4] The CH^+ ion is very unstable, formed through strongly endothermic processes, with a dissociation time of around 1 yr. As such, it is only observed where it is created, in strongly shocked regions. Meanwhile, OH^+ traces more diffuse molecular gas feeding star formation. In total, around 40 sources have been observed in submm absorption lines, with around 25 sources showing

[4]Systemic emission of these lines, and neighbouring ones, can interfere with a complete interpretation of these lines, although this effect is often minimal.

absorption lines at velocities outside of the systemic velocity. The majority of these sources show signs of outflowing gas because of rapid star formation or AGN feedback. Meanwhile, inflows of gas are likely occurring as well, although they might be more difficult to image. Observations will need to see down the barrel of inflowing gas filaments, and as a result large samples tracing the delicate balance of gas in- and outflows are still lacking. Without these necessary observational constraints, hydrodynamical models of the gas flows struggle to benchmark mass loading factors (i.e. outflowing gas over SFR) in the distant Universe, which are crucial to test the duration of star-forming events such as the extreme DSFGs studied in this paper.

The bright continuum emission from these galaxies, particularly in Bands 6 and beyond, allowed the detection of twelve absorption lines across six sources (HerBS-21, -22, -36, -41A, -42A, and -104), where two molecules were seen in absorption (CH^+ and OH^+). Several transitions of OH^+ are seen, namely the strong (1_1-0_1) and (1_2-0_1) ground-transitions, as well as the weaker (1_0-0_1) transition for HerBS-22 (see e.g. Berta et al. 2021). Meanwhile, this is only the second time that CH^+(2–1) is seen in the $z > 0.1$ Universe (Bakx et al. 2024), although we note that we might miss the $\Delta V < 0$ km s^{-1} component in the ANGELS observations. The ANGELS observations also covered multiple other lines that are sometimes seen in absorption, including water and ionized water. The sensitivity limits, and the limits to the bandwidth result in non-detections for the fainter species in absorption, particularly given the fainter continuum emission regions (i.e. below Band 5). Similarly, lower significance line features such as P-Cygni might be hard to identify, with tentative cases seen in, for example, CH^+ in HerBS-21.

We show an overview of the absorption lines in Fig. 9 as a function of their redshift and relative velocity compared to the ANGELS-detected CO transitions. The sources are compared against other absorption line studies of $z > 1$ sources (Falgarone et al. 2017; Indriolo et al. 2018; Spilker et al. 2018, 2020a; Berta et al. 2021; Butler et al. 2021; Riechers et al. 2021). Three of the sources (-21, -36, and -104) have evidence of inflowing gas in their absorption lines, although only the relative velocities of HerBS-21 are outside of the error margins. There appears to be a relation between the velocity offset with redshift, transitioning between in- to outflowing gas at $z = 3$. However, since that this collation of data was obtained with different line tracers and observing differently selected sources having a range intrinsic velocity widths, larger samples of observations with similar observational parameters (beam size, observation depth, and tracers) are necessary before such investigations become more robust.

HerBS-21, -22, -36, and -42A have multiple molecules seen in absorption. Even though these can be sensitive to vastly different phases of the ISM and even the circumgalactic medium, they indicate similar velocity offsets relative to the host galaxy. This suggests that the shocked regions seen by CH^+ of HerBS-21 and HerBS-22 lie close to large volumes of low-density molecular gas traced by OH^+. The shocked gas in HerBS-36 seems to be redshifted relative to the bulk molecular gas reservoirs, which could indicate rapid inflows encountering the strong star-forming environments. Given the large velocity widths of these sources (Table 1), these are likely dynamically complex systems, and the small relatively velocity offsets ($|\delta V| < 500$ km s^{-1}) between the absorption and emission lines could obfuscate a more intricate interaction of the in- or outflowing gas and the host galaxy. In order to secure a good interpretation of these sources, deeper and higher resolution observations on absorption lines in these sources are thus important. A more thorough investigation of in- and outflowing gas masses are beyond the scope of this paper, and they are strongly dependent on geometry arguments (e.g. Butler et al. 2023).

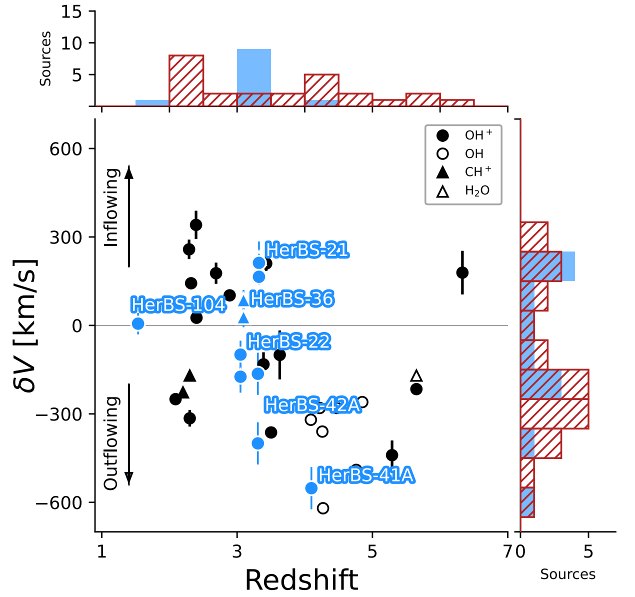

Figure 9. The redshift and relative velocity distribution between absorption lines and their intrinsic velocities from CO observations for the ANGELS sources, shown in blue together with the names of the respective sources. Filled triangles indicate CH^+ detections and circles indicate OH^+ observations. We compare against other high-redshift observations of absorption lines with a velocity shift (Falgarone et al. 2017; Indriolo et al. 2018; Spilker et al. 2018, 2020a; Berta et al. 2021; Butler et al. 2021; Riechers et al. 2021). About half of the sources are seen with inflowing gas, with the other half showing outflowing gas with velocities between ± 300 km s^{-1}. The sources with multiple transitions (HerBS-21 and -22) find similar systematic velocity offsets for both their tracers, suggesting that the shocked gas traced by CH^+ and the more diffuse molecular gas traced by OH^+ originate from similar regions.

5.3 Atomic lines

Large gas clouds surround the ionizing emission of bright young O- and B-stars and shield the outer layers of the highest energy photons. As a result, high-ionization states of specific elements (e.g. hydrogen, helium, oxygen, and nitrogen) mostly emit from the central regions of these photodissociation regions (PDRs; Tielens & Hollenbach 1985), i.e. H_{II} regions. The PDR model of the ISM of galaxies in the distant Universe suggests an onion-like distribution of gas around ionization sources such as bright, massive (O and B) stars, where gas temperature decreases as the column density of neutral hydrogen increases. Lines from forbidden transitions such as atomic oxygen [O I] and singly ionized nitrogen [N II] can trace these higher ionization rates and can be important cooling lines of galaxies (Stacey 2011; Vogelsberger et al. 2020). Current studies of FIR atomic lines typically focus on the low-redshift Universe with now-defunct observatories such as *Spitzer*, *Herschel* (Cormier et al. 2015; Díaz-Santos et al. 2017; Zhang et al. 2018), and SOFIA (Stratospheric Observatory for Infrared Astronomy; Ura et al. 2023), or require high redshifts ($z > 4.5$; Lee et al. 2019, 2021; Le Fèvre et al. 2020; Bouwens et al. 2022; Bakx et al. 2023) to shift these lines in more favourable atmospheric transmission windows. The local studies often only detect a small fraction of the targeted sources, resulting in difficulties in interpreting the sample as a whole (Bonato et al. 2014), while the most distant searches probe a population different than the DSFGs located at the peak of cosmic evolution (Madau & Dickinson 2014). ANGELS offers to increase the number of DSFGs in the

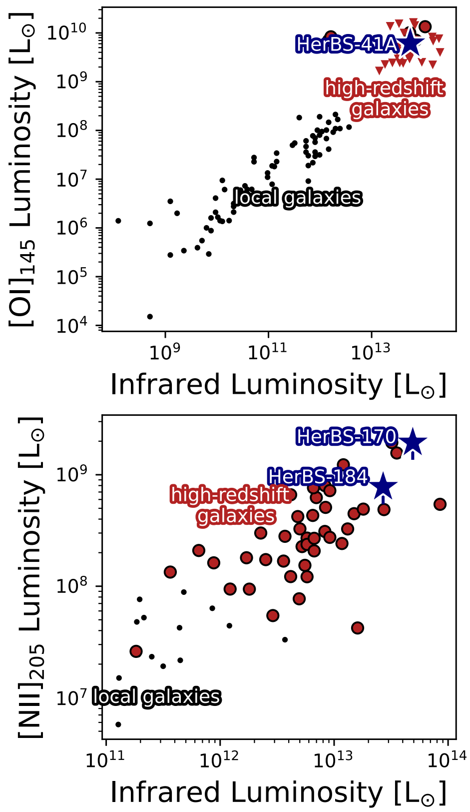

Figure 10. The luminosity scaling relation between [O I] (top) and [N II] 205 μm (bottom) for local galaxies (normal star-forming systems, starbursts, and AGNs; Brauher, Dale & Helou 2008), and high-redshift galaxies (for [O I] Herrera-Camus et al. 2018; for [N II] Cheng et al. 2020; Cunningham et al. 2020, and references therein). HerBS-41A is detected in [O I] with the ANGELS observations, and the detections of [N II] in HerBS-170 and HerBS-184 places them as the brightest Nitrogen emitters in the Universe observed to date. We note that the [O I] flux estimate for HerBS-41A might be an underestimate since we are only sensitive to emission from the $\Delta V <$ 150 km s^{-1}. There is no evidence of far-infrared line deficits, often seen in [C II] high surface SFR galaxies.

cosmic noon with atomic line observations to better characterize the PDR conditions in the most violent starbursts across cosmic time.

The highest frequency bands (Bands 7 and 8) covered atomic lines for four sources, namely [N II] 205 μm for HerBS-170 and HerBS-184 (in Band 7) and HerBS-81B (in Band 8), and [O I] 145 μm for HerBS-41A (in Band 7). The [N II] emission line is detected in both HerBS-170 and HerBS-184. In the case of HerBS-81, only part of the [N II] emission line was covered ($V > 50$ km s^{-1}) and hence not detected in the current data. The [O I] emission line was detected in HerBS-41A, although we note that the total flux estimate might be underestimated since we probe only the $\Delta V < 150$ km s^{-1} region.

Fig. 10 shows the observed [O I] and [N II] line luminosity scaling relations of the three detected ANGELS sources, compared to local (Brauher et al. 2008) and distant galaxies (Herrera-Camus et al. 2018; Cheng et al. 2020; Cunningham et al. 2020) from other surveys. We note that we do not scale our luminosity for the magnification of HerBS-41A, since we do not have lensing models of our spectral line. Our sources lie on the bright end of the scaling relations, and HerBS-170 qualifies as the brightest nitrogen emitter observed to date. There is no evidence for a far-infrared line deficit, which appears to affect high star formation surface-density galaxies (e.g. Rybak et al. 2019). As we build catalogues of atomic lines, these lines become invaluable to provide strong constraints of the gas densities (e.g. Doherty et al. 2020), ionization parameters (Hagimoto et al. 2023), and metallicities (e.g. Tadaki et al. 2022) to characterize this diverse sample of DSFGs.

5.4 Stacked spectrum

In an effort to reveal fainter line transitions, line stacking experiments combine the emission from multiple galaxies together for a higher fidelity signal (Spilker et al. 2014; Fudamoto et al. 2017; Birkin et al. 2021; Chen et al. 2022; Hagimoto et al. 2023; Reuter et al. 2023). These fainter lines can reveal unique phases of the ISM. For example, hydrogen cyanide traces dense, star-forming gas (Riechers et al. 2006, 2010; Oteo et al. 2017; Béthermin et al. 2018; Cañameras et al. 2021; Rybak et al. 2022; Yang et al. 2023), and the presence of carbon and oxygen isotopologues are a measure of metal enrichment history (Henkel et al. 2010; Béthermin et al. 2018; Zhang et al. 2018; Maiolino & Mannucci 2019). These lines are often faint and thus require long observation times. The observations of multiple sources can be combined through stacking, although these often are done only at the wavelengths where spectral scans searched for the redshifts, i.e. the 3 and 2 mm observed wavelengths. Consequently, faint lines in the 1 mm regime remain poorly studied, even though many molecular species exist in this wavelength range. Consequently, even if individual observations are not able to directly detect individual lines, stacking is thus an important tool, particularly when samples become large enough to enable A/B comparison tests.

Fig. 11 shows the stacked spectrum from the ANGELS observations using the same method as Hagimoto et al. (2023). In short, we extract the complete spectra from the regions where the Band 7 emission exceeds 2σ surrounding the sources using an additional smoothing of one beam. We decide to stack the spectrum of each galaxy with the goal of representing a single archetypal galaxy at $z = 2.5$ (approximately the mean of this sample; Urquhart et al. 2022) with an infrared luminosity of 10^{13} L$_\odot$. This involves normalizing all spectra to the same luminosity and to a common redshift. Consequently, we require a constant L' across all redshifts, and normalize the spectrum accordingly:

$$S_{\nu,\mathrm{common}} = S_\nu \left(\frac{D_\mathrm{L}(z_\mathrm{source})}{D_\mathrm{L}(z_\mathrm{common})}\right)^2 \frac{1+z_\mathrm{common}}{1+z_\mathrm{source}}, \quad (5)$$

where D_L refers to the luminosity distance at redshift z, and z_common is set to 2.5. This factor accounts for the cosmological dimming for each spectral line, as well as for the redshift-dependence of the flux density unit.

We use the *Herschel*-based infrared luminosities as discussed in Section 3.1, where we reweight the fields by their respective Band 7 fluxes (Bendo et al., in preparation; see Table D1), since the sources are most reliably detected at this frequency. When compared to the method in Hagimoto et al. (2023), where the weighting was performed based on the infrared luminosities derived from the ALMA Band 4 continuum, there appears to be a marginal (< 15 per cent) effect from source to source when compared to a fixed constant dust temperature. Each of the weighted spectra are then added by their variance-weighted fluxes, which prioritizes the highest SNRs of the lines. As discussed in detail by Hagimoto et al. (2023) and Reuter et al. (2023), this means that the brightest sources are still predominantly determining the spectrum. It explains the lack of effect in line SNR when changing the (intrinsic) luminosity or dust-mass weightings as shown in Spilker et al. (2014). However, the relative line ratios within the composite spectrum do strongly

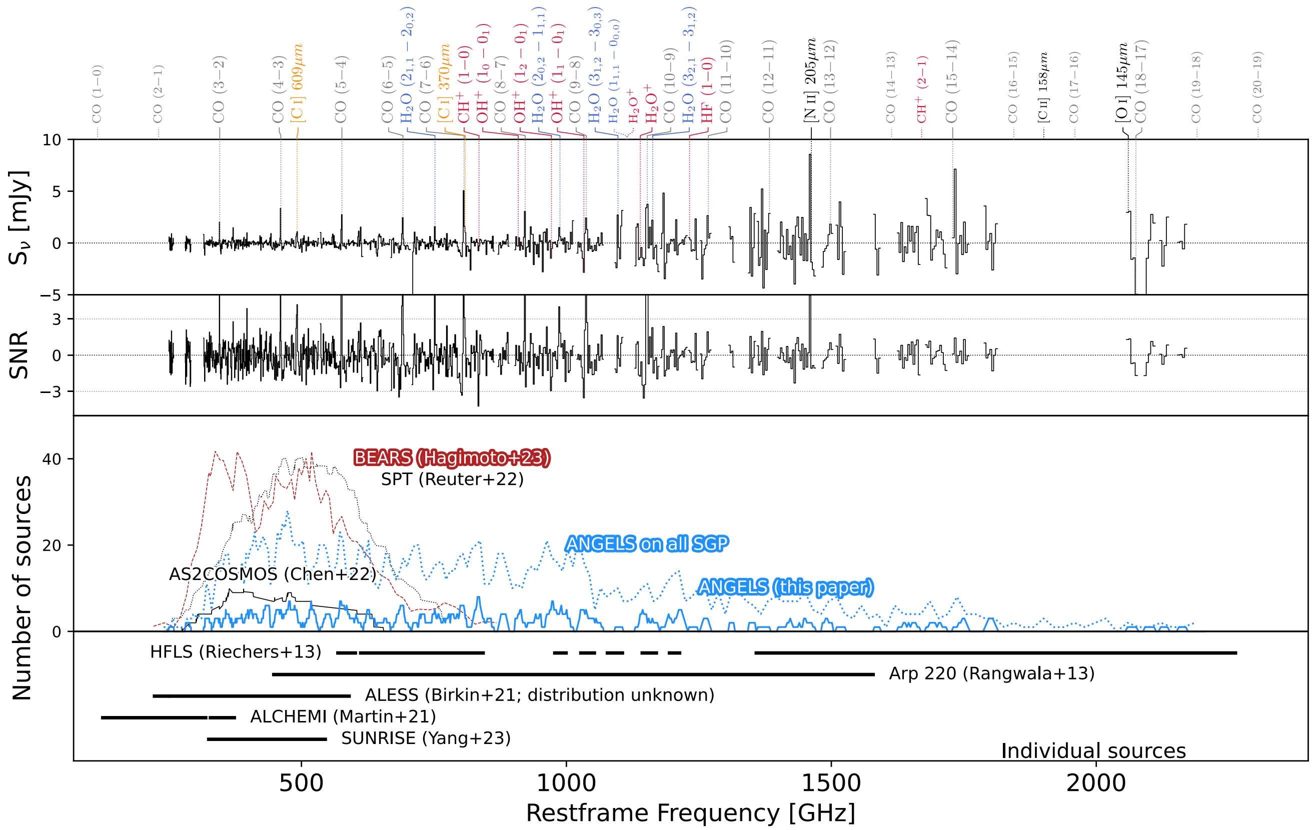

Figure 11. The composite spectrum based on the ANGELS observations. The top panel shows the noise-weighted stacked spectrum of an archetypal $z = 2.5$ and $L_{\rm IR} = 10^{13}\,{\rm L}_{\odot}$ galaxy. The brightest spectral line is the [N II] line at around 10 mJy (see Section 5.4). The middle panel shows the SNR of the spectrum. The bottom panel shows the number of sources that contribute to each of the spectral line in a solid blue line. Similar stacking experiments (Reuter et al. 2020; Chen et al. 2022; Hagimoto et al. 2023) are shown as histograms, and the predicted coverage of the full SGP sample is shown in a blue dashed line. Follow-up studies of individual sources (Rangwala et al. 2014; Riechers et al. 2013; Birkin et al. 2021; Martín et al. 2021; Yang et al. 2023) are shown as solid lines. While the coverage of the ANGELS sources in this paper becomes sparse at higher frequency, the full survey aims to detect at least a few sources out to 2300 GHz.

vary as different weighting schemes are used (see e.g. the discussion in Reuter et al. 2023), and are important to account for in future composite spectra.

The top panel of Fig. 11 shows the rest-frame composite spectrum using the above-mentioned weighting scheme. The middle panel shows the SNR of the observations, while the lowest panel shows the total number of spectral lines seen per rest-frame frequency, and compares it to other and future stacking experiments.

All CO lines with $J_{\rm up} < 11$ are seen in the stacked spectrum. Only two out of five of the [C I](1−0) lines are detected individually, but the [C I](1−0) line is clearly detected in the stacked emission. The line profile of [C I](1−0) appears broader, and could remain undetected because of its potentially more extended nature (Valentino et al. 2020b). Both H_2O ($2_{1,1}-2_{0,2}$) and ($2_{0,2}-1_{1,1}$) are detected in the stacked spectrum, in line with the individual detections and previous stacking experiments (Yang et al. 2016; Zavala et al. 2018; Hagimoto et al. 2023; Reuter et al. 2023). The brightest stacked spectral line, [N II], is detected, and stands out in the stacked spectrum. Three molecular absorption lines are seen at the -3σ level, CH^+(1−0), OH^+ (1_1-0_1), and (1_2-0_1), which are also seen in individual observations, while the fainter OH^+ feature (1_0-0_1) remains undetected. Importantly, the velocity difference relative to the systemic redshift of absorption lines are large. Detecting such features in a line stack is thus surprising. In future observations, larger samples will be able to more fully characterize fainter lines, and combine the resolved (ANGELS) and unresolved (BEARS) data to better characterize the 200–800 GHz regime, while short-wavelength observations fill in a contiguous composite spectrum well into the THz regime, probing atomic lines such as [C II] 158 μm and [O III] 88 μm, as well as provide a composite CO SLED out to high-J transitions as explored in previous work (Hagimoto et al. 2023; Reuter et al. 2023).

6 RESOLVED PROPERTIES OF ANGELS SOURCES

The ANGELS observations have provided a high-resolution view on a sample of sixteen *Herschel* fields, revealing 54 emission and 12 absorption lines, while providing meaningful upper limits on another 27 lines. The beam sizes of the observations range between 0.5 to 0.1 arcsec, enough to resolve the internal structure of these distant sources. In the following, we will use this resolved data to investigate the properties of the star formation in the ANGELS sources.

6.1 The resolved star formation law in ANGELS sources

The Schmidt–Kennicutt relation between the star formation surface density and molecular gas mass surface density ($\Sigma_{\rm SFR}$–$\Sigma_{\rm H_2}$; Schmidt 1959; Kennicutt 1998) is a diagnostic of the star formation mode. High-redshift dusty starbursts typically have higher SFRs relative to

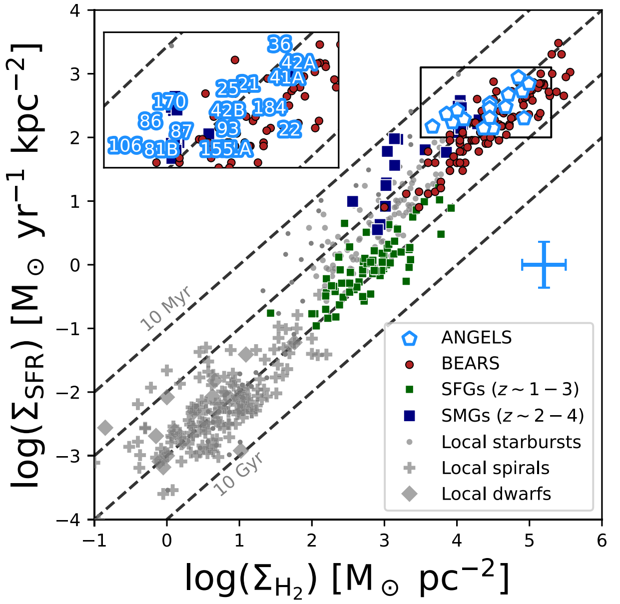

Figure 12. The resolved Schmidt–Kennicutt star formation law of the ANGELS sources with observations of CO emission lines. We compare the sources against reference samples of low-redshift galaxies (Kennicutt 1989; de los Reyes & Kennicutt 2019a, b; Kennicutt & De Los Reyes 2021; grey points, plus points, and diamonds), high-redshift star-forming galaxies (Tacconi et al. 2013; green squares), and high-redshift DSFGs (Hatsukade et al. 2015; Chen et al. 2017 and references therein; blue squares). The parent sample of BEARS is shown in dark red circles (Hagimoto et al. 2023). We use an $\alpha_{[CI]}$ value of 17.0 and an α_{CO} value of 4.0 from the recent study of Dunne et al. (2021, 2022). We adjust the reference sample of DSFGs (blue squares) from Chen et al. (2017) from the initially assumed $\alpha_{CO} = 0.8$ to 4.0 for a fair comparison. These sources lie in the upper right region of the star formation law, with similar depletion times as the resolved observations of unlensed sources (Chen et al. 2017). The sources have similar or slightly smaller volumes of star-forming gas than unresolved studies with similar surface SFRs. This could indicate that the dense star-forming regions deplete faster than the moderately resolved studies, and require efficient fuelling from more gas-rich regions to maintain their high surface SFRs.

their molecular gas compared to normal star-forming galaxies (e.g. Casey et al. 2014), which results in a shorter depletion time-scale ($\sim$ 100 Myr). The reasons for this boost in star formation are often hypothesized to be connected with recent merger events (Sanders et al. 1988; Barnes & Hernquist 1991; Hopkins et al. 2008), although several other theories have been posited, including secular evolution and violent disc collapse (Cai et al. 2013; Gullberg et al. 2019; Hodge et al. 2019; Rizzo et al. 2020; Fraternali et al. 2021; Zavala et al. 2022).

Fig. 12 shows the resolved Schmidt–Kennicutt relation (Schmidt 1959; Kennicutt 1998) for the ANGELS sources and reference samples of low-redshift galaxies (Kennicutt 1989; de los Reyes & Kennicutt 2019a, b; Kennicutt & De Los Reyes 2021), high-redshift star-forming galaxies (Tacconi et al. 2013), and high-redshift DSFGs (Hatsukade et al. 2015; Chen et al. 2017, and references therein). The parent sample of BEARS is shown in dark red circles (Hagimoto et al. 2023). These modestly resolved observations show more extreme star-forming environments in the mixed lensed and unlensed samples than found for unlensed DSFGs. We use a CO–H_2 conversion factor (α_{CO}) value of 4.0 from the recent study of Dunne et al. (2021, 2022), adjusting the reference sample of DSFGs accordingly for a fair comparison, although we note that this molecular gas conversion can vary sharply from source to source (Harrington et al. 2021). Similarly, we use an IR luminosity-to-SFR factor of 1.73×10^{-10} $M_\odot yr^{-1}$ ($L_\odot^{-1}$) valid for a Salpeter 1–100 $M_\odot$ initial mass function. We calculate the position of each galaxy using a pixel-by-pixel comparison between the dust continuum emission from Band 7 to the lowest J ANGELS-observed CO transition. Since pixels within each beam are not statistically independent, we subsequently downsample to account for this effect.

The higher resolution Band 7 dust continuum is smoothed to the same beam size as the Bands 3, 4, or 5 CO emission using the images as they appear in the sky. Then, we compare the maps on a pixel-by-pixel basis to provide a distribution of the sources, and while the selection itself could be affected by differential lensing, the position of these sources on the star formation law should not be affected by the lensing as surface brightness is preserved during a lensing event. We use pixels with either the moment-0 CO or dust emission beyond 3σ within a radius including all of the source flux, as shown in the appendix figures. As a lower limit, we demand that the pixel in the other image has at least 1σ emission, and ensure that the majority ($>$ 80 per cent) of pixels are not excluded from this additional constraint. We show these pixel-per-pixel comparison of the star formation law in Appendix Figs G1 and G2 to investigate the individual properties of the sources, and for all sources where available, compare directly to the CO and [C I]-derived star formation and gas surface densities from the moderately resolved study in Hagimoto et al. (2023). These show a relatively wide distribution of star formation or gas surface densities, varying by up to an order of magnitude as seen in previous studies as well (Ikeda et al. 2022). Note that the sharp lines in resolved Schmidt–Kennicutt relations in Fig. G2, particularly for HerBS-25 and -106, come from the $> 1\sigma$ criterion. Deeper observations of these sources could reveal lower SFR and gas mass surface densities on the source outskirts. This could shift their average position on the star formation diagram downwards by up to $\sim$ 0.2 dex based on the current distribution of the $> 1\sigma$ emission shown in Fig. G2. This further demonstrates the internal variation of the star formation law within galaxies, and the need for efficient fuelling of gas within galaxies to sustain these high SFRs for durations in excess of 100 Myr.

The difference between the moderately resolved study (Hagimoto et al. 2023) and the ANGELS observations mostly lie along the constant depletion times (i.e. the diagonal lines). This indicates that the discrepancy between these studies could originate from less accurate, and dependent size estimations. Additionally, CO line tracers between CO(3−2) and CO(6−5) are used for the molecular gas mass estimates, which add additional uncertainties in the conversion to the ground state, i.e. to the luminosity of CO(1−0). This can explain the additional offset in the x-direction (Σ_{H_2}) for HerBS-86 and -106, where CO(6–5) was the lowest-J transition. Reassuringly, there do not appear to be significant y-axis offsets, indicating that the SFR estimates are in agreement (both this study and Hagimoto et al. 2023 use ALMA dust continuum measurements).

The distribution of the sources is similar to the moderately resolved pilot sample of BEARS (red points), with larger gas and SFR surface densities than those found by previous observations for unlensed sources (Chen et al. 2017). There appears to be enough gas available for around 100 megayears or one gigayear of star formation in these sources. The extended gas reservoirs seen in even these short snapshots thus indicate that the spatial distribution of gas and dust can play an important role in the evolution of DSFGs (see e.g. Ikeda et al. 2022). The order of magnitude spread in the pixel-per-pixel surface gas densities and surface SFRs indicates that DSFGs require efficient feeding of gas from the gas-rich regions into star-forming regions to

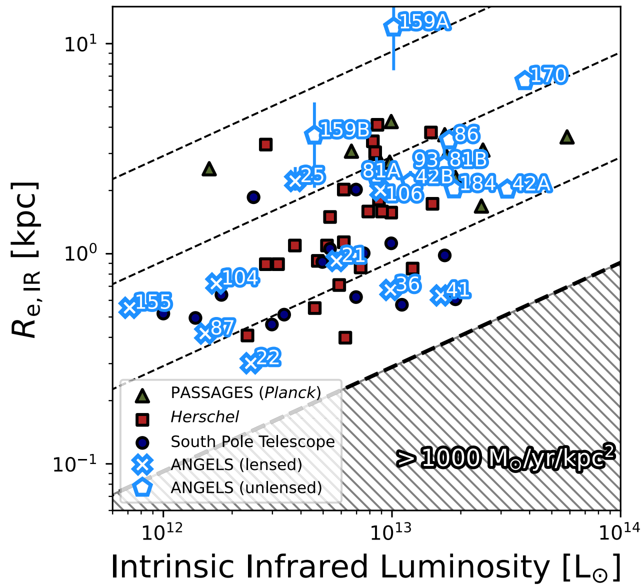

Figure 13. The radius of the sources in proper angular distance as a function of their luminosity for the ANGELS sources and other distant galaxies (Bussmann et al. 2013; Spilker et al. 2016; Kamieneski et al. 2024). We use the intrinsic sizes for all lensed sources (see Table 3). The hatched region indicates the forbidden regime for a stable star-forming system according to Andrews & Thompson (2011), with increasing diagonal dashed lines indicating star formation surface densities of 1000, 100, 10, and 1 $M_\odot$ yr^{-1} kpc^{-2}. The majority of the sources lie around 100 $M_\odot$ yr^{-1} kpc^{-2}, with the surface SFRs of HerBS-22, -41A, and -36 approaching the limits of star formation. The diffuse sources (see Section 7.3) HerBS-159A and -B appear to be more extended with low SFR densities on the order of ≈ 10 $M_\odot$ yr^{-1} kpc^{-2}.

ensure that the high SFRs can be sustained for the depletion time-scales indicated by un- or marginally-resolved observations (e.g. Hagimoto et al. 2023).

6.2 Star formation surface densities of ANGELS sources

When many stars are formed in a small environment, star formation feedback becomes a more important contributor of the evolution of galaxies. Fig. 13 compares the intrinsic sizes of the ANGELS sources against their intrinsic infrared luminosities. By comparing their star formation surface densities to other galaxies (Bothwell et al. 2013; Spilker et al. 2016; Kamieneski et al. 2024) and to expected limits of SFR (Andrews & Thompson 2011), we find a large variation across our sample of sources. We use the Sérsic profiles for the sources when available from the lensing reconstruction (seen by crosses; Table 3), where the Sérsic indices are free to vary between 0.5 and 5. The non-lensed sources are fitted using the CASA task IMFIT, which assumes a Sérsic index of 0.5 that appears to match the emission profiles well based on the residual images. These unlensed sources are broadly larger in size (shown in pentagons instead of crosses). We calculate the per-source luminosity using the *Herschel* photometry, which better accounts for the total SFR in the total system, but could cause discrepancies between the $\Sigma_{\rm SFR}$ estimates from the resolved star formation law and this discussion (see Section 3.1). In the case of any multiplicity, we distribute the flux based on the weighted flux densities of the Band 7 continuum emission.

The bulk of sources reside between the 10 and 100 $M_\odot$ yr^{-1} kpc^{-2} regime, similar to other sources seen with *Herschel* and SPT. Broadly, three sources are close to the forbidden regime of star formation, of which two are in the hyperluminous infrared galaxy (HyLIRG) regime. Although likely the bulk of the submm emission of these sources is due to star-= formation (Bakx et al. 2018), an obscured AGN could be contributing to the emission and produce these compact-but-bright sources. In total, eight sources are in the $L_{\rm IR} > 10^{13}$ $L_\odot$ regime. The more diffuse galaxies, HerBS-159A and B (see Section 7.3) lie in the < 10 $M_\odot$ yr^{-1} kpc^{-2} regime, where typically more normal star-forming galaxies are found (e.g. Tacconi et al. 2013). Note that the radius of these sources is extracted on a tapered image (*uv*-taper of 0.5 arcsec), resulting in larger errors, but regardless their radii are larger than average. The diverse and complex nature of ANGELS sources is apparent from these resolved ALMA observations. In the subsequent section, we compare these rich results against the known literature of DSFGs.

7 NATURE OF ANGELS SOURCES

The ANGELS sources are effectively randomly sampled from the BEARS survey, with a selection based solely by their proximity to each other on scales beyond the scales of the cosmic web (see Fig. 1), as is discussed further in Negrello et al. (2017). The guiding principle behind the observations was solely to maximize the number of lines that we could target within a single tuning modulo the atmosphere. As a result, these observations provide an unbiased sampling of the properties of high-redshift, bright *Herschel* sources. In this section, we investigate the properties of ANGELS sources in an effort to better characterize the bright end of *Herschel* sources.

7.1 Lensing among the HerBS sources

The total sample of 16 *Herschel* sources turned out to consist of 26 separate ALMA sources. Out of these, nine ALMA sources are apparent lenses from the observations. Although an additional number of sources might still be lensed (HerBS-42A and -159A), we exclude these in the statistics of these sources. The lensing fraction of 56 ± 13 per cent (assuming a binomial distribution; Gehrels 1986) is on the lower end of theoretical predictions (e.g. 70 per cent; Negrello et al. 2007), with direct comparisons to galaxy evolution models (Cai et al. 2013; Bakx et al. 2018, 2020b) expected even higher fractions ($\sim$ 85 per cent), in line with subsequent comparisons to near-infrared imaging ($\sim$ 82 per cent; Bakx, Eales & Amvrosiadis 2020a). Lensed galaxies allow the probing of populations that would remain under the detection capabilities of facilities, with magnifications up to several tens (Dye et al. 2015, 2018; Spilker et al. 2016; Amvrosiadis et al. 2018; Zavala et al. 2018; Rizzo et al. 2020; Kamieneski et al. 2024). The properties of these sources appears diverse, with over two order of magnitudes spread in the source radius and associated star formation surface density (Fig. 13). The comparison samples between the lensed and unlensed ANGELS sources are selected from different areas and depths. As a result, larger scale surveys will select towards more rare geometries of lensing where strongly boosting caustics intersect with bright central regions resulting in brighter fluxes. Four of the sources in ANGELS are also present in the sample from Negrello et al. (2017), namely HerBS-21, 22, 25, and 42A/B. Two sources (HerBS-36 and 41A) also meet the Negrello et al. (2017) selection criterion of $S_{500} > 100$ mJy, and are also lensed. All four common sources have lensing rank C (unclear lensing nature). HerBS-42-A/B is a double system and the individual S_{500} fluxes fall below the 100 mJy criterion, confirming the prediction by Negrello et al. (2007) that most of the $S_{500} > 100$ mJy sources – also those with C rank – are likely strongly lensed.

The *HerBS* sample is selected at the transition from mostly lensed surveys (Harrington et al. 2016; Spilker et al. 2016; Negrello et al. 2017) to unlensed systems found often in ground-based surveys such as LABOCA (LArge APEX BOlometer CAmera; e.g. Weiß et al. 2009) and Submillimetre Common-User Bolometer Array (-2) (e.g. Simpson et al. 2019; Garratt et al. 2023). Among the lensed sources, differential lensing[5] (Serjeant 2012, 2024) could more strongly affect the lensed samples, resulting in a more biased and inhomogeneous survey at the higher magnifications. Meanwhile, the lensing magnifications of our survey ($\mu = 2 - 28$ with a median $\mu = 8.9$) are surprisingly similar to those seen of the SPT ($\mu = 2 - 33$ with a median $\mu = 6.3$; Spilker et al. 2016; Reuter et al. 2020) and *Planck* ($\mu = 2 - 28$ with a median $\mu = 7$; Kamieneski et al. 2024), and the effect of bias could be similar across our samples. We find that the majority of these lensed systems are small (0.3–3 kpc) central dusty systems, similar to the sources found in ALESS (ALMA LABOCA ECDFS Submm Survey; Hodge et al. 2013; Karim et al. 2013). The line profiles of these galaxies do not appear to indicate any source multiplicity or merging state contrary to the idea that all DSFGs are mergers as often seen in the local Universe (Sanders et al. 1988; Barnes & Hernquist 1991; Hopkins et al. 2008). Instead, central dusty starbursts could be driving the bulk of the lensed sources seen in *Herschel* and other surveys (Barro et al. 2016; Hodge et al. 2016; Cibinel et al. 2017; Ikarashi et al. 2017; Tadaki et al. 2017; Gullberg et al. 2019; Pantoni et al. 2021), where galaxies are building up a compact central dense stellar component and change their morphology from disc- to bulge-dominated systems, perhaps in late-stage mergers and/or violent disc instabilities (Zolotov et al. 2015). This could be a bias due to the lensing selection – where compact sources are more susceptible to be strongly lensed, either because of their prevalence or their high star formation surface densities, than extended merging systems – or an effect of differential lensing. Only deep observations tracing the more extended emission in the lower magnification regions would be able to differentiate between these two scenarios.

7.2 Hyperluminous galaxies

The high-resolution observations revealed the lensing properties of the ANGELS sources. Eleven sources remain above the HyLIRG ($> 10^{13} L_{\rm IR}$ in Fig. 13) regime, although HerBS-159A is potentially lensed. This is higher than typically observed in other samples (cf. Reuter et al. 2020; Liao et al. 2024), likely because of the fainter selection of the *HerBS* sources relative to other surveys. Unlike the lensed sources (sizes between $300 - 2000$ pc with a median size of 600 pc), unlensed systems appear to be more extended (0.3–3 kpc), such as HerBS-93, -170, and -184. The extended morphology of HerBS-170 further makes its *HST*-dark nature surprising, as it requires a large, homogeneous dust screen to obscure this emission. Source confusion affects many of the apparently brightest *Herschel* galaxies (Bendo et al. 2023), however several of the intrinsically brightest sources also come from fields with multiples, such as HerBS-41A, -42A, and -81A. This means that source confusion only little affects the ability of *Herschel* to find HyLIRGs in the slightly fainter flux regimes ($S_{500} = 50 - 100$ mJy; Ivison et al. 2016; Oteo et al. 2017).

[5]Due to sharp variations in the lensing magnification of different regions of a galaxy, the observed, lensed line, and continuum fluxes of galaxies could give a warped perspective on the intrinsic properties of galaxies. This effect is exacerbated by the initial selection effects, which might favour the selection of galaxies with strong amplifications of star-forming regions.

Four sources showcase the extreme end of star formation in this sample: HerBS-36, -41A, -42A, and -81A. Their CO SLEDs indicate similar star-forming conditions as found in other intense star-forming systems, such as *Planck*-selected systems. The surprising discovery of inflowing gas seen in a shocked tracer for HerBS-36 could further suggest that inflows play an important role in boosting SFRs (Berta et al. 2021), with part of the source close to the limits of star formation (Andrews & Thompson 2011), which can thus provide a ready source for shocks.

The morphology of these systems furthermore appears clumpy, with modest amounts of the flux density ($\approx$ 10 per cent $-$ 20 per cent for HerBS-93, -170, and -184) and thus associated star formation originating from these clumps. Such structures could be essential for the formation of bulges and of wider star formation across these intense starbursts (Hodge et al. 2019; Rujopakarn et al. 2019; Gullberg et al. 2019). Contrary to this, observations of lensed ULIRGs (Dye et al. 2018; Rizzo et al. 2020) often find more stable rotators, although SDP.81 is an obvious counter example (Dye et al. 2015; Rybak et al. 2015; Tamura et al. 2015). An important consideration here is also that lensing could affect our picture of the clumpiness of these sources, both through differential lensing and uv-plane issues addressed in Gullberg et al. (2019). HerBS-41A and -93 show velocity widths of approximately 1000 km s^{-1}, which indicates that they are already very massive systems ($\sim 5 \times 10^{11}$M$_\odot$; Hagimoto et al. 2023) without obvious indications of merging. The discrepancy between smaller compact lensed ULIRGs and the larger weakly or unlensed clumpy HyLIRGs is an important avenue for future investigations, as we find five of our sources to show these extended clumpy morphologies, with an incidence rate of roughly 35 ± 25 per cent.

Particularly the lack of *Hubble* counterpart for HerBS-170 poses an interesting test for the clumpy morphology of dust. At a rest-frame wavelength of 2100 Å, these *Hubble* observations are sensitive to direct starlight. With a total SFR of $3000 - 7000$ M$_\odot$ yr^{-1} depending on the IMF, the dust screen needs to extend across the system to obscure both the small-scale clumps (a few 100 M$_\odot$ yr^{-1}) and the central star-forming region. HerBS-170 has roughly 4 orders of magnitude higher dust mass than the optically selected $z = 6 - 8$ REBELS sources (Reionization Era Bright Emission Line Survey; Ferrara et al. 2022), whose dust screen size extends about 30 times further ($\sim$ 1000 times in terms of area). Using equation (11) from Ferrara et al. (2022), the optical depth of HerBS-170 is thus roughly 10 times higher than REBELS with $A_V = 0.1 - 0.4$ (Inami et al. 2022). Meanwhile, the REBELS observations are only moderately deeper ($1\sigma_{1500} = 0.06\mu$Jy and $1\sigma_{2100} = 0.1\,\mu$Jy, respectively), although REBELS lie at higher redshifts. The rest-frame optical dust obscuration of HerBS-170 is thus, as expected, much higher than optically selected sources, but perhaps more importantly, the distribution of this dust must be coincident with star formation across the entire extended system, suggestive of a remarkably-homogeneous dust screen or of star formation occurring in separate but similarly obscured clumps across the system at 10 kpc separation (see e.g. Cochrane et al. 2021).

While the dust properties in DSFGs are quite similar (dust emissivity index, gas-to-dust ratio; Bendo et al. 2023; Hagimoto et al. 2023), the CO excitations and other line ratios suggest a diverse group (Daddi et al. 2015; Valentino et al. 2020a; Birkin et al. 2021; Hagimoto et al. 2023; Stanley et al. 2023), indicating that there are multiple ways to form a DSFG (Quirós-Rojas et al. 2024). The morphological and kinematic properties of these HyLIRGs seems to indicate a potential pathway where star-forming clumps are associated with gaseous discs that are unstable (Toomre $Q < 1$)

due to high turbulence (Krumholz, Dekel & McKee 2012; Harrington et al. 2021). This would be contrary to smaller central dusty starbursts that are rotationally dominated (Dekel et al. 2009) seen mostly through lenses (Dye et al. 2018; Rizzo et al. 2020) and ground-based surveys (Hodge et al. 2013; Karim et al. 2013). The diversity of models to explain DSFGs (Baugh et al. 2005; Davé et al. 2010; Narayanan et al. 2009, 2015) should thus accurately reflect the multiple pathways of starbursts and their transition to quenched galaxies (Toft et al. 2014; Barro et al. 2016).

7.3 Spatially extended sources

HerBS-159A and B are extended sources, which made the emission fall below the detection criteria of our observations. By tapering the data (see Section 3.1), we find $\sim 3\sigma - 5\sigma$ continuum emission visible across Bands 5, 6, 7, and 8 for these galaxies. This system is of particular interest, as HerBS-159B is one of the CUBS (Companion sources with Unusually Bright lineS) sources in Hagimoto et al. (2023). The CO SLED of this system is in excess of the maximum expected behaviour from the equipartition theorem between CO excitations; i.e. it is superthermalized, and cannot be explained by linear-scaling effects such as differential lensing (Serjeant 2024). Out of the total sample of 46 sources within the CO studies in Hagimoto et al. (2023), only four CUBS sources are found. If there is any intrinsic physical difference between these sources, their physical interpretation thus offers insight into a unique galaxy process within the DSFG phase, with an occurrence rate of ~ 8 per cent. Under the assumption of a single DSFG phase with a duration of ≈ 200 Myr (i.e. their average gas depletion time; Hagimoto et al. 2023), this could thus point to a galaxy phase duration of ~ 20 Myr.

It is still unclear how galaxies would achieve such a galaxy phase, however it is possible to physically provide an superthermalized CO SLED through optical depth effects (see the modelling in Hagimoto et al. 2023). These could be triggered by a merger phase or by the presence of an obscured AGN. Unfortunately, HerBS-159B does not have any observations of spectral emission lines within ANGELS that further provide constraints on the system properties.

Instead, the fact that the HerBS-159 system requires tapering to reveal the component galaxies is an important hint to their galaxy evolutionary phase. Similar galaxies have been reported in different studies. Tadaki et al. (2020) reported on such a galaxy with extended emission, missed in the untapered data, while looking at 85 massive galaxies with ALMA. Sun et al. (2021) investigated a sample of lensed sources with *Herschel* through ALMA observations. Two sources out of a sample of 29 have similar features to the HerBS-159 system. They report that these sources lack the central starbursts dominating the majority of galaxies, similar to the morphologies that are seen in the lensing reconstructions for our sources (Fig. 5). This is not in agreement with a bright central component associated with a far-infrared luminous AGN.

HST imaging revealed that HerBS-159A is likely a lensed system with extended emission across multiple arcseconds. Regardless, this means that the Einstein rings also carry a certain thickness, implying extended emission in the source plane. No obvious lensing morphology is seen for HerBS-159B (the CUBS source; Hagimoto et al. 2023), with no evidence of a nuclear emitting region. The fact that all CUBS sources were seen as multiples suggests this could be an important component to the formation of this phase. The early merging, pre-coalescence phase thus seems the most likely explanation for this phase. This early phase, also occurring on the scale of ~10 megayears. Rare fields such as HerBS-159 thus require detailed further study to find out how they fit within the emerging paradigm of DSFGs, and might reflect an important part in merging history still missing from models.

8 ANGELS AS A LINE SURVEY TECHNIQUE

The ANGELS pilot aimed to investigate the use of Bands 3–8 in-line observations through quick snapshots. In this section, we summarize the results of this method, and provide caveats and suggested improvements towards expansion of this survey to larger samples of bright sources.

8.1 ANGELS as a redshift machine!?

Three sources did not yet have spectroscopic redshifts at the start of the ANGELS observations: HerBS-87, -104, and -170 (see Table 1). The BEARS observations revealed single-line detections (Urquhart et al. 2022), but not at sufficient depth to exclude different redshift solutions (Bakx & Dannerbauer 2022). HerBS-87 had a single line detected at 160.96 GHz. HerBS-104 had a line detected at 90.91 GHz. The quality of the emission lines seen for HerBS-170 was below the significance to conclusively state the redshift, with lines at 111.15 and 156.13 GHz.

ANGELS observations revealed additional lines to ensure the robust redshifts of each of these three sources. Of course, these ANGELS tunings did not optimize towards lines for these three sources, but we use the method from Bakx & Dannerbauer (2022) to estimate the chance of a single line, or better yet, a robust redshift estimate from even blind observations, shown in Fig. 14. In total, we find a roughly 50 per cent chance to derive a robust redshift from six tunings (Bands 3–8) on a typical DSFG-like redshift distribution, and a > 75 per cent chance of detecting a single line for each source targeted. ANGELS thus offers a good chance of assisting in the redshift completion of the SGP fields. In this pilot study, 13 galaxies (+ three neighbouring galaxies) had spectroscopic redshifts, and the choice for observing windows was driven solely by the expected lines in our observing window for these 16 galaxies. However, in a scenario where much fewer spectroscopic redshifts are known, preference to lower frequency observations could be given when using tools similar to Appendix Fig. A1, as they relatively cover a larger redshift region for the same observing window.

8.2 Efficiency compared to overhead-limited surveys

ANGELS has offered a high-resolution view on galaxies across a wide spectroscopic scope using ALMA. The project was uniquely enabled by the bright nature of *Herschel* sources with yet high enough surface density to enable efficient scheduling (see Fig. 1). In total, 94 spectral lines were targeted across 28 different line transitions. On average, each source is observed in five transitions, with HerBS-41A being targeted in as many as 12 lines. 66 lines were detected, resulting in a detection ratio of 70 per cent. In Bands 3 and 4, eleven transitions were targeted, and, respectively, 8 and 9 of these transitions were detected. Band 5 targeted 19 lines, and we detected 14. Most lines were targeted in Band 6, where out of 27 lines, 19 were detected. Band 7 had 17 lines targeted and 11 were detected, and Band 8 targeted 9 lines, with five lines detected.

At only 6.5 h of observing time, the ANGELS survey targeted one line every 4 min, and detected a line every 6 min. Since each band required around 1 h (and Band 8 required 1.5 h), the Band 6 tunings were most efficient, at one line detected every three minutes. This is faster than even efficient blind redshift surveys of submm bright sources such as BEARS, which detected around 150 spectral

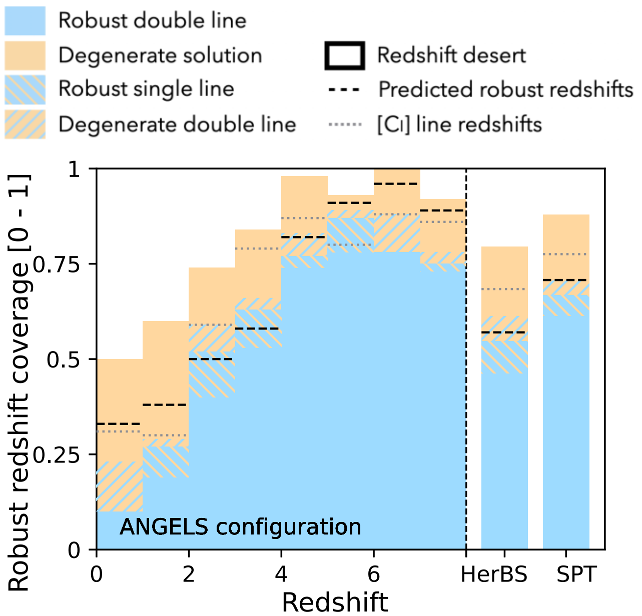

Figure 14. We use the method from Bakx & Dannerbauer (2022) to calculate the redshift efficiency of the ANGELS method across a blind sample of galaxies – without any prior line confirmations. These show a large probability for robust redshift identification for sources without known redshifts beyond $z > 2$ (darker blue regions). The HerBS (Bakx et al. 2018, 2020b) and SPT sources (Reuter et al. 2020; the two rightmost histograms) show the predicted capability to find robust and single-line (lighter orange region) redshifts for a sample with the same redshift distribution as the HerBS and SPT samples. The blue regions indicate the chance of finding more than one spectral line, while orange regions suggest a single spectral line will be found in a tuning. Hatched blue fill indicates cases where one can identify the redshift robustly with even a single spectral line, while hatched orange fill indicates the situation where redshift degeneracies remain down to a 5σ uncertainty in $z_{\rm phot}$. The grey dotted lines indicate the robust redshifts if we include the possibility of detecting atomic lines such as [C I], and the black dashed lines indicate the robust redshifts if we include the possibility of single-line robust redshifts and for cases where there still remains a degeneracy between multiple CO line solutions (see Bakx & Dannerbauer 2022, for details). The three sources with ANGELS-confirmed redshifts already had a single-line detection, and ANGELS thus offers a good chance of assisting in the redshift completion of the SGP fields.

lines across roughly 30 h of observation time (12 min per line). We note that this method also used the optimized observations of clusters of sources (see Fig. 1) to increase the efficiency. Similarly, the z-GAL NOEMA survey (Cox et al. 2023; Berta et al. 2023; Ismail et al. 2023) managed to detect 318 emission lines for 135 *Herschel*-selected galaxies, resulting in a detection rate of about one line every 30 min. As a rough estimate, every targeted observation requires between 20 and 30 min of overheads such as calibration steps, reducing even surveys of bright sources to an efficiency of one line per every 30 min. As such, clustering is an important tool for future spectral surveys, and the ANGELS method demonstrated here offers at the very least a doubling, but even an order of magnitude increase in the efficiency of line surveys with ALMA on bright targets.

8.3 Caveats with the ANGELS method

We note several short comings of this method, which could be used as caveats for future attempts to do efficient line surveys with ALMA. First, the ANGELS method is efficient, but does not provide the homogeneity of targeted observations with ALMA. In fact, these observations are not deep enough to guarantee a detection, and if these observations were set to guarantee a detection, the efficiency boost of ANGELS would reduce significantly. Detection bias can strongly influence the scientific consensus surrounding important topics, such as the gas depletion time or ionization state of galaxies (e.g. Bonato et al. 2014). Lines that remain below the detection limit could be teased out using line stacking. Here, we note an important caveat of line stacking, which reflects only the behaviour of a group of galaxies (see the section below). Since DSFGs are found to be a diverse population, line stacking alone cannot reveal more than population-wide behaviour, although once large-enough samples of data are explored, AB tests (i.e. comparing one subsample directly to another) in stacking might provide a solution to this problem.

Secondly, there exist a few more variables that can be optimized towards future ANGELS observations. The optimized tuning set-up for each cluster was determined on pre-defined clusters of galaxies. Sources on the edges of these clusters could switch between clusters, providing potentially more efficient or targeted observations to increase the total number of detected spectral lines. Meanwhile, the parametrization of the number of lines is based on a fixed set-up of spectral windows, which provide the widest bandwidth for all bBands except for Band 6. Band 6 has a variable intermediate frequency which has not been further optimized during these ANGELS observations, and would require higher order optimization steps to fully explore. The method for finding the tunings to detect as many lines as possible (Appendix Fig. A1) does not account for the chance to detect lines that were already observed in previous (BEARS) observations. The method also did not highlight that several sources, such as HerBS-159, did not have any detected spectral lines in their observations. Fig. A1 does account for an estimate of the atmospheric windows. However, it is hard to notice where the spectral lines exactly fall within these windows, and the effect of poor transparency is hard to properly take into account. Line species or even line types are clumped together, and as the sensitivity of receivers change with frequency, these graphs do not fully represent the difficulty of detecting specific species.

Lastly, although this has not turned out to be a major issue with our observations, these graphs do not account for the change in primary beam sensitivity with increasing frequency. As several of our sources were known multiples, we are unable to resolve some sources across all bands.

8.4 Future perspectives on complete *Herschel* samples

Fig. 1 offers an alluring peek on the potential of ANGELS on the complete sample of southern *Herschel* sources. The current observations target 16 sources in just 6.5 h. To cover the full 88 southern HerBS sources, we would require around 30 h. Scaling up the number of detected lines, we could expect to detect ~ 350 lines, exceeding even the most successful high-z large programmes with ALMA and NOEMA (e.g. Le Fèvre et al. 2020). On top of expanding the catalogues of high-J CO SLEDs, in- and outflowing lines, and atomic lines, a full-scale SGP survey would enable a comprehensive stacked spectrum into the Terahertz regime, a crucial next step until space-based missions such as the *Origins Space Telescope* (Meixner et al. 2019) take flight. The ability to characterize 88 sources, notwithstanding multiples (roughly an additional 30 per cent of sources) would enable sample comparisons on the order of 10 per cent, and could better test the claims made on this smaller sample of ANGELS pilot souces.

These pilot observations use the ALMA Bands with relatively good atmospheric transmission. Observations in Bands 9 and 10 would be technically difficult because of the atmospheric transmissivity, but would also offer a unique view on the short-wavelength dust continuum and on bright atomic lines, which are important diagnostics of the ISM (e.g. [O I], [O III], [C II], [N II], and [N III]; Ramos Padilla et al. 2023). The initial *Herschel* observations are to a greater or lesser extent affected by source confusion (Bendo et al. 2023), and a per-band view on these (and all southern) ANGELS sources would reveal the dust temperature in a pixel-by-pixel fashion, find any internal properties such as strong nuclear emission (Tsukui et al. 2023), and provide a solid foundation to study the complete dust emission of these dusty galaxies.

One of the main aims of ALMA development is the wide-band sensitivity upgrade (Carpenter et al. 2023). The goal of ALMA in 2030 is to double the receiver bandwidth, with a final goal of a quadrupling of the bandwidths. Here, we estimate the effect this would have on the efficiency of the ANGELS method beyond 2030. Appendix Fig. A1 is the tool used to derive the optimum tunings. As a mathematical abstraction, this graph depicts a convolution of the available lines (i.e. a set of delta functions at their redshifted, observed wavelengths) with the observable bandwidths across Bands 3 through 8. These graphs would look like flat lines for both extremes in bandwidths; a limitless spectral coverage would not require (or allow) optimization, while a very narrow spectral windows would quickly reduce the probability of finding lines across multiple sources in a single set-up. The current set-up sees at least a few lines per band, so as the bandwidths increase from their current state, the peak values would increase. However, the troughs would increase faster still, reducing the relative effect of optimization (i.e. the difference between the best and worst tuning set-ups).

This does not mean that the ANGELS method becomes redundant. First, these pilot observations were not deep enough to detect all targeted lines, particularly across the fainter sources. By increasing the integration time of our short snapshots to even a modest 5 min per source, the number of sources in a cluster identified by the ALMA Observing Tool would reduce rapidly (i.e. within 10 deg on the sky). This would leave fewer lines per selected set-up, again increasing the importance of optimization. Secondly, this pilot aims to target as many lines as possible. More science-case guided observations (instead of proof-of-principle) might want to target only specific line transitions such as CO(1−0), atomic lines or [C I]. With an increasing bandwidth, it becomes easier to design experiments that are able to widely target specific lines while also increasing the serendipity of the observations. Instead of designing the observations to place the targeted spectral line in the middle of the wider bandwidth, the ALMA tool should consider the possibility to pick up lines from multiple sources without the need for changing the local oscillator and the subsequent recalibration. Another such use-case might overcome the current limit on the resolution. The ANGELS strategy does not work with the ALMA configurations with a baseline greater than 3 km (C43-7 and beyond), which require sources to be within 1 deg-on the sky instead of 10. Although several sources are on the sky closer than this (particularly in lower flux selections), this would make the current version of the ANGELS method difficult to execute on a large sample. Finally, these observations provide a showcase towards the careful inspection of the data cubes of observations without the explicit goal to detect lines. As ALMA approaches ultrawide data cubes, careful exploration of ancillary lines in the spectra becomes more important, in particular when tools such as machine learning become better able to assist in the full exploitation of ALMA data (Guglielmetti et al. 2023).

9 CONCLUSIONS

The ANGELS observations have efficiently shared calibrators to facilitate a spectral survey of 16 sources in just 6.5 hours of observation time. These observations revealed

(i) ALMA targeted 94 lines and detected 66 of these lines. The majority (54) were seen in emission, with an additional 12 lines seen in absorption;

(ii) the dust continuum observations across six bands revealed the intrinsic nature of the sample, and for two diffuse sources, tapering was required to image them at $> 5\sigma$ significance. Of the 26 targets that have been observed, 21 sources have spectroscopic redshifts that enabled detailed studies of their emission and absorption lines;

(iii) the CO SLEDs show a variation of sources, with extreme SLEDs shown for a small fraction (36 per cent) of sources, which suggests a fraction of DSFGs are dominated by dense and warm gas;

(iv) the observations of 12 absorption line features show one rare case of inflowing gas through a redshifted molecular absorption lines, and two cases of strongly outflowing gas through blueshifted emission. The sources that are seen in multiple molecular absorption lines have similar systematic velocity offsets, suggesting that the absorption features are sensitive to similar regions of the circumgalactic and internal gas;

(v) atomic lines have been detected in three sources, namely: the [O I] 145 μm emission line in HerBS-41A, and the [N II] 205 μm emission line seen in HerBS-170 and HerBS-184, with HerBS-170 being the strongest [N II] emitter found to date;

(vi) a stacked spectrum offers a preliminary view on the capabilities of a large sample, which will be able to characterize DSFGs out to ≈ 2000 GHz; and

(vii) a preliminary bimodal picture of DSFGs is appearing, where lensed sources are indicative of typically central dusty starbursts, found in other surveys to be rotationally stable, while the weakly or unlensed HyLIRGs could represent turbulent massive star-forming events driven by unstable galaxy kinematics and clumpy gas flows.

Exploitation of the complete southern *Herschel* bright sources samples could enable a large line survey of ∼350 molecular and atomic lines, providing robust statistics with a fidelity of ∼10 per cent. This increase in fidelity will help characterize the diversity of DSFGs at cosmic noon, in order to investigate the origins of the most violent star-forming events in the Universe. Similarly, studies with short-wavelengths will enable a complete characterization of the dust, target short-wavelength emission lines, and allow for a more accurate separation of the unresolved *Herschel* fluxes. With the advent of the WSU (Carpenter et al. 2023), this method will become even more efficient – and arguably important to include in most observations – as the bandwidths of ALMA receivers and capabilities of the correlators increase in the near future.

ACKNOWLEDGEMENTS

The authors kindly thank the anonymous referee for their insightful comments and suggestions to improve this manuscript. Financial support from the Knut and Alice Wallenberg Foundation is gratefully acknowledged through grant no. KAW 2020.0081. This work was supported by NAOJ ALMA Scientific Research grant nos 2018-09B and JSPS KAKENHI nos 17H06130, 22H04939, 22J21948, and 22KJ1598. SS was partly supported by the ESCAPE project; ESCAPE – The European Science Cluster of Astronomy and Particle Physics ESFRI Research Infrastructures has received funding from the European Union's Horizon 2020 research and innovation programme under grant agreement no. 824064. SS also thanks the Science and Technology Facilities Council for financial support under grant ST/P000584/1. SU would like to thank the Open University School of Physical Sciences for supporting this work. This paper makes use of the following ALMA data: ADS/JAO.ALMA nos 2016.2.00133.S, 2018.1.00804.S, 2019.1.01477.S, and 2021.1.01628.S.

DATA AVAILABILITY

The data underlying this article will be shared on reasonable request to the corresponding author.

REFERENCES

Amvrosiadis A. et al., 2018, MNRAS, 475, 4939
Andrews B. H., Thompson T. A., 2011, ApJ, 727, 97
Aravena M. et al., 2016, MNRAS, 457, 4406
Asayama S. et al., 2014, PASJ, 66, 57
Bakx T., Conway J., 2024, preprint (arXiv:2409.02164)
Bakx T. J. L. C., Dannerbauer H., 2022, MNRAS, 515, 678
Bakx T. J. L. C. et al., 2018, MNRAS, 473, 1751
Bakx T. J. L. C., Eales S., Amvrosiadis A., 2020a, MNRAS, 493, 4276
Bakx T. J. L. C. et al., 2020b, MNRAS, 494, 10
Bakx T. J. L. C. et al., 2021, MNRAS, 508, L58
Bakx T. J. L. C. et al., 2023, MNRAS, 519, 5076
Bakx T. J. L. C., Gray B. S., González-Nuevo J., Bonavera L., Amvrosiadis A., Eales S., Hagimoto M., Serjeant S., 2024, MNRAS, 527, 8865
Barnes J. E., Hernquist L. E., 1991, ApJ, 370, L65
Barro G. et al., 2016, ApJ, 827, L32
Baugh C. M., Lacey C. G., Frenk C. S., Granato G. L., Silva L., Bressan A., Benson A. J., Cole S., 2005, MNRAS, 356, 1191
Belitsky V. et al., 2018, A&A, 611, A98
Bendo G. J. et al., 2023, MNRAS, 522, 2995
Berman D. A. et al., 2022, MNRAS, 515, 3911
Berta S. et al., 2021, A&A, 646, A122
Berta S. et al., 2023, A&A, 678, A28
Béthermin M. et al., 2018, A&A, 620, A115
Birkin J. E. et al., 2021, MNRAS, 501, 3926
Blain A. W., Smail I., Ivison R. J., Kneib J. P., Frayer D. T., 2002, Phys. Rep., 369, 111
Blain A. W., Chapman S. C., Smail I., Ivison R., 2004, ApJ, 611, 725
Bonato M. et al., 2014, MNRAS, 438, 2547
Borsato E. et al., 2023, MNRAS, 528, 6222
Bothwell M. S. et al., 2013, MNRAS, 429, 3047
Bouwens R. J. et al., 2022, ApJ, 931, 160
Brauher J. R., Dale D. A., Helou G., 2008, ApJS, 178, 280
Bryerton E., Saini K., Muehlberg J., Vaselaar D., Thacker D., 2013, in IEEE MTT-S International Microwave Symposium Digest (MTT). IEEE, p. 6697622
Bussmann R. S. et al., 2013, ApJ, 779, 25
Butler K. M. et al., 2021, ApJ, 919, 5
Butler K. M., van der Werf P. P., Topkaras T., Rybak M., Venemans B. P., Walter F., Decarli R., 2023, ApJ, 944, 134
Cai Z.-Y. et al., 2013, ApJ, 768, 21
Cañameras R. et al., 2018, A&A, 620, A61
Cañameras R. et al., 2021, A&A, 645, A45
Carilli C. L., Walter F., 2013, ARA&A, 51, 105
Carpenter J., Brogan C., Iono D., Mroczkowski T., 2023, in Ossenkopf-Okada V. et al., eds, Physics and Chemistry of Star Formation: The Dynamical ISM Across Time and Spatial Scales. Universitäts- und Stadtbibliothekj Köln, p. 304
CASA Team et al., 2022, PASP, 134, 114501
Casey C. M., 2016, ApJ, 824, 36
Casey C. M., Narayanan D., Cooray A., 2014, Phys. Rep., 541, 45
Cheng C. et al., 2020, ApJ, 898, 33
Chen C.-C. et al., 2017, ApJ, 846, 108
Chen C.-C. et al., 2022, ApJ, 929, 159
Chiang Y.-K., Overzier R., Gebhardt K., 2013, ApJ, 779, 127
Chiang Y.-K., Overzier R. A., Gebhardt K., Henriques B., 2017, ApJ, 844, L23
Cibinel A. et al., 2017, MNRAS, 469, 4683
Claude S. et al., 2008, in Duncan W. D., Holland W. S., Withington S., Zmuidzinas J., eds, Proc. SPIE Conf. Ser. Vol. 7020, Millimeter and Submillimeter Detectors and Instrumentation for Astronomy IV. SPIE, Bellingham, p. 70201B
Cochrane R. K. et al., 2021, MNRAS, 503, 2622
Cormier D. et al., 2015, A&A, 578, A53
Cortes P. C. et al., 2023, ALMA Cycle 10 Technical Handbook, ALMA Doc. 8.3. Joint ALMA Observatory, Vitacura, Santiago, Chile
Cox P. et al., 2023, A&A, 678, A26
Cunningham D. J. M. et al., 2020, MNRAS, 494, 4090
Czekala I. et al., 2021, ApJS, 257, 2
Daddi E. et al., 2015, A&A, 577, A46
Davé R., Finlator K., Oppenheimer B. D., Fardal M., Katz N., Kereš D., Weinberg D. H., 2010, MNRAS, 404, 1355
de los Reyes M. A. C., Kennicutt Robert C. J., 2019b, ApJ, 878, 74
de los Reyes M. A. C., Kennicutt Robert C. J., 2019a, ApJ, 872, 16
Dekel A. et al., 2009, Nature, 457, 451
Díaz-Santos T. et al., 2017, ApJ, 846, 32
Doherty M. J., Geach J. E., Ivison R. J., Dye S., 2020, ApJ, 905, 152
Dunne L., Maddox S. J., Vlahakis C., Gomez H. L., 2021, MNRAS, 501, 2573
Dunne L., Maddox S. J., Papadopoulos P. P., Ivison R. J., Gomez H. L., 2022, MNRAS, 517, 962
Dye S. et al., 2015, MNRAS, 452, 2258
Dye S. et al., 2018, MNRAS, 476, 4383
Eales S., Lilly S., Gear W., Dunne L., Bond J. R., Hammer F., Le Fèvre O., Crampton D., 1999, ApJ, 515, 518
Eales S. et al., 2010, PASP, 122, 499
Ediss G. A. et al., 2004, in Narayanan G., ed., Proc. Fifteenth Int. Symp. Space Terahertz Technology. p. 181
Enia A. et al., 2018, MNRAS, 475, 3467
Etherington A. et al., 2023, MNRAS, 521, 6005
Falgarone E. et al., 2017, Nature, 548, 430
Ferrara A. et al., 2022, MNRAS, 512, 58
Fixsen D. J., Bennett C. L., Mather J. C., 1999, ApJ, 526, 207
Fraternali F., Karim A., Magnelli B., Gómez-Guijarro C., Jiménez-Andrade E. F., Posses A. C., 2021, A&A, 647, A194
Fudamoto Y. et al., 2017, MNRAS, 472, 2028
Furlanetto S. R., Mirocha J., 2022, MNRAS, 511, 3895
Garratt T. K. et al., 2023, MNRAS, 520, 3669
Gehrels N., 1986, ApJ, 303, 336
Glazebrook K. et al., 2017, Nature, 544, 71
Griffin M. J. et al., 2010, A&A, 518, L3
Guglielmetti F. et al., 2023, Phys. Sci. Forum, 9, 18
Gullberg B. et al., 2019, MNRAS, 490, 4956
Hagimoto M. et al., 2023, MNRAS, 521, 5508
Hainline L. J., Blain A. W., Smail I., Alexander D. M., Armus L., Chapman S. C., Ivison R. J., 2011, ApJ, 740, 96
Harrington K. C. et al., 2016, MNRAS, 458, 4383
Harrington K. C. et al., 2021, ApJ, 908, 95
Hatsukade B., Tamura Y., Iono D., Matsuda Y., Hayashi M., Oguri M., 2015, PASJ, 67, 93
Henkel C., Downes D., Weiß A., Riechers D., Walter F., 2010, A&A, 516, A111
Herrera-Camus R. et al., 2018, ApJ, 861, 94
Hickox R. C. et al., 2012, MNRAS, 421, 284
Hlavacek-Larrondo J., Li Y., Churazov E., 2022, in Bambi C., Santangelo A., eds, Handbook of X-ray and Gamma-ray Astrophysics. Edited by Cosimo Bambi and Andrea. Springer Living Reference Work, p. 5
Hodge J. A. et al., 2013, ApJ, 768, 91
Hodge J. A. et al., 2016, ApJ, 833, 103
Hodge J. A. et al., 2019, ApJ, 876, 130

Hopkins P. F., Hernquist L., Cox T. J., Kereš D., 2008, ApJS, 175, 356
Hughes D. H. et al., 1998, Nature, 394, 241
Ikarashi S. et al., 2017, ApJ, 849, L36
Ikeda R. et al., 2022, ApJ, 933, 11
Inami H. et al., 2022, MNRAS, 515, 3126
Indriolo N., Bergin E. A., Falgarone E., Godard B., Zwaan M. A., Neufeld D. A., Wolfire M. G., 2018, ApJ, 865, 127
Ismail D. et al., 2023, A&A, 678, A27
Ivison R. J. et al., 2010, A&A, 518, L35
Ivison R. J. et al., 2016, ApJ, 832, 78
Jorsater S., van Moorsel G. A., 1995, AJ, 110, 2037
Kamieneski P. S. et al., 2024, ApJ, 961, 2
Karim A. et al., 2013, MNRAS, 432, 2
Kennicutt Robert C. J., 1989, ApJ, 344, 685
Kennicutt Robert C. J., 1998, ApJ, 498, 541
Kennicutt Robert C. J., De Los Reyes M. A. C., 2021, ApJ, 908, 61
Kerr A. R. et al., 2004, in Narayanan G., ed., Fifteenth Int. Symp. Space Terahertz Technology. p. 55
Kerr A. R., Pan S.-K., Claude S. M. X., Dindo P., Lichtenberger A. W., Effland J. E., Lauria E. F., 2014, IEEE Trans. Terahertz Sci. Technol., 4, 201
Krumholz M. R., Dekel A., McKee C. F., 2012, ApJ, 745, 69
Le Fèvre O. et al., 2020, A&A, 643, A1
Lee M. M. et al., 2019, ApJ, 883, L29
Lee M. M. et al., 2021, ApJ, 913, 41
Liao C.-L. et al., 2024, ApJ, 961, 226
Lilly S. J., Eales S. A., Gear W. K. P., Hammer F., Le Fèvre O., Crampton D., Bond J. R., Dunne L., 1999, ApJ, 518, 641
Long A. S., Casey C. M., del P. Lagos C., Lambrides E. L., Zavala J. A., Champagne J., Cooper O. R., Cooray A. R., 2023, ApJ, 953, 11
Madau P., Dickinson M., 2014, ARA&A, 52, 415
Mahieu S. et al., 2012, IEEE Trans. Terahertz Sci. Technol., 2, 29
Maiolino R., Mannucci F., 2019, A&AR, 27, 3
Man A., Belli S., 2018, Nat. Astron., 2, 695
Maresca J. et al., 2022, MNRAS, 512, 2426
Martín S. et al., 2021, A&A, 656, A46
McMullin J. P., Waters B., Schiebel D., Young W., Golap K., 2007, in Shaw R. A., Hill F., Bell D. J., eds, ASP Conf. Ser. Vol. 376, Astronomical Data Analysis Software and Systems XVI. Astron. Soc. Pac., San Francisco, p. 127
Meixner M. et al., 2019, preprint (arXiv:1912.06213)
Merlin E. et al., 2019, MNRAS, 490, 3309
Montaña A. et al., 2021, MNRAS, 505, 5260
Narayanan D., Cox T. J., Hayward C. C., Younger J. D., Hernquist L., 2009, MNRAS, 400, 1919
Narayanan D. et al., 2015, Nature, 525, 496
Nayyeri H. et al., 2016, ApJ, 823, 17
Negrello M., Perrotta F., González-Nuevo J., Silva L., de Zotti G., Granato G. L., Baccigalupi C., Danese L., 2007, MNRAS, 377, 1557
Negrello M. et al., 2017, MNRAS, 465, 3558
Nightingale J. W., Dye S., 2015, MNRAS, 452, 2940
Nightingale J. W., Dye S., Massey R. J., 2018, MNRAS, 478, 4738
Nightingale J. et al., 2021, J. Open Source Softw., 6, 2825
Novak M. et al., 2019, ApJ, 881, 63
Oliver S. J. et al., 2012, MNRAS, 424, 1614
Oteo I. et al., 2017, ApJ, 850, 170
Oteo I. et al., 2018, ApJ, 856, 72
Pantoni L. et al., 2021, MNRAS, 504, 928
Pearson E. A. et al., 2013, MNRAS, 435, 2753
Planck Collaboration VI, 2020, A&A, 641, A6
Posses A. et al., 2024, preprint (arXiv:2403.03379)
Powell D., Vegetti S., McKean J. P., Spingola C., Rizzo F., Stacey H. R., 2021, MNRAS, 501, 515
Quirós-Rojas M., Montaña A., Zavala J. A., Aretxaga I., Hughes D. H., 2024, MNRAS, 533, 2966
Ramos Padilla A. F., Wang L., van der Tak F. F. S., Trager S. C., 2023, A&A, 679, A131
Rangwala N. et al., 2011, ApJ, 743, 94
Rangwala N., Maloney P. R., Glenn J., Wilson C. D., Kamenetzky J., Schirm M. R. P., Spinoglio L., Pereira Santaella M., 2014, ApJ, 788, 147
Reuter C. et al., 2020, ApJ, 902, 78
Reuter C. et al., 2023, ApJ, 948, 44
Riechers D. A., Walter F., Carilli C. L., Weiss A., Bertoldi F., Menten K. M., Knudsen K. K., Cox P., 2006, ApJ, 645, L13
Riechers D. A., Weiß A., Walter F., Wagg J., 2010, ApJ, 725, 1032
Riechers D. A. et al., 2013, Nature, 496, 329
Riechers D. A., Cooray A., Pérez-Fournon I., Neri R., 2021, ApJ, 913, 141
Rizzo F., Vegetti S., Powell D., Fraternali F., McKean J. P., Stacey H. R., White S. D. M., 2020, Nature, 584, 201
Rizzo F. et al., 2024, A&A, 689, A273
Rosenberg M. J. F. et al., 2015, ApJ, 801, 72
Rowan-Robinson M. et al., 2018, A&A, 619, A169
Rujopakarn W. et al., 2019, ApJ, 882, 107
Rybak M., McKean J. P., Vegetti S., Andreani P., White S. D. M., 2015, MNRAS, 451, L40
Rybak M. et al., 2019, ApJ, 876, 112
Rybak M. et al., 2022, A&A, 667, A70
Sanders D. B., Soifer B. T., Elias J. H., Madore B. F., Matthews K., Neugebauer G., Scoville N. Z., 1988, ApJ, 325, 74
Schmidt M., 1959, ApJ, 129, 243
Schreiber C. et al., 2018, A&A, 618, A85
Sekimoto Y., Iizuko Y., Satou N., Ito T., Kumagai K., Kamikura M., Naruse M., Shan W. L., 2008, in Wild W., ed., Proc. Ninteenth Int. Symp. Space Terahertz Technology. p. 253
Serjeant S., 2012, MNRAS, 424, 2429
Serjeant S., 2024, Res. Notes Am. Astron. Soc., 8, 52
Sérsic J. L., 1963, Bol. Asoc. Argentina Astron. La Plata Argentina, 6, 41
Shirley R. et al., 2021, MNRAS, 507, 129
Simpson J. M. et al., 2019, ApJ, 880, 43
Smail I., Ivison R. J., Blain A. W., 1997, ApJ, 490, L5
Smail I. et al., 2023, ApJ, 958, 36
Spilker J. S. et al., 2014, ApJ, 785, 149
Spilker J. S., Bezanson R., Marrone D. P., Weiner B. J., Whitaker K. E., Williams C. C., 2016, ApJ, 832, 19
Spilker J. S. et al., 2018, Science, 361, 1016
Spilker J. S. et al., 2020a, ApJ, 905, 85
Spilker J. S. et al., 2020b, ApJ, 905, 86
Springel V., 2005, MNRAS, 364, 1105
Stacey G. J., 2011, IEEE Trans. Terahertz Sci. Technol., 1, 241
Stanley F. et al., 2023, ApJ, 945, 24
Straatman C. M. S. et al., 2014, ApJ, 783, L14
Sulzenauer N., Dannerbauer H., Díaz-Sánchez A., Ziegler B., Iglesias-Groth S., Rebolo R., 2021, ApJ, 923, L27
Sun F. et al., 2021, ApJ, 908, 192
Suyu S. H., Marshall P. J., Hobson M. P., Blandford R. D., 2006, MNRAS, 371, 983
Swinbank A. M. et al., 2010, Nature, 464, 733
Tacconi L. J. et al., 2013, ApJ, 768, 74
Tadaki K.-i. et al., 2017, ApJ, 834, 135
Tadaki K.-i. et al., 2020, ApJ, 901, 74
Tadaki K.-i. et al., 2022, PASJ, 74, L9
Tamura Y., Oguri M., Iono D., Hatsukade B., Matsuda Y., Hayashi M., 2015, PASJ, 67, 72
Tielens A. G. G. M., Hollenbach D., 1985, ApJ, 291, 722
Toft S. et al., 2014, ApJ, 782, 68
Trujillo I., Erwin P., Asensio Ramos A., Graham A. W., 2004, AJ, 127, 1917
Tsukui T., Wisnioski E., Krumholz M. R., Battisti A., 2023, MNRAS, 523, 4654
Ura R. et al., 2023, ApJ, 948, 3
Urquhart S. A. et al., 2022, MNRAS, 511, 3017
Valentino F. et al., 2020a, A&A, 641, A155
Valentino F. et al., 2020b, ApJ, 890, 24
Valiante E. et al., 2016, MNRAS, 462, 3146
van der Werf P. P. et al., 2010, A&A, 518, L42
Viero M. P. et al., 2014, ApJS, 210, 22

Vogelsberger M. et al., 2020, MNRAS, 492, 5167
Ward B. A. et al., 2022, MNRAS, 510, 2261
Warren S. J., Dye S., 2003, ApJ, 590, 673
Weiß A., Downes D., Neri R., Walter F., Henkel C., Wilner D. J., Wagg J., Wiklind T., 2007, A&A, 467, 955
Weiß A. et al., 2009, ApJ, 707, 1201
Yang C. et al., 2016, A&A, 595, A80
Yang C. et al., 2017, A&A, 608, A144
Yang C. et al., 2023, A&A, 680, A95
Zavala J. A., Casey C. M., da Cunha E., Spilker J., Staguhn J., Hodge J., Drew P. M., 2018, ApJ, 869, 71
Zavala J. A. et al., 2022, ApJ, 933, 242
Zhang Z.-Y. et al., 2018, MNRAS, 481, 59
Zolotov A. et al., 2015, MNRAS, 450, 2327

APPENDIX A: GRAPH TO OPTIMIZE THE OBSERVING BANDS

Fig. A1 shows the tool used to define the optimum observing conditions for efficiently targeting as many spectral lines as possible.

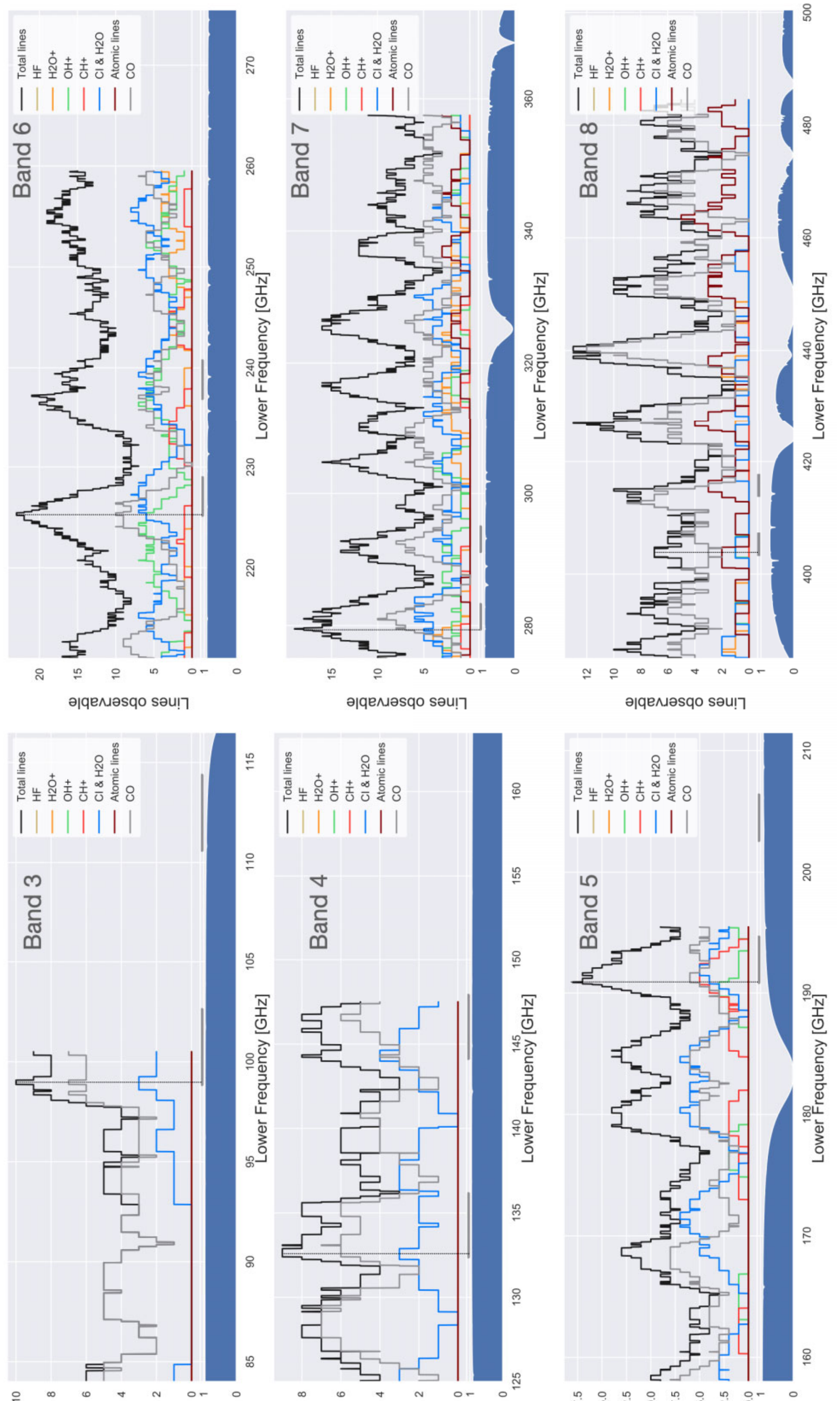

Figure A1. These six graphs were used to find the optimum tuning of each of the bands to target the most lines given a fixed spectral set-up. The *x*-axis shows the frequency set-up by indicating the lowest frequency of the spectral windows, and the lower and upper sidebands are separated by 8 GHz. The grey bar indicates the selected frequency set-up, and the dashed line indicates the total number of expected lines that are targeted with the observations. The optical transparency of the atmosphere is indicated by the bottom panel of each graph, between 1 (fully transparent) and 0 (fully opaque), in order to evaluate the effect of the optical transmission while targeting as many lines as possible. Notable absorptions include the water feature in Band 5, a central absorption component in Band 7, and the majority of Band 8. As such, we did not always choose the highest position in the top panel for our observations.

APPENDIX B: SOURCES WITHOUT SPECTROSCOPIC REDSHIFTS

In this section, we report the seven sources without spectroscopic redshifts that were included in the field of view of ALMA. We present their continua in Fig. B1.

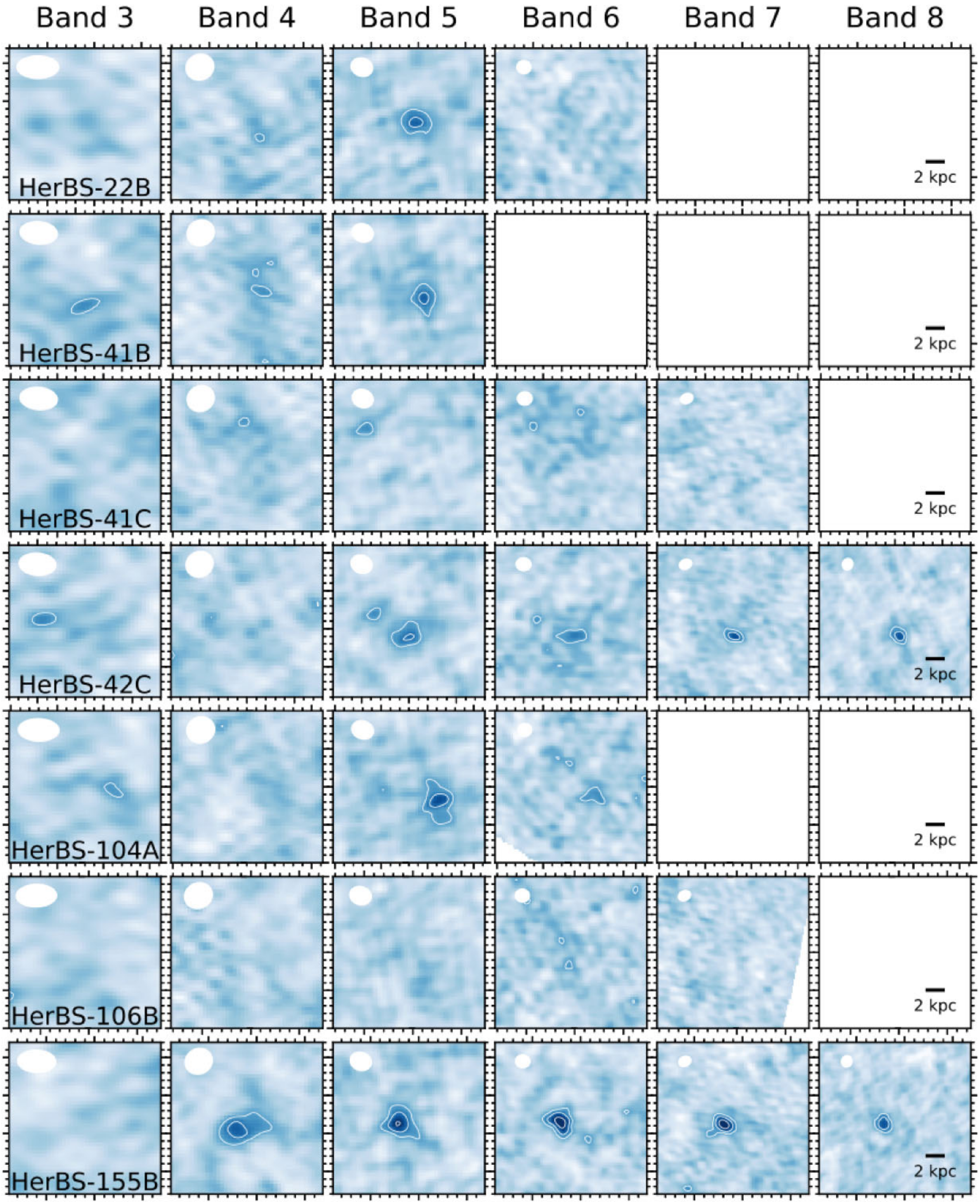

Figure B1. These sources are not the main targets in the ANGELS data, but were found through unresolved BEARS observations (Bendo et al. 2023). They do not have spectroscopic redshifts, and the majority are not completely covered by the primary beam (PB-COR < 0.3) for the highest frequencies. Here, we show the images before the primary beam correction to better showcase the source across the bands.

APPENDIX C: SPECTRAL LINE PROFILES

The tabulated measured properties of the spectral lines are shown in Table C1. All detected lines are shown in Figs C1.

Table C1. Line tables.

Line	Frequency [GHz]	Band	SdV [Jy km s^{-1}]	dV [km s^{-1}]	$V - V_{CO}$ [km s^{-1}]
			HerBS-21 $z = 3.323$		
[C I] 609 μm	113.847	Band 3	< 1.54		
CO (5−4)	133.251	Band 4	14.18 ± 3.34	521 ± 92	−23 ± 39
CH^+ (1−0)	193.171	Band 5	−1.21 ± 0.75	360 ± 169	205 ± 71
OH^+ $(1_2 - 0_1)$	224.799	Band 6	−6.1 ± 1.45	439 ± 78	189 ± 33
OH^+ $(1_1 - 0_1)$	238.982	Band 6	−2.54 ± 0.95	177 ± 50	142 ± 21
CO (9−8)	239.851	Band 6	8.99 ± 2.82	642 ± 152	13 ± 64
CO (11−10)	293.311	Band 7	4.91 ± 1.4	416 ± 89	−109 ± 37
			HerBS-22 $z = 3.051$		
CO (4−3)	113.820	Band 3	11.72 ± 3.25	568 ± 118	34 ± 50
CH^+ (1−0)	206.141	Band 5	−0.75 ± 0.36	107 ± 39	−138 ± 15
OH^+ $(1_0 - 0_1)$	224.428	Band 6	−1.84 ± 0.75	178 ± 55	−65 ± 23
OH^+ $(1_2 - 0_1)$	239.893	Band 6	−5.14 ± 1.0	470 ± 0	−140 ± 44
H_2O^+ $(1_{1,1} - 0_{0,0})$	281.373	Band 7	11.89 ± 3.19	941 ± 163	869 ± 93
			HerBS-25 $z = 2.912$		
CO (5−4)	147.324	Band 4	18.96 ± 2.17	226 ± 19	9 ± 8
H_2O $(2_{1,1} - 2_{0,2})$	192.238	Band 5	6.35 ± 2.81	478 ± 160	−73 ± 68
CO (7−6)	206.220	Band 5	12.61 ± 3.66	249 ± 54	−34 ± 23
H_2O $(3_{1,2} - 3_{0,3})$	280.512	Band 7	5.93 ± 2.52	196 ± 63	−106 ± 26
H_2O^+ $(1_{1,1} - 0_{0,0})$	291.299	Band 7	3.88 ± 2.7	136 ± 71	−128 ± 30
CO (10−9)	294.661	Band 7	17.76 ± 4.98	941 ± 185	357 ± 93
			HerBS-36 $z = 3.095$		
CO (4−3)	112.619	Band 3	6.88 ± 1.85	464 ± 94	−18 ± 40
CH^+ (1−0)	203.926	Band 5	−2.23 ± 0.38	283 ± 36	10 ± 15
CO (8−7)	225.208	Band 6	5.80 ± 2.03	440 ± 116	−4 ± 49
CO (10−9)	281.541	Band 7	4.69 ± 1.79	392 ± 112	56 ± 48
CH^+ (2−1)	407.638	Band 8	−5.21 ± 2.03	128 ± 43	64 ± 16
			HerBS-41A $z = 4.098$		
CO (5−4)	113.147	Band 3	5.05 ± 1.64	710 ± 174	12 ± 74
CO (6−5)	135.869	Band 4	4.35 ± 1.51	842 ± 221	248 ± 93
H_2O $(2_{1,1} - 2_{0,2})$	147.515	Band 4	< 1.89		
H_2O $(2_{0,2} - 1_{1,1})$	193.787	Band 5	1.31 ± 0.97	647 ± 363	−232 ± 154
OH^+ $(1_1 - 0_1)$	202.652	Band 5	−0.88 ± −0.47	349 ± 147	−540 ± 57
CO (9−8)	203.663	Band 5	3.44 ± 2.1	790 ± 363	−37 ± 154
H_2O^+ $(1_{1,1} - 0_{0,0})$	223.531	Band 6	< 2.9		
CO (10−9)	226.111	Band 6	1.59 ± 1.15	940 ± 524	−21 ± 211
CO (13−12)	293.944	Band 7	5.77 ± 1.2	941 ± 72	−200 ± 89
[O I] 145 μm	404.081	Band 8	10.27 ± 2.72	941 ± 135	−481 ± 106
CO (18−17)	406.999	Band 8	3.15 ± 1.11	941 ± 4	−173 ± 299
			HerBS-42A $z = 3.307$		
CO (5−4)	133.787	Band 4	13.42 ± 1.75	667 ± 65	−18 ± 27
CH^+ (1−0)	193.889	Band 5	< 1.13		
OH^+ $(1_1 - 0_1)$	225.634	Band 6	−0.4 ± 0.32	342 ± 203	−418 ± 86
OH^+ $(1_2 - 0_1)$	239.87	Band 6	−0.73 ± 0.5	340 ± 177	−182 ± 75
CO (9−8)	240.775	Band 6	10.6 ± 2.84	647 ± 134	−18 ± 53
CO (11−10)	294.401	Band 7	7.54 ± 2.94	941 ± 190	255 ± 153
			HerBS-42B $z = 3.314$		
[C I] 609 μm	114.085	Band 3	< 2.28		
CO (5−4)	133.601	Band 4	3.35 ± 1.58	564 ± 201	16 ± 85
CH^+ (1−0)	193.574	Band 5	< 1.67		
CO (9−8)	240.482	Band 6	1.84 ± 0.74	150 ± 45	42 ± 19
OH^+ $(1_2 - 0_1)$	239.48	Band 6	< 3.44		
CO (11−10)	293.923	Band 7	< 2.90		

Table C1 – *continued*

Line	Frequency [GHz]	Band	SdV [Jy km s^{-1}]	dV [km s^{-1}]	$V - V_{CO}$ [km s^{-1}]
			HerBS-81A $z = 3.160$		
CO (4−3)	110.800	Band 3	6.05 ± 2.05	587 ± 150	-63 ± 63
CO (7−6)	194.002	Band 5	4.38 ± 1.69	442 ± 129	149 ± 54
[C I] 370 µm	194.509	Band 5	< 1.32		
H_2O ($2_{0,2} - 1_{1,1}$)	237.482	Band 6	< 1.54		
H_2O ($3_{2,1} - 3_{1,2}$)	279.546	Band 7	8.32 ± 4.78	762 ± 336	-337 ± 137
			HerBS-81B $z = 2.588$		
CO (6−5)	192.976	Band 5	3.16 ± 1.93	870 ± 401	61 ± 167
CO (7−6)	225.139	Band 6	2.46 ± 1.96	932 ± 563	60 ± 235
[C I] 370 µm	225.769	Band 6	< 1.62		
CO (13−12)	418.115	Band 8	< 3.5		
[N II] 205 µm	407.678	Band 8	< 3.87		
			HerBS-86 $z = 2.564$		
CO (6−5)	194.045	Band 5	5.36 ± 1.68	532 ± 126	-3 ± 53
CO (7−6)	226.320	Band 6	5.32 ± 1.68	446 ± 106	-8 ± 45
			HerBS-87 $z = 2.059$		
CO (3−2)	113.066	Band 3	5.16 ± 2.03	474 ± 156	70 ± 64
CO (6−5)	226.127	Band 6	13.84 ± 4.06	280 ± 62	118 ± 26
			HerBS-93 $z = 2.402$		
CO (3−2)	101.638	Band 3	4.01 ± 1.53	821 ± 237	0 ± 100
CO (4−3)	135.547	Band 4	8.72 ± 3.22	782 ± 218	-46 ± 92
[C I] 609 µm	144.668	Band 4	4.79 ± 2.18	371 ± 140	203 ± 52
CO (6−5)	203.420	Band 5	6.1 ± 2.08	941 ± 101	464 ± 215
[C I] 370 µm	237.987	Band 6	2.07 ± 1.34	155 ± 76	499 ± 3
CO (12−11)	406.84	Band 8	< 2.67		
			HerBS-104 $z = 1.536$		
[C I] 609 µm	194.070	Band 5	3.56 ± 1.0	324 ± 68	58 ± 29
OH^+ ($1_1 - 0_1$)	407.397	Band 8	-2.09 ± 1.03	121 ± 45	64 ± 19
			HerBS-106 $z = 2.369$		
[C I] 609 µm	146.0854	Band 4	4.36 ± 1.78	229 ± 70	-31 ± 29
CO (6−5)	205.254	Band 5	9.49 ± 2.12	542 ± 91	-11 ± 39
H_2O ($2_{1,1} - 2_{0,2}$)	223.221	Band 6	< 1.20		
CO (7−6)	239.507	Band 6	5.02 ± 2.17	219 ± 71	-14 ± 30
[C I] 370 µm	240.177	Band 6	23.39 ± 5.68	941 ± 116	-58 ± 96
H_2O ($2_{0,2} - 1_{1,1}$)	293.24	Band 7	< 4.91		
			HerBS-155 $z = 3.077$		
CO (4−3)	113.121	Band 3	5.32 ± 0.52	144 ± 15	20 ± 12
CH^+ (1−0)	204.827	Band 5	< 2.33		
OH^+ ($1_0 - 0_1$)	222.997	Band 6	< 2.82		
CO (8−7)	226.150	Band 6	5.36 ± 1.75	212 ± 52	-2 ± 22
H_2O^+ ($1_{1,1} - 0_{0,0}$)	279.51	Band 7	< 1.14		
CO (10-−9)	282.735	Band 7	< 6.18		
			HerBS-159A $z = 2.236$		
OH^+ ($1_0 - 0_1$)	280.951	Band 7	< 2.6		
			HerBS-159B z		
OH^+ ($1_0 - 0_1$)	280.951	Band 7	< 1.38		
			HerBS-170 $z = 4.182$		
CO (5−4)	111.188	Band 3	< 2.07		
CO (6−5)	133.426	Band 4	3.37 ± 1.59	421 ± 150	-15 ± 63
H_2O ($2_{1,1} - 2_{0,2}$)	145.079	Band 4	< 2.10		
H_2O ($3_{2,1} - 3_{1,2}$)	224.344	Band 6	4.8 ± 2.61	941 ± 479	43 ± 87
HF (1−0)	237.765	Band 6	< 2.3		
[N II] 205 µm	281.873	Band 7	4.36 ± 1.93	304 ± 102	51 ± 43
			HerBS-184 $z = 2.507$		
CO (3−2)	98.577	Band 3	4.32 ± 1.29	395 ± 89	6 ± 37
CH^+ (1−0)	238.118	Band 6	< 1.74		
H_2O ($2_{0,2} - 1_{1,1}$)	281.701	Band 7	1.39 ± 0.96	472 ± 245	-22 ± 104
OH^+ ($1_1 - 0_1$)	294.587	Band 7	< 1.74		
[N II] 205 µm	416.629	Band 8	4.15 ± 2.94	362 ± 194	4 ± 82

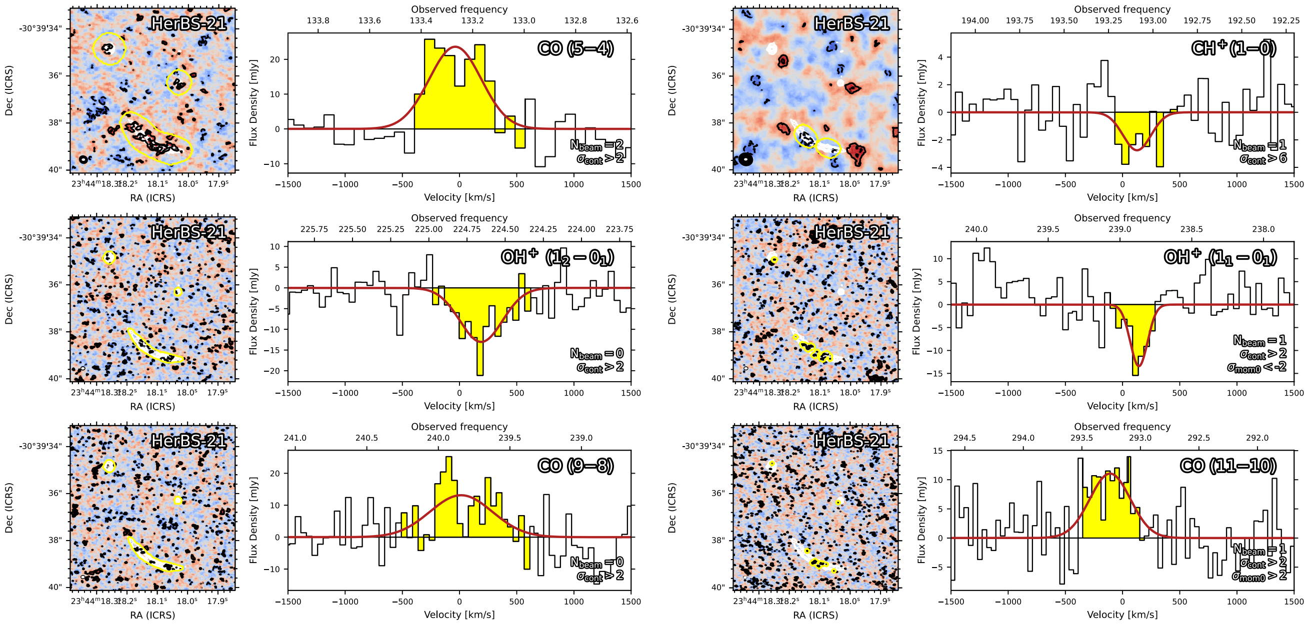

Figure C1. The moment-0 (left) and line spectra (right) of HerBS-21 at $z = 3.323$. The white contours show the untapered Band 7 image at $2, 3, 5, \dots, \sigma$, and the red solid/blue dashed contours show the $\pm 2, 3, 5, \dots, \sigma$ moment-0 line emission. The yellow contour shows the selected aperture based on the selection criteria highlighted in the bottom right of the spectrum, using an aperture based on the tapered Band 7 continuum ($\sigma_{\rm cont}$) and moment-0 ($\sigma_{\rm mom-0}$) emission, which are subsequently tapered by $N_{\rm beams}$ times the moment-0 beam. Similarly, the moment-0 image is created from the highlighted emission bins. The line properties listed in Table C1 are derived from the line fits.

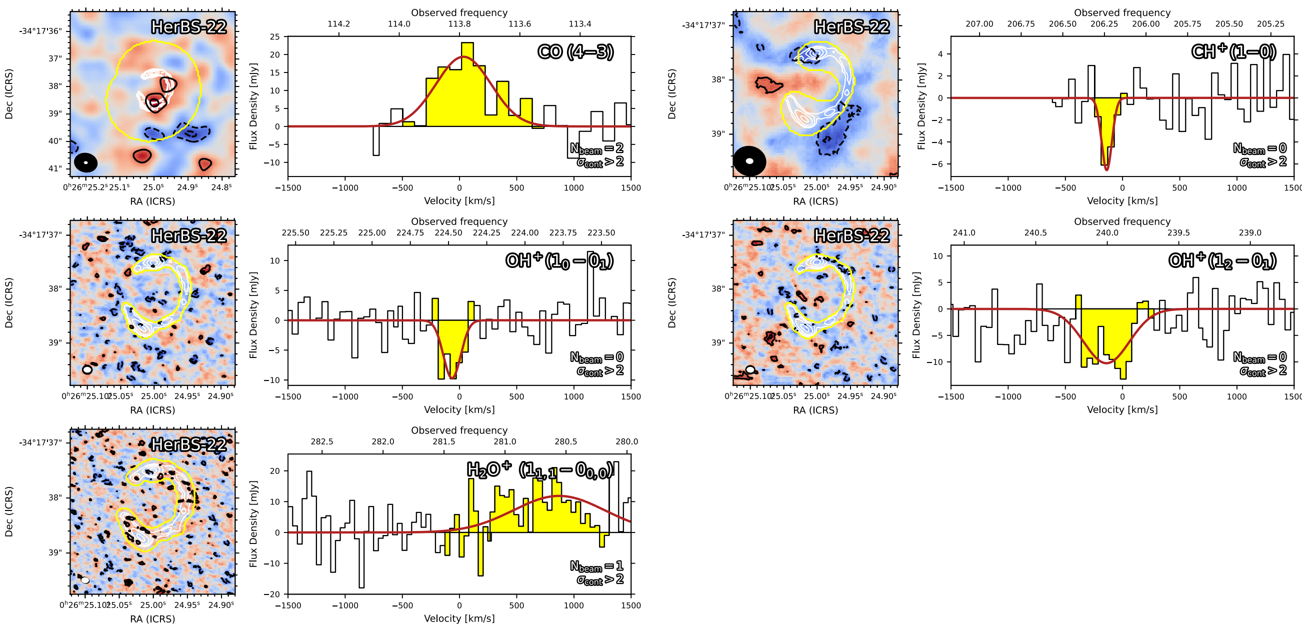

Figure C1. (*Continued*). The moment-0 (left) and line spectra (right) of HerBS-22 at $z = 3.050$.

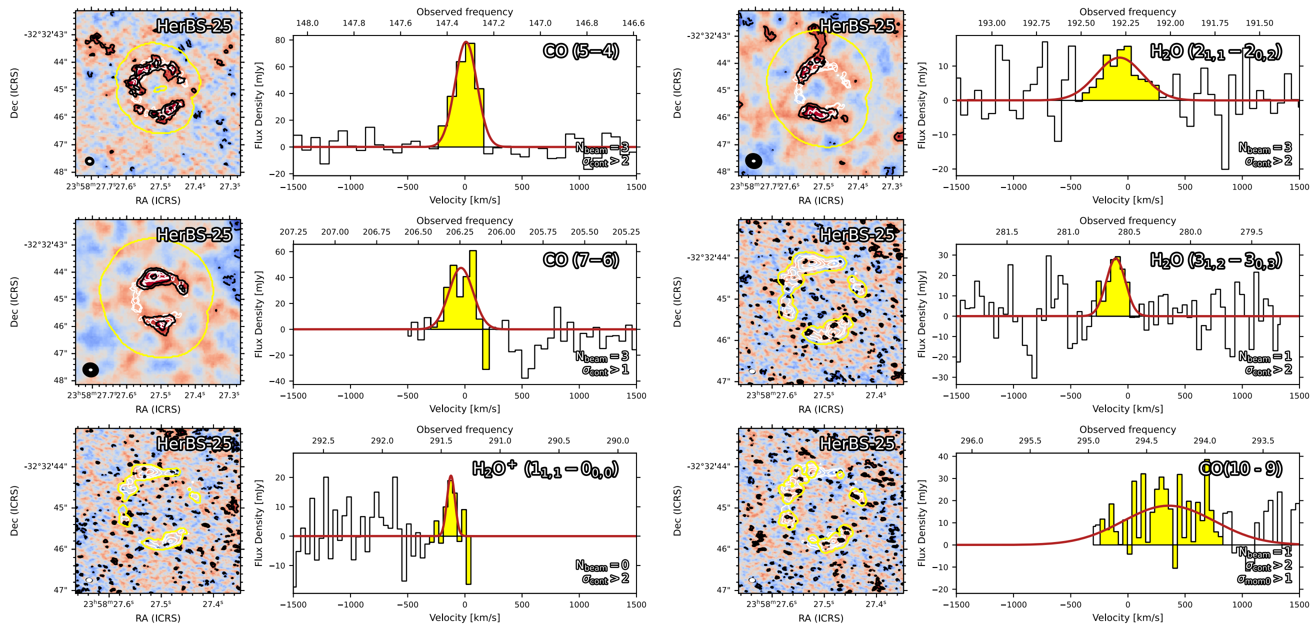

Figure C1. (*Continued*). The moment-0 (left) and line spectra (right) of HerBS-25 at $z = 2.912$.

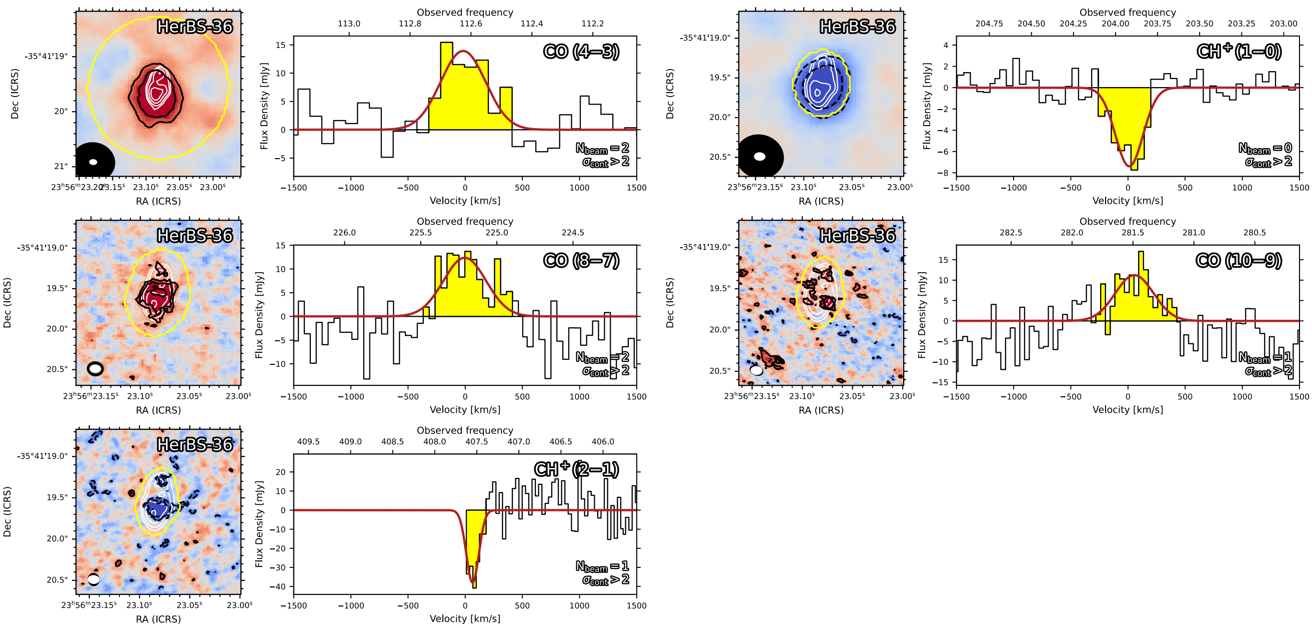

Figure C1. (*Continued*). The moment-0 (left) and line spectra (right) of HerBS-36 at $z = 3.095$.

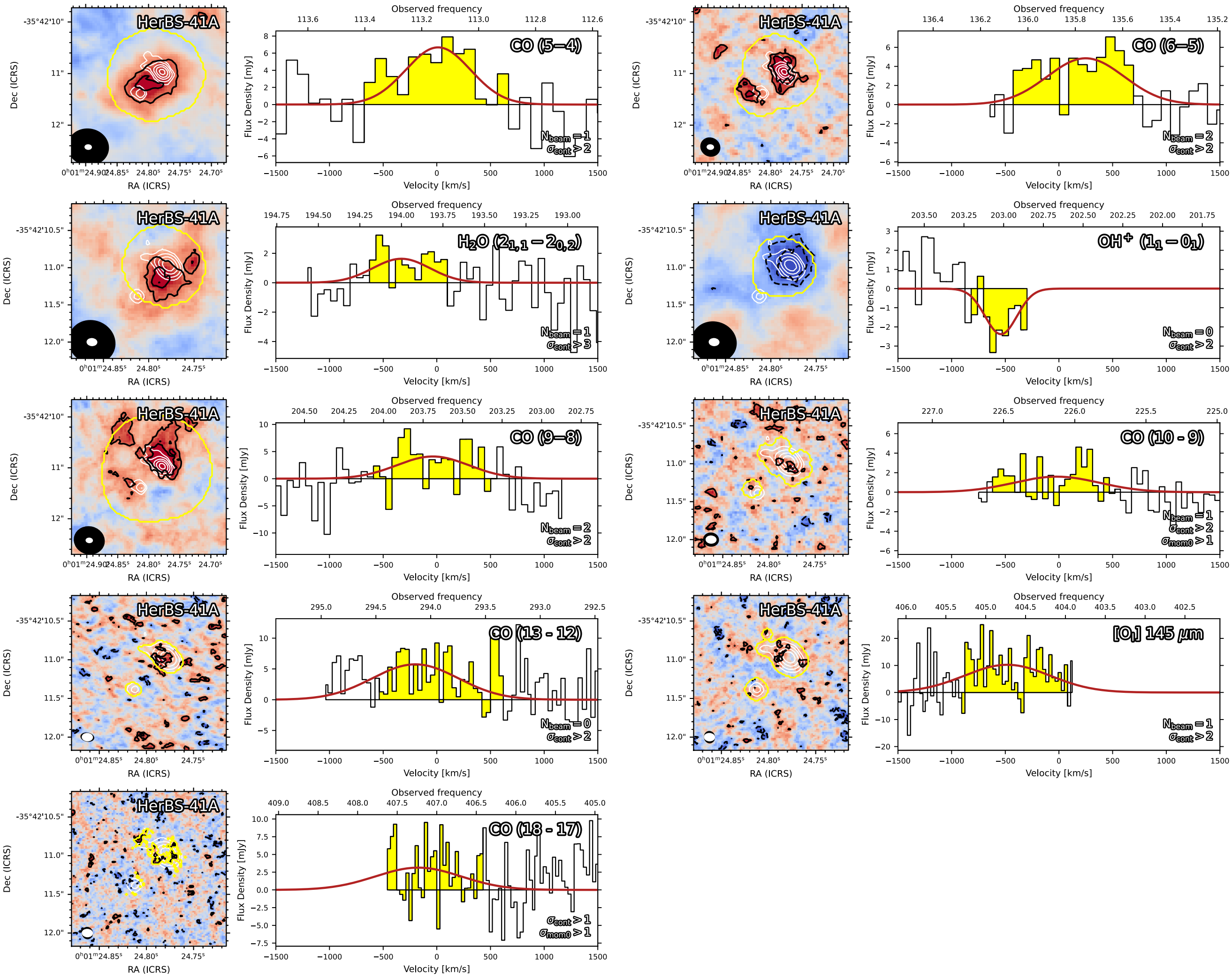

Figure C1. (*Continued*). The moment-0 (left) and line spectra (right) of HerBS-41A at $z = 4.098$.

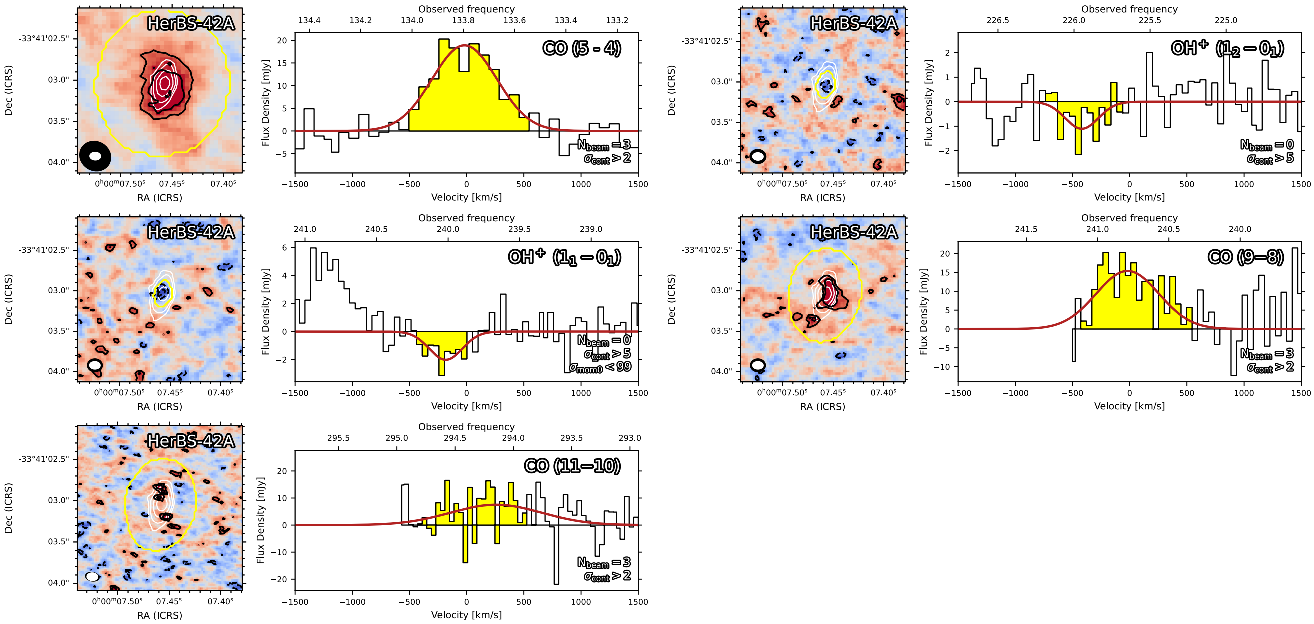

Figure C1. (*Continued*). The moment-0 (left) and line spectra (right) of HerBS-42A at $z = 3.307$.

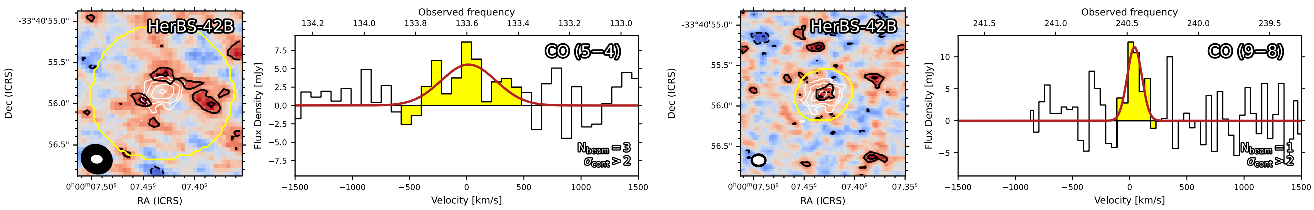

Figure C1. (*Continued*). The moment-0 (left) and line spectra (right) of HerBS-42B at $z = 3.314$.

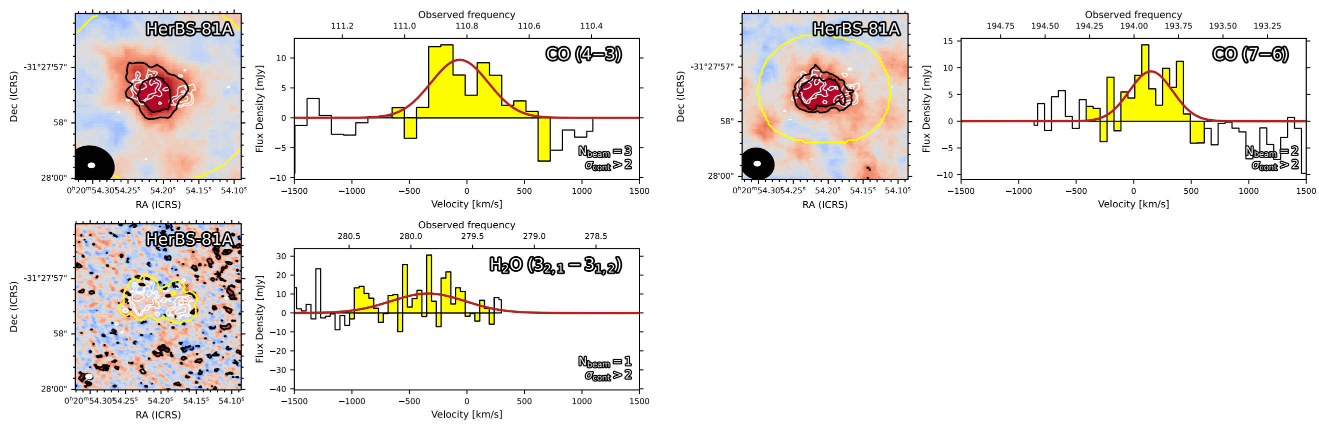

Figure C1. (*Continued*). The moment-0 (left) and line spectra (right) of HerBS-81A at $z = 3.160$.

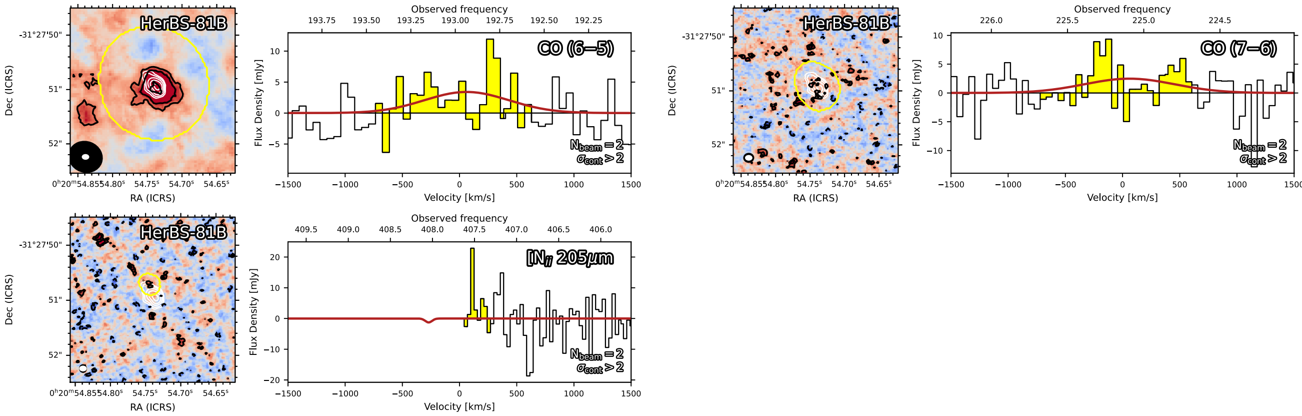

Figure C1. (*Continued*). The moment-0 (left) and line spectra (right) of HerBS-81B at $z = 2.588$.

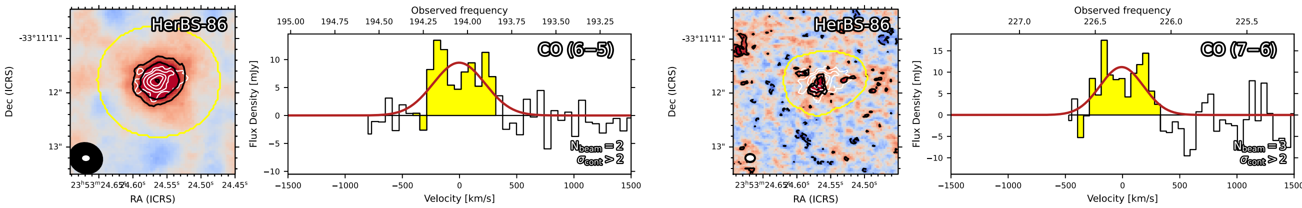

Figure C1. (*Continued*). The moment-0 (left) and line spectra (right) of HerBS-86 at $z = 2.564$.

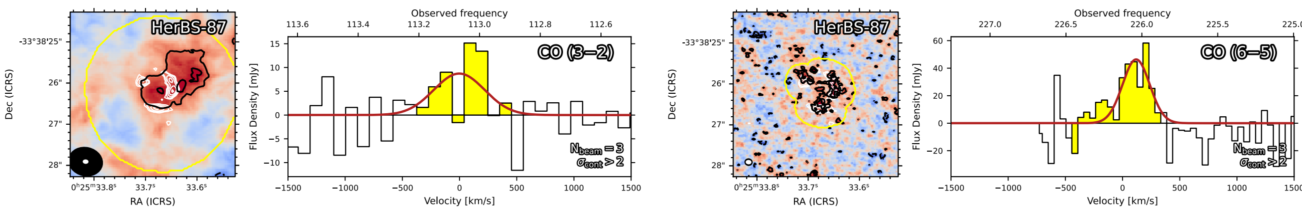

Figure C1. (*Continued*). The moment-0 (left) and line spectra (right) of HerBS-87 at $z = 2.059$.

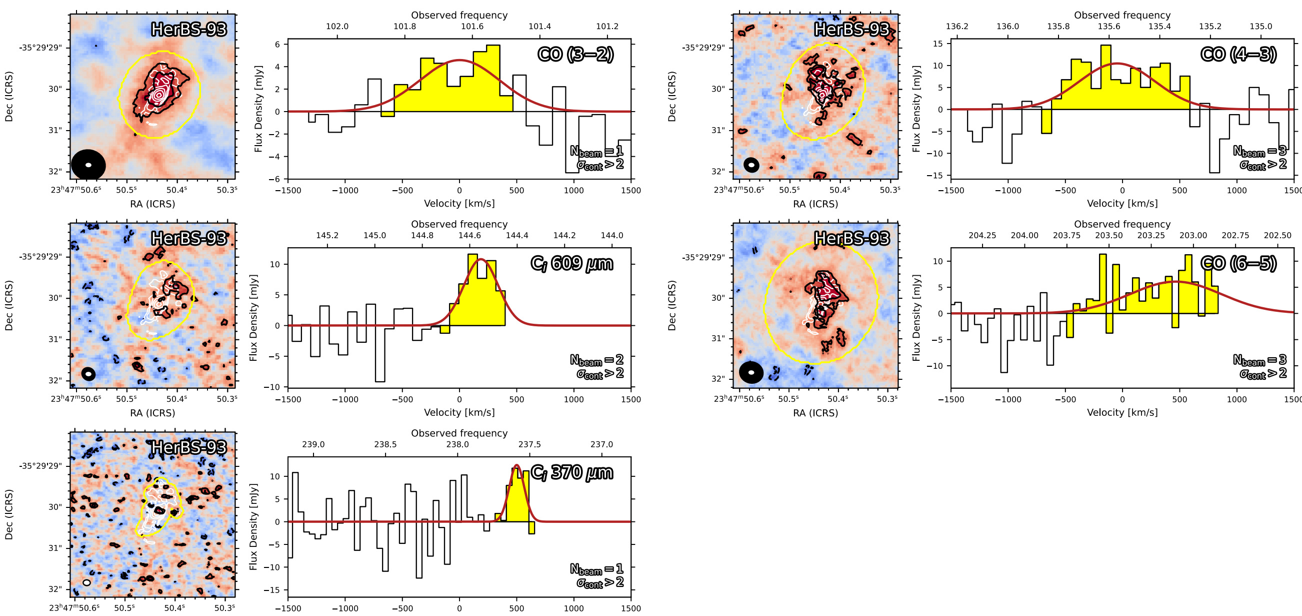

Figure C1. (*Continued*). The moment-0 (left) and line spectra (right) of HerBS-93 at $z = 2.402$.

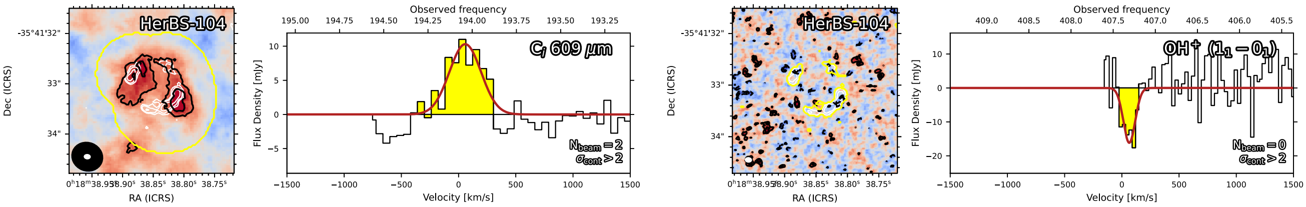

Figure C1. (*Continued*). The moment-0 (left) and line spectra (right) of HerBS-104 at $z = 1.536$.

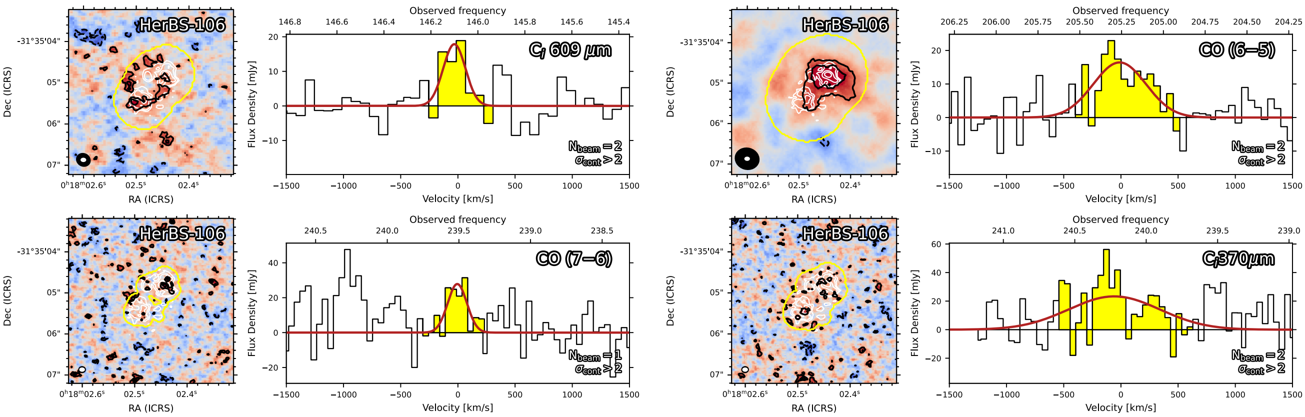

Figure C1. (*Continued*). The moment-0 (left) and line spectra (right) of HerBS-106 at $z = 2.369$.

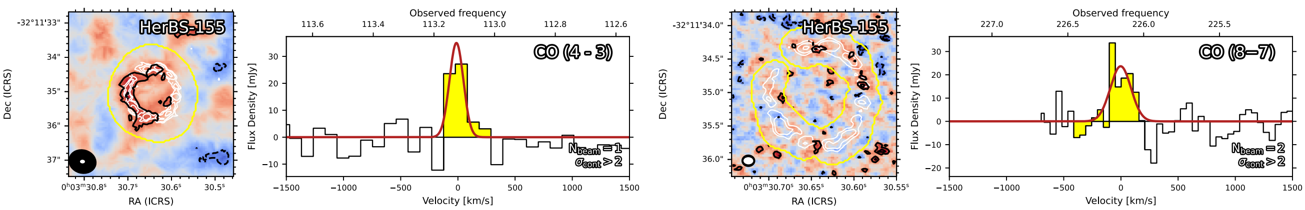

Figure C1. (*Continued*). The moment-0 (left) and line spectra (right) of HerBS-155 at $z = 3.077$.

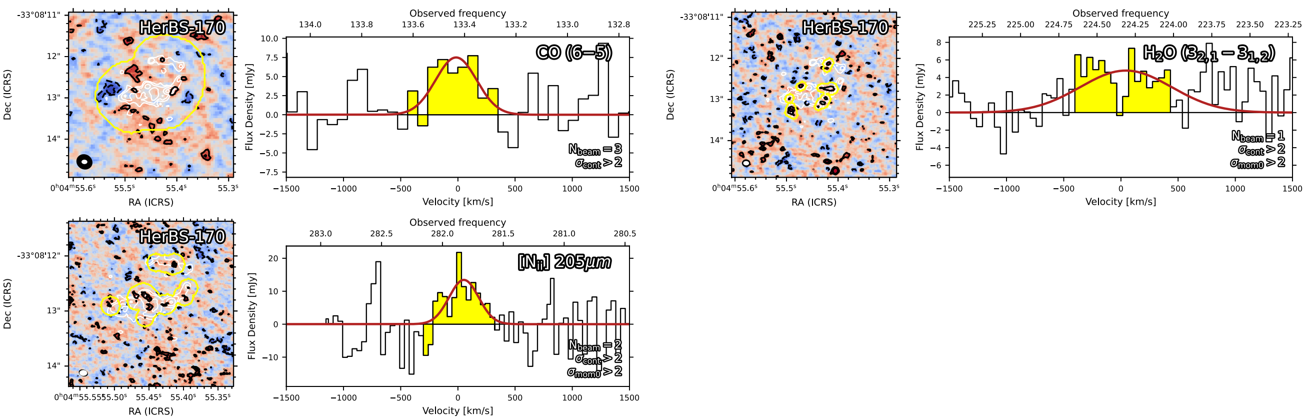

Figure C1. (*Continued*). The moment-0 (left) and line spectra (right) of HerBS-170 at $z = 4.182$.

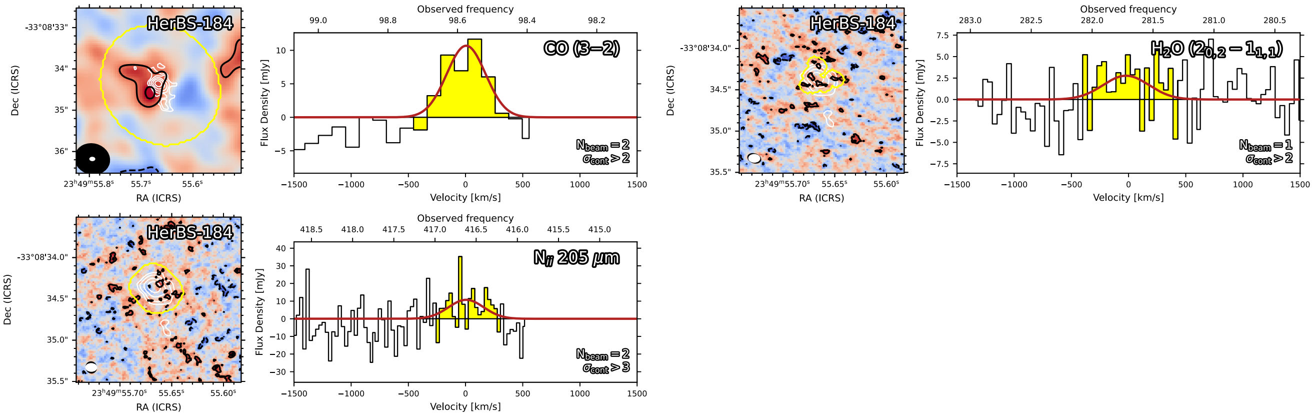

Figure C1. (*Continued*). The moment-0 (left) and line spectra (right) of HerBS-184 at $z = 2.507$.

APPENDIX D: INFRARED LUMINOSITIES OF ANGELS SOURCES

We provide the infrared luminosities for the ANGELS targets using three methodologies in Table D1: (1) using the Eyelash galaxy template (e.g. Ivison et al. 2016), (2) using the *Herschel*-derived template from Bakx et al. (2018, 2020b), and thirdly assuming a modified blackbody with a $\beta_{\rm dust} = 2.0$, based on the method outlined in Bakx et al. (2021). On average the luminosities of the first two methods are roughly 50 per cent higher than for a single-temperature fit, as much of the shorter wavelength emission is missed in a single-temperature fit, which reflects mostly the colder dust (see e.g. Eales et al. 1999). Meanwhile, the latter option also provides us an estimate of the dust masses for these targets, which are primarily at these colder dust temperatures.

Table D1. Infrared luminosities and dust masses for the ANGELS sources.

Source	z	r_{B7} [0−1]	μ	$\mu L_{\rm IR}^{\rm eye}$ [10^{12} L$_\odot$]	$L_{\rm IR}^{\rm eye}$ [10^{12} L$_\odot$]	$\mu L_{\rm IR}^{\rm B+18}$ [10^{12} L$_\odot$]	$L_{\rm IR}^{\rm B+18}$ [10^{12} L$_\odot$]	$T_{\rm d}$ [K]	$\mu L_{\rm IR}^{\rm fit}$ [10^{12} L$_\odot$]	$L_{\rm IR}^{\rm fit}$ [10^{12} L$_\odot$]	μM_d [10^8 M$_\odot$]	M_d [10^8 M$_\odot$]
21	3.323	1	9	51.7	5.7	56.3	6.2	34.1	46.3	5.1	109.4	12.1
22	3.050	1	18.8	45.5	2.4	50.5	2.6	32.6	39.2	2.0	121.7	6.4
25	2.912	1	9.2	34.8	3.7	38.7	4.2	30.6	28.7	3.1	130.9	14.2
36	3.095	1	4.1	40.3	9.8	44.7	10.9	33.4	35.5	8.6	95.4	23.2
41	4.098	1	2.6	42.5	16.3	45.6	17.5	35.9	40.3	15.5	70.3	27.0
42A	3.307	0.726	1	31.9	*31.9*	35.4	*35.4*	36.7	31.3	*31.3*	47.7	*47.7*
42B	3.314	0.274	1	12.0	*12.0*	13.4	*13.4*	36.8	11.8	*11.8*	17.9	*17.9*
81A	3.160	0.579	1	16.9	*16.9*	18.6	*18.6*	33.9	15.1	*15.1*	40.8	*40.8*
81B	2.584	0.421	1	8.5	*8.5*	9.6	*9.6*	29.2	6.8	*6.8*	37.2	*37.2*
86	2.564	1	1	17.8	*17.8*	20.2	*20.2*	28.1	13.7	*13.7*	103.1	*103.1*
87	1.860	1	8.7	13.2	1.5	15.6	1.8	25.9	9.2	1.0	113.7	13.0
93	2.400	1	1	15.2	*15.2*	17.5	*17.5*	27.6	11.5	*11.5*	97.5	*97.5*
104	1.540	1	6.3	10.7	1.7	12.6	2.0	24.6	6.6	1.0	113.1	17.9
106	2.369	1	2.3	20.9	9.0	24.2	10.5	31.7	17.9	7.8	66.2	28.7
155	3.077	0.860	28.3	20.2	0.7	22.2	0.8	30.6	16.6	0.6	75.1	2.6
159A	2.236	0.690	1	10.1	*10.1*	11.8	*11.8*	28.5	7.8	*7.8*	54.6	*54.6*
159B	2.236	0.310	1	4.5	*4.5*	5.3	*5.3*	28.5	3.5	*3.5*	24.5	24.5
170	4.184	1	1	38.1	*38.1*	41.5	*41.5*	38.2	37.2	*37.2*	45.0	*45.0*
184	2.507	1	1	18.6	*18.6*	21.5	*21.5*	30.6	15.4	*15.4*	69.9	*69.9*

Notes. Column 1: source name. Column 2: spectroscopic redshift. Column 3: Band 7 flux ratio between the component and other sources in the field. Column 4: magnifications as derived in Section 4. Columns 5 and 6: observed and magnification-corrected infrared luminosity derived from the Eyelash template (e.g. Ivison et al. 2016) using the $z_{\rm spec}$ fitted to the *Herschel* fluxes. Columns 7 and 8: observed and magnification-corrected infrared luminosity derived from the template in Bakx et al. (2018, 2020b) using the $z_{\rm spec}$ fitted to the *Herschel* fluxes. Columns 9–13: single-temperature modified blackbody using the $z_{\rm spec}$ fitted to the *Herschel* fluxes, assuming $\beta_{\rm dust} = 2.0$, providing the dust temperature, observed and magnification-corrected infrared luminosities, and observed and magnification-corrected dust masses using the methodology from Bakx et al. (2021). Italics indicate unchanged values in the case of an unlensed source.

APPENDIX E: COMPARISON OF BEARS AND ANGELS FLUXES

Fig. E1 shows the velocity-integrated flux densities for the six galaxies with line measurements of the same CO transition in both BEARS and ANGELS, and compare this against the resolved observations extracted using the same technique as the BEARS study (Urquhart et al. 2022), where the aperture is increased in a curve-of-growth fashion until an SNR of 5 is reached in the velocity-integrated flux density. The line fluxes of the resolved ANGELS observations are often higher than those extracted from the moderately resolved BEARS observations, and could point to differences between the curve-of-growth approach from BEARS (Urquhart et al. 2022). Similarly, unresolved and resolved studies (Jorsater & van Moorsel 1995; Czekala et al. 2021) have found different fluxes on the same object, such as the flux estimates from ALMA large program ALPINE when compared to the resolved CRISTAL study (Posses et al. 2024), or the flux estimates reported in resolved observations of bright AGNs (Novak et al. 2019). The origin of these issues is believed to arise from the deconvolution technique in TCLEAN that produces a combined image of background noise (in units of Jy/dirty beam) and signal (assuming a Gaussian PSF in units of Jy/clean beam). As a consequence, the fluxes from resolved maps might produce a different total flux estimate than those from unresolved observations.

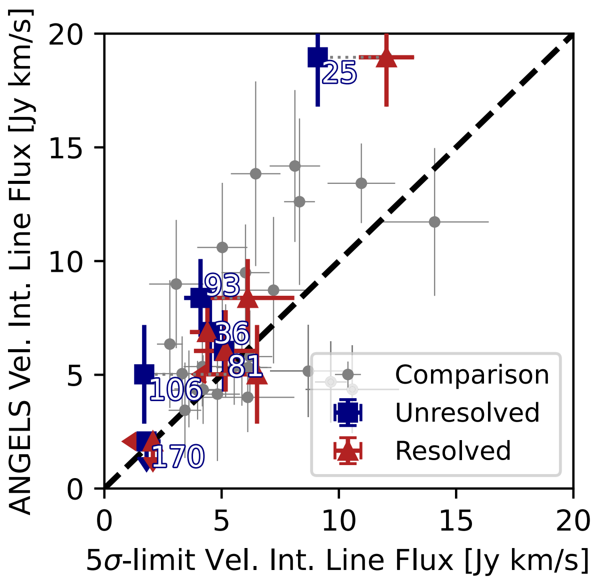

Figure E1. The velocity-integrated line fluxes of the BEARS (*x*-axis) and ANGELS (*y*-axis) flux extraction methods show discrepant flux densities across the six CO lines that are observed in both the unresolved (blue squares) and resolved (red triangles) data. A comparison of the fields with only resolved data (grey circles) also show a bias towards higher fluxes when the ANGELS method is used for flux extraction, suggesting the flux difference between BEARS and ANGELS is both because of the use of resolved data (i.e. Jorsater & van Moorsel 1995; Czekala et al. 2021) and because of a difference in methods of flux extraction.

APPENDIX F: RGB IMAGES FROM THE DUST CONTINUUM

Fig. F1 shows an RGB image using the Bands 6, 7, and 8 photometry of ANGELS across nineteen sources. These galaxies show a large diversity.

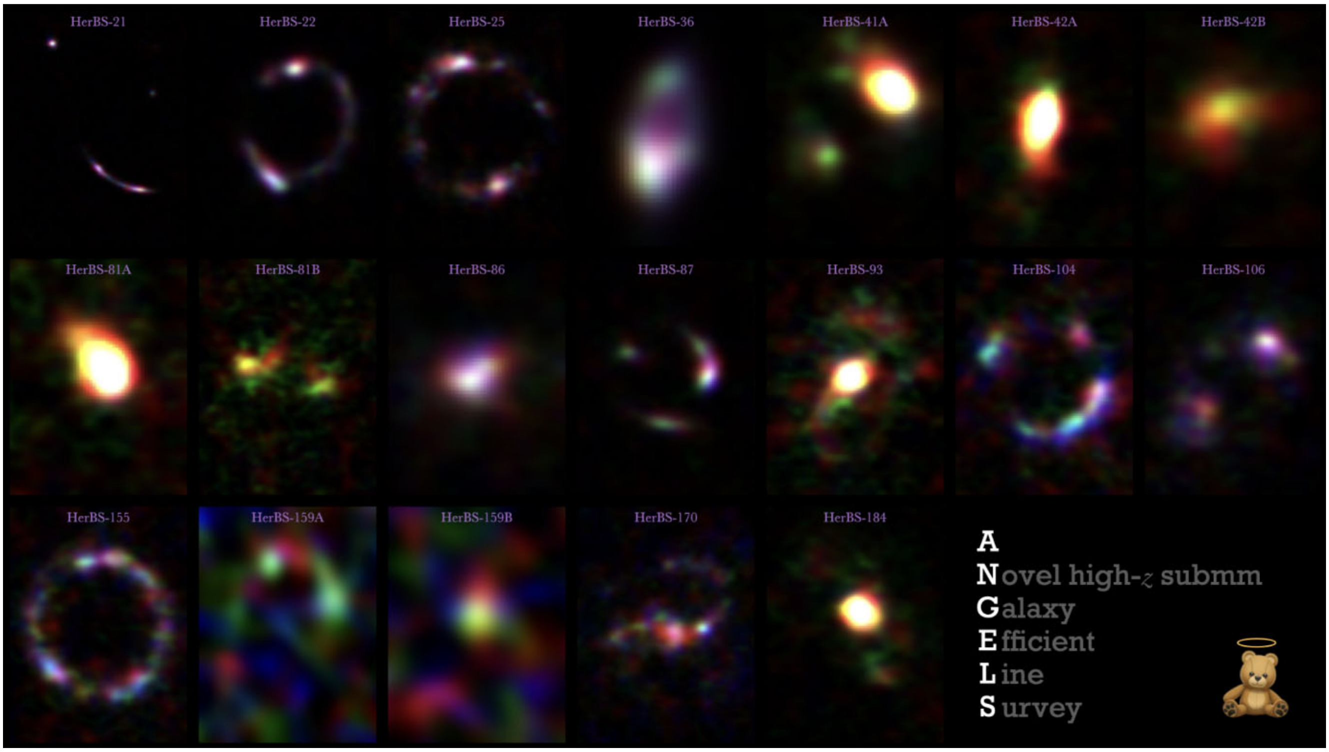

Figure F1. A composite RGB image across all 19 fields with Bands 6 (red), 7 (green), and 8 (blue) photometry shows the spread in morphologies across the ANGELS sources.

APPENDIX G: RESOLVED COMPARISON OF DUST TO GAS

The data enable a spatially resolved study of Schmidt–Kennicutt (see Fig. 12). We derive this in a pixel-per-pixel comparison shown in Appendix Fig. G1 for each of the sources with observed spectral lines.

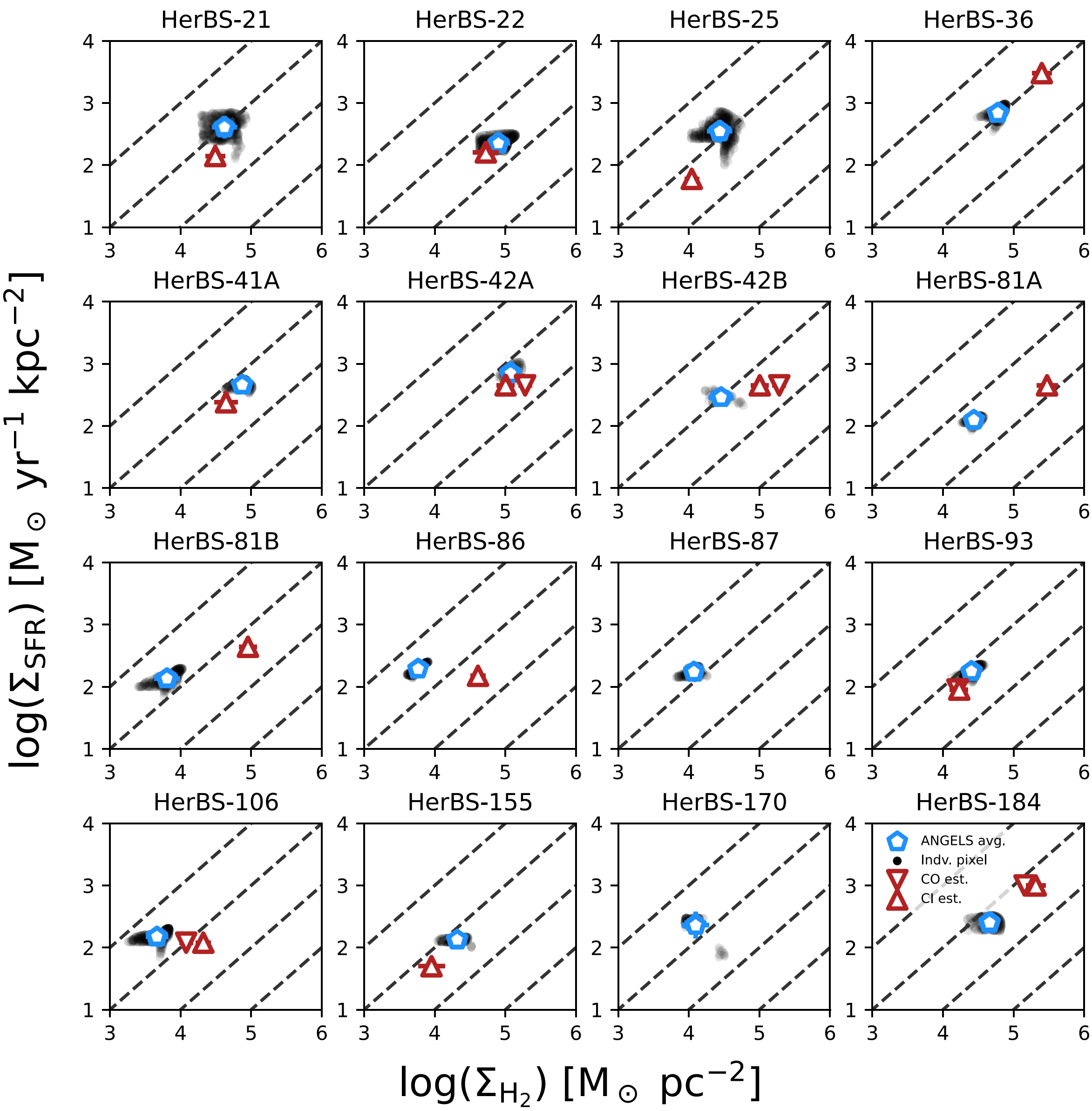

Figure G1. The pixel-per-pixel comparison of the Schmidt–Kennicutt relation for each source is shown for individual pixels (black points) and as the most likely value (blue pentagon) and associated errors. We show the constant depletion time-scales as diagonal lines for direct comparison to Fig. 12. The red upward and downward triangles indicate the position of the source on the Schmidt–Kennicutt relation based on the unresolved observations in Hagimoto et al. (2023) for CO and [C I]-derived dust masses, respectively.

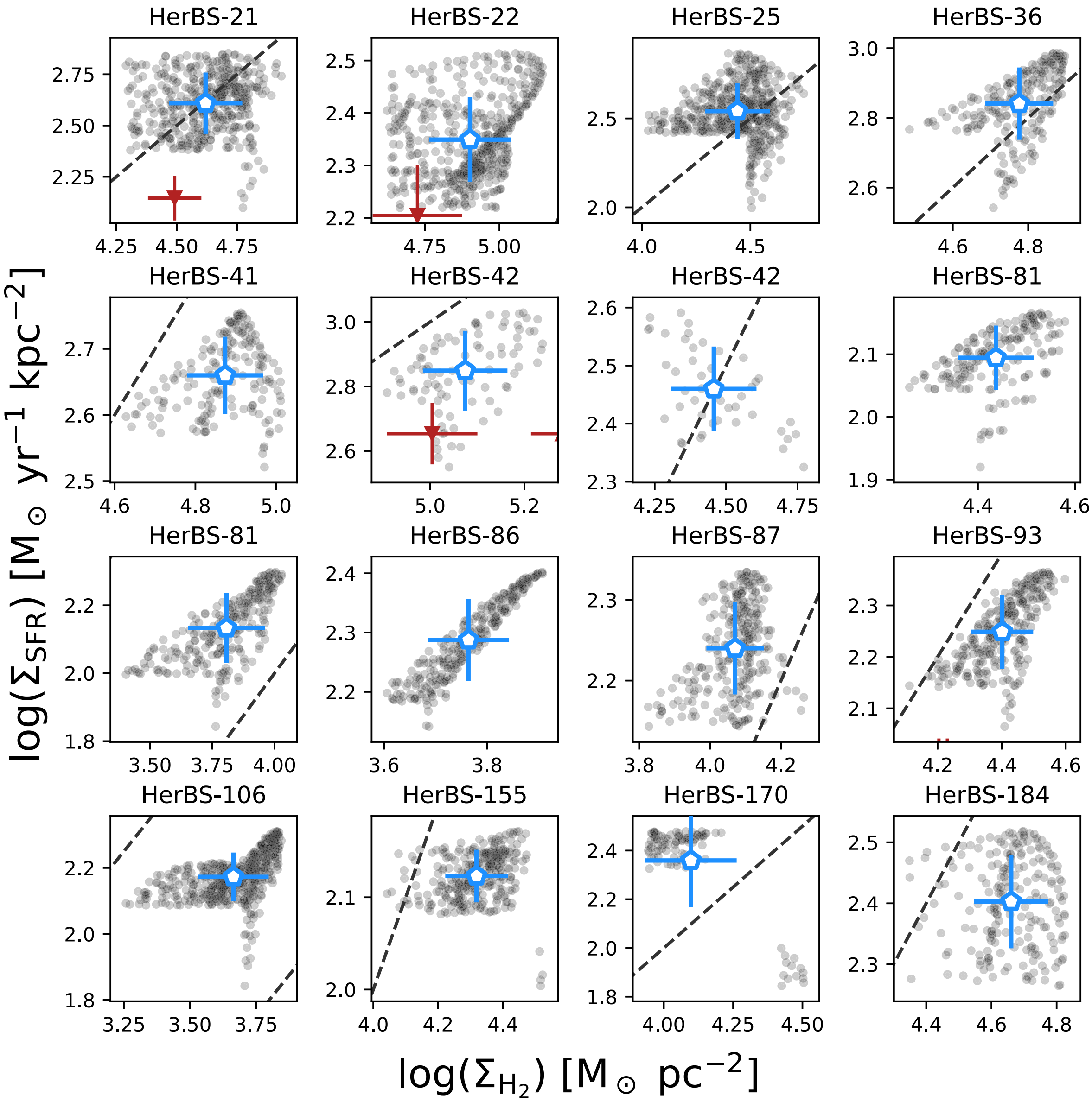

Figure G2. A zoomed-in version of Fig. G1 focusing on the pixel-per-pixel comparison of the Schmidt–Kennicutt relation, black points) and its most likely value (blue pentagon). The constant depletion time-scales are shown as diagonal lines for direct comparison to Fig. 12. The variation of the gas depletion times across the sources is spread roughly 0.2–0.5 dex. in both surface SFR and gas density. The sharp cut-offs seen most clearly for HerBS-25 and -106 originate from the 1 sigma extraction limit in the pixel-per-pixel comparison.

[1]*Department of Space, Earth, & Environment, Chalmers University of Technology, Chalmersplatsen, SE-4 412 96 Gothenburg, Sweden*
[2]*Department of Physics, Graduate School of Science, Nagoya University, Aichi 464-8602, Japan*
[3]*National Astronomical Observatory of Japan, 2-21-1, Osawa, Mitaka, Tokyo 181-8588, Japan*
[4]*Department of Physics, Centre for Extragalactic Astronomy, Durham University, South Road, Durham DH1 3LE, UK*
[5]*UK ALMA Regional Centre Node, Jodrell Bank Centre for Astrophysics, Department of Physics and Astronomy, University of Manchester, Oxford Road, Manchester M13 9PL, UK*
[6]*Hiroshima Astrophysical Science Center, Hiroshima University, 1-3-1 Kagamiyama, Higashi-Hiroshima, Hiroshima 739-8526, Japan*
[7]*School of Physical Sciences, The Open University, Milton Keynes, MK7 6AA, UK*
[8]*Departamento de Fisica, Universidad de Oviedo, C. Federico Garcia Lorca 18, E-33007 Oviedo, Spain*
[9]*Instituto Universitario de Ciencias y Tecnologas Espaciales de Asturias (ICTEA), C. Independencia 13, E-33004 Oviedo, Spain*
[10]*INAF – Osservatorio Astronomico di Padova, Vicolo Osservatorio 5, I-35122 Padova, Italy*
[11]*Institut d'Astrophysique de Paris, Sorbonne Université,UPMC Université Paris 6 and CNRS, UMR 7095, 98 bis boulevard Arago, F-75014 Paris, France*
[12]*European Southern Observatory, Alonso de Córdova 3107, Vitacura, Casilla 19001, Santiago de Chile, Chile*
[13]*European Southern Observatory (ESO), Karl-Schwarzschild-Strasse 2, D-85748 Garching, Germany*
[14]*School of Cosmic Physics, Dublin Institute for Advanced Studies, 31 Fitzwilliam Place, Dublin D02 XF86, Ireland*
[15]*Institute for Astronomy, University of Edinburgh, Royal Observatory, Blackford Hill, Edinburgh EH9 3HJ, UK*

[16]*ARC Centre of Excellence for All Sky Astrophysics in 3 Dimensions (ASTRO 3D)*
[17]*School of Earth and Space Exploration, Arizona State University, Tempe, AZ 85287-6004, USA*
[18]*Department of Astronomy, University of Cape Town, Private Bag X3, Rondebosch 7701, Cape Town, South Africa*
[19]*INAF – Instituto di Radioastronomia-Italian ARC, Via Piero Gobetti 101, I-40129 Bologna, Italy*
[20]*I. Physikalisches Institut, Universität zu Köln, Zülpicher Strasse 77, D-50937 Köln, Germany*
[21]*Research School of Astronomy and Astrophysics, Australian National University, Cotter Road, Weston Creek, ACT 2611, Australia*
[22]*Leiden Observatory, Leiden University, PO Box 9513, NL-2300 RA Leiden, Netherlands*
[23]*INAF – Osservatorio Astronomico di Roma, via di Frascati 33, I-00078 Monte Porzio Catone, Italy*
[24]*Institut de Radioastronomie Millimétrique (IRAM), 300 Rue de la Piscine, F-38400 Saint-Martin-d'Hères, France*
[25]*Department of Physics & Astronomy, University of California, Irvine, 4129 Reines Hall, Irvine, CA 92697, USA*
[26]*School of Physics and Astronomy, Cardiff University, The Parade, Cardiff, CF24 3AA, UK*
[27]*Department of Astronomy, School of Science, SOKENDAI (The Graduate University for Advanced Studies), 2-21-1 Osawa, Mitaka, Tokyo 181-8588, Japan*
[28]*Department of Astronomy, The University of Tokyo, 7-3-1 Hongo, Bunkyo, Tokyo 113-0033, Japan*
[29]*Department of Physics and Astronomy, University of British Columbia, 6224 Agricultural Road, Vancouver, BC V6T 1Z1, Canada*
[30]*Astrophysics Branch, NASA-Ames Research Center, MS 245-6, Moffett Field, CA 94035, USA*

This paper has been typeset from a TEX/LATEX file prepared by the author.